DEVELOPMENT AND CHARACTERIZATION OF A HIGH AVERAGE POWER, SINGLE-STAGE REGENERATIVE CHIRPED PULSE AMPLIFIER

By

VIDYA RAMANATHAN

A DISSERTATION PRESENTED TO THE GRADUATE SCHOOL
OF THE UNIVERSITY OF FLORIDA IN PARTIAL FULFILLMENT
OF THE REQUIREMENTS FOR THE DEGREE OF
DOCTOR OF PHILOSOPHY

UNIVERSITY OF FLORIDA

2006

To my family

ACKNOWLEDGMENTS

Graduate school has been an extremely enriching experience dispelling my naivety in more ways than one.

I owe a great deal to my mentor Dr. David Reitze for his guidance and encouragement that saw me through these past six years in graduate school. Not only did he acquaint me with the rudiments of ultrafast lasers, but he also helped me gain a deep insight and perspective into this field. I very much appreciate Dr. Reitze's treatment of his graduate students as junior colleagues. It is encouraging as well as challenging reminding me always of my discerning decision of joining his research team.

I am grateful to my committee members Profs. Hagen, Tanner, Stanton and Kleiman for serving on my supervisory committee and for all their advice and suggestions. I would also like to thank Prof. Nicolo Omenetto for agreeing to serve on my committee at an extremely short notice and was patient enough to read through my thesis and spot typos in just two days!

My sincere gratitude also goes to my fellow graduate students Jinho Lee, Shengbo Xu and Xiaoming Wang for all their help and for creating a pleasant environment in the laboratory. I would like to thank Dr. Yoonseok Lee and Pradeep Bhupathi for their ideas and suggestions about cryogenics and vacuum systems and also for all the stycast that they so willingly made for me! Bill Malphurs and Marc Link from the machine shop deserve special mention for their brilliant imagination and craftsmanship. Many thanks go to Luke Williams for letting me benefit from his expertise in thermodynamics and CAD designing software. I am extremely grateful to the support staff in the Physics department, Jay Horton, Don Brennan and many more for lending a helping hand whenever I needed one. I thank Darlene Latimer and Nathan Williams for all their assistance during times of distress! I would also like to thank all the folks in Tanner Lab

and Hebard Lab for letting me borrow sundry items and equipment from their laboratories from time to time.

I wish to thank my friends Ronojoy Saha, Karthik Shankar, Aparna Baskaran, Naveen Margankunte from the physics department and many others in Gainesville for providing respite from the trials and tribulations of graduate school with countless Friday nights filled with revelry!

Finally I wish to thank my parents and my siblings for their unconditional support and patience over all these years and the undaunted faith they have in me. Last but not least, a great deal of credit goes to Rajkeshar Singh who, although my husband of just two years, has been my best buddy for almost a decade now. I definitely do not envision myself here today if it were not for him.

TABLE OF CONTENTS

LIST OF TABLES

LIST OF FIGURES

Abstract of Dissertation Presented to the Graduate School
of the University of Florida in Partial Fulfillment of the
Requirements for the Degree of Doctor of Philosophy

DEVELOPMENT AND CHARACTERIZATION OF A HIGH AVERAGE POWER, SINGLE-STAGE REGENRATIVE CHIRPED PULSE AMPLIFIER

By

Vidya Ramanathan

December 2006

Chair: David Reitze
Major Department: Physics

Ultrashort pulses have revolutionized the field of optical science making it possible to investigate highly nonlinear processes in atomic, molecular, plasma and solid-state physics and to access previously unexplored states of matter. Although ultrashort pulses make an extremely useful tool, the generation of these highly energetic but short pulses is by no means trivial. Amplified ultrashort pulses are generated by the technique of chirped pulse amplification (CPA). Pulses with peak powers of the order of 10^{12} W from the CPA lasers when focused down to a surface area that correspond to a few square-microns generates high intensities capable of ionizing the medium or generate spectacular non-linear electromagnetic phenomena.

This dissertation details the design, fabrication and complete characterization of a high average power, high repetition rate, and single-stage chirped pulse amplifier system capable of delivering 40-45 fs pulses in the milli-joule range at multikilohertz repetition rate. In order to achieve millijoule level pulses from a single amplifier stage, the CPA systems need to be pumped with high average power sources. This introduces a host of thermal issues and thermal management then becomes necessary to increase the efficiency of such systems. In this work, we have carried out a systematic investigation of the thermal loading effects in a high average power, regenerative CPA system. We experimentally characterize the thermal aberrations using a variety

of different techniques (interferometry, pump-probe thermal lens power, and M^2 analysis). We compute the temperature distribution, the optical path deformations (OPDs) and the corresponding thermal lens focal powers using Finite Element Analysis (FEA) for different pumping conditions. The validation of the experimental results with the FEA model allowed us to use the model to design an effective regenerative amplifier cavity that is stable over a wide range of thermal lens focal length and hence over a wide range of repetition rates. The model could also predict optimal pumping conditions for minimizing thermal aberrations for a variety of geometries and pumping schemes.

The regenerative amplifier is capable of generating 40-45 fs, ~ 1mJ pulses at 5 kHz repetition rate and ~ 300 μJ at 12 kHz repetition rate with minimal fluctuations (0.9% of mean pulse energy) in the shot-to-shot pulse energy and good beam quality (average M^2 of 1.42 at 5 kHz).

CHAPTER 1
INTRODUCTION

Light is everywhere in the world. It has always been a carrier of information: from the real world to our brains through our eyes. Our vision defines a sense of perception, which in turn governs the way we look at the world. With the help of modern instruments, light has enabled us to see closely and understand phenomena beyond our limited visibility. From scrutinizing astronomical objects thousands of light years away from us to delving into the microscopic world, light has in many ways helped us achieve the impossible.

Much of this achievement witnessed accelerated growth after the invention of lasers, which have undoubtedly been one of the greatest inventions in the history of science. Since their arrival in the 1960s (Maiman, 1960) they have found themselves useful in almost all areas of science today. Barely years after the first laser was demonstrated DeMaria and coworkers (1966) generated ultrashort pulses which were picoseconds long from a modelocked Nd: glass laser. Atomic and molecular processes occur on time scales as short as a few picoseconds (10^{-12} secs) to a few femtoseconds (10^{-15} secs). The generation of short laser pulses has made it possible to observe such effects with very high temporal resolution. The shorter the pulse duration, the greater are the prospects of investigating highly nonlinear processes in atomic, molecular, plasma and solid-state physics and gain access to previously unexplored states of matter.

Through the 1970s picosecond pulses were generated from flash lamp pumped solid state materials such as ruby, Nd: glass and Nd: YAG using passive modelocking schemes such as saturable absorbers in the laser cavity. But the major drawbacks of these systems were the large fluctuations in the shot-to-shot output from the laser, and the instability of the saturable dye solution whose quality degraded with exposure to light. As a result focus shifted from solid state gain medium to organic dye lasers which were capable of generating pulses shorter than 10-ps.

The field of ultrafast laser development has seen rapid progress since the generation of high quality sub-picosecond (0.1-ps) laser pulses by Richard Fork, Benjamin Greene and Charles Shank in 1981. Pulse durations quickly dropped to the femtosecond regime (Shank et al., 1982) using colliding pulse modelocked lasers. With the invention of solid state laser material such as Ti^{3+} doped sapphire (Ti: Al_2O_3) by P. F. Moulton (1986) renewed interest in solid state lasers as they offered higher stored energies and unlimited operating and 'shelf' lifetimes as compared to organic dye liquids.

The discovery of self-modelocked Ti: sapphire lasers by Spence et al in 1991 revolutionized the field of ultrafast laser development. It now became possible to generate pulses as short as 5 fs (Jung, et al., 1997; Morgner et al., 1999) directly from a laser oscillator without the use of saturable absorbers. These table top lasers easily generate peak power levels of the order of a few megawatts $\left(10^6 W\right)$ (Huang et al., 1992a; 1992b; Asaki et al., 1993).

Ultrashort pulses allow for fast temporal resolution. One now has the capability to 'freeze' motion of fast moving electrons and molecules, facilitating the study of molecular dissociation dynamics, complex chemical reaction dynamics, etc. thus paving way for the field of femtochemistry (Zewail, 1996), which deals with the nature of transition states and their control.

Following the development of milli-joule level picosecond pulses by Strickland and Mourou in 1985, it became possible to generate millijoule level femtosecond pulses via the technique of Chirped Pulse Amplification. This saw an increase in peak power by six orders of magnitude $\left(10^{12} W\right)$ over those generated by the Ti: sapphire laser oscillators. Current table top laser systems can generate peak powers in the petawatt range $\left(10^{15} W\right)$ (Perry et al., 1999; Pennington et al., 2000, Kitagawa et al., 2004).These lasers have found a variety of applications over the past decade and continue to do so as our understanding develops.

Peak powers of a megawatt are however insufficient for many experiments. Several nonlinear optical processes like high harmonic generation, ultrashort surface science, generation of extreme ultraviolet radiation (EUV) (to name a few) are limited by the availability of ultrashort pulse energies and the average flux, making it necessary to amplify pulses from a self-mode-locked Ti: sapphire oscillators. The technique of chirped pulse amplification has progressed significantly since the amplified picosecond pulses from the system developed by Strickland and Mourou (1985). Amplification of ultrashort pulses by a factor of 10^6 to generate peak powers in excess of 10^{12} W (1 TW) at a repetition rate of 10 Hz was easily achieved (Maine et al., 1988; Kimetec et al., 1991; Sullivan et al., 1991; Zhou et al., 1995; Chambaret et al., 1996). S. Backus et al. (2001) extended the chirped pulse amplification technique to generate millijoule level, femotsecond pulses at multikilohertz repetition rate in a single stage chirped pulse amplifier system. Advantages of liquid nitrogen cooled Ti: sapphire crystal (Moulton, 1986; Schulz and Henion, 1991) were incorporated into a multipass amplifier cavity.

The advent of such high intensity, ultrafast lasers has facilitated many experiments in 'high-field' science. Matter exposed to intense ultrashort laser light undergoes ionization as the electronic wave packet is set free to oscillate in a laser electric field that is strong enough to overcome the effective binding potential. Nobel gases such as neon, argon, etc. when exposed to such intense electric fields, ionize generating electromagnetic waves at much higher frequencies. Also free electrons in plasma can be accelerated over 100 MeV in a space of only a few millimeters (Umstadter, 2001) using strong laser electric fields. As a specific example, millijoule level amplified pulses are essential for non-linear processes such as generating sub-nanometer range radiation, which are harmonics of the fundamental laser beam (L'Huillier and Balcou 1993; Bartels et al., 2000; Reitze et al., 2004). When a high-energy ultrashort laser pulse is tightly

focused the intensities created corresponds to an electric field that often exceeds the binding energy of a valence electron to the core of a noble gas atom. Within the first laser period the ejected electron from the parent ion is accelerated and it may return to the parent ion with a finite probability releasing harmonics that are coherent, directional and shorter in duration as compared to the driving laser pulse (Figure 1-1). Coherent soft and hard X-rays produced due to the harmonic up-conversion are used to conduct frequency interferometry in the ultraviolet to probe thin solid films and dense plasmas (Salieres et al., 1999; Descamps et al., 2000) and study electron transport dynamics in semiconductors (Rettenberger et al., 1997).

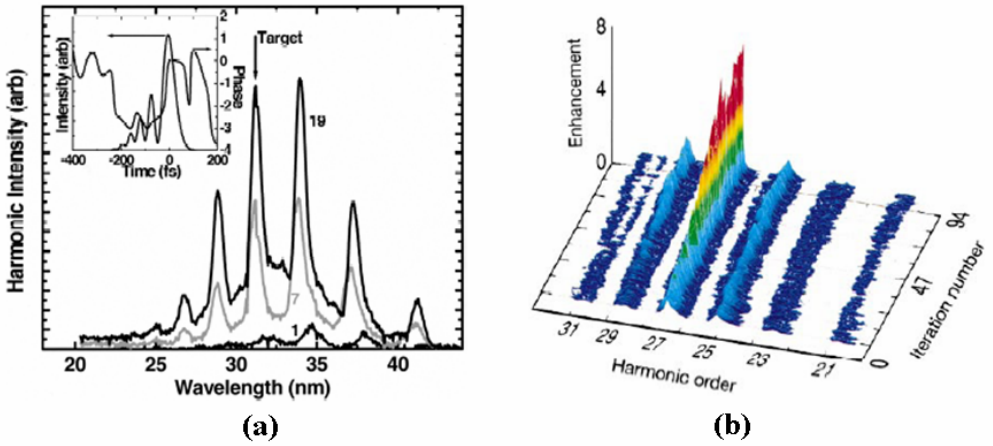

Figure 1-1: Harmonic generation in Ar gas. Using (a) 6-mJ, 30-fs, 800-nm pulses at 1 kHz repetition rate, Peak intensity ~ $3\times10^{14}\,W/cm^2$ (Reitze et al., 2004) and (b) 1-mJ, 25-fs, 800-nm pulses at 1 kHz repetition rate, Peak intensity ~ $2\times10^{14}\,W/cm^2$ (Bartels et al., 2000).

As a second example, high intensity laser pulses can ablate material non-thermally i.e without an increase in temperature. As in Figure 1-2 the quality of ablated holes and patterns in materials that undergo fabricated microstructures using femtosecond and picosecond pulses is much better than those produced using nanosecond pulses (Liu X et al., 1997; Von der Linde et al., 1997). Such fast 'cold' ablation technique where the solid is changed directly to the gas

phase is highly desirable as it reduces effects caused by heat conduction and interaction of the pulse with the ablated material.

In addition, amplified ultrashort pulses can further be compressed to sub-10 fs duration by self-phased modulation of these pulses in hollow core waveguides and pulse compression (Steinmeyer et al., 1999). Harmonics generated by such short and intense pulses give rise coherent x-rays with pulse duration as short as 10^{-18} s (100 attoseconds) (Paul et al., 2001; Hentschel et al., 2001) to study electronic state transition processes that occur faster than femtosecond timescales.

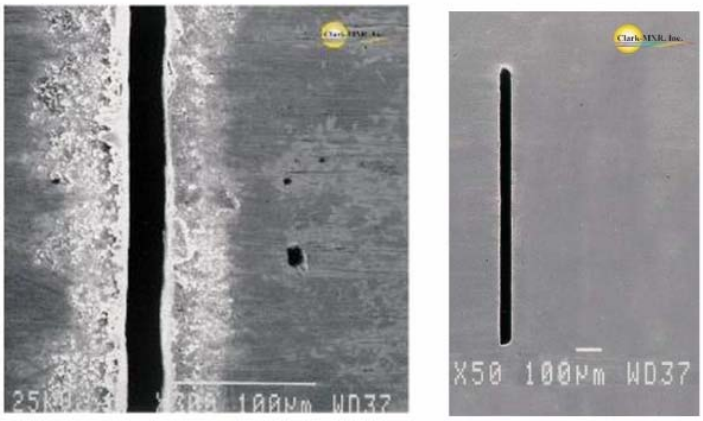

(a) (b)

Figure 1-2: A sheet of invar micromachined with (a) 10 nsec pulses and (b) 100-fs pulses. (http://www.cmxr.com/Industrial/Handbook/Chapter7.htm)

Femtosecond pulses with high energy and faster repetition rates are also utilized to perform surface non-linear spectroscopy (Ostroverkhov et al., 2005; Liu et al., 2005). As a second order nonlinear optical effect, second harmonic generation and sum-frequency generation are forbidden under the electric-dipole approximation in media with inversion symmetry. But at the surface or an interface this symmetry is necessarily broken. Thus non-linear surface spectroscopy is surface specific. As described in Figure 1-3 (a), two laser beams at frequencies ω_1 and ω_2 when mixed at an interface generate surface-specific sum frequency (or second harmonic,

when $\omega_1 = \omega_2$) output in transmission or reflection. The signal is proportional to the square of the nonlinear susceptibility $\left(\left|\chi_s^{(2)}(\omega) = \omega_1 + \omega_2\right|^2\right)$ of the interface. Scanning ω_2 over the vibrational resonances of the molecules or adsorbates on the surface, gives rise to a vibrational spectrum, which is unique to that particular surface/interface. When ω_1 and ω_2 are high energy pulses derived from a high brightness femtosecond chirped pulse amplifier, the peaks in the vibration spectra are well enhanced making it possible to detect surface abnormalities with ease.

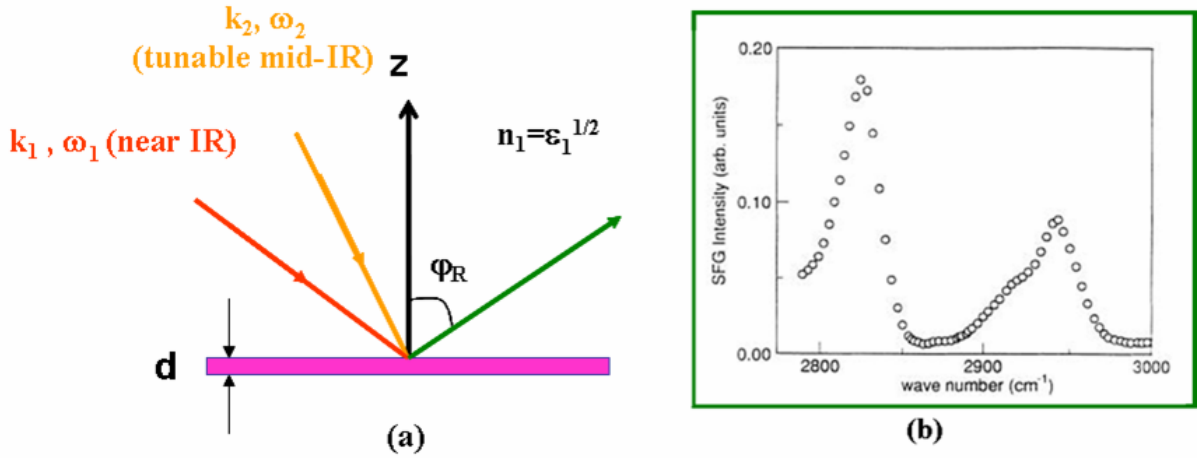

Figure 1-3: Schematic of surface spectroscopy (a) and a typical Sum-frequency Generation spectra (b). [Reprinted with permission from Superfine et al., (1991)].

An intense ultrashort laser pulse as available today, with peak powers ≥ $10^{22} W/cm^2$, are capable of generating electric fields at an excess of 10^{11} V/cm, can produce a wake of plasma oscillations through the action of the pondermotive force (Tajima and Dawson, 1979). An electron trapped in this wake is accelerated to relativistic speeds such that the work done by the electric field E over the wavelength λ of the laser field, $(eE\lambda)$ approaches the rest mass energy (m_0c^2) of the electron, where m_0 is the rest mass of the electron and c is the speed of light (Umstadter, 2001). Intense laser pulse when come in contact with plasma confined in a λ^3 volume, where λ is the wavelength of the laser radiation, is capable of generating attosecond

pulses and electron bunches (Naumova et al., 2004; Ness et al., 2005). These laser-based radiation sources may someday be used for cancer radiotherapy and as injectors into conventional accelerators, which are critical tools for x-ray and nuclear physics research.

The above examples present but a few of the applications of ultrafast lasers in physics, materials science, and chemistry. There is an ever-increasing need for ultrashort pulses at high pulse energies and faster repetition rates driven by these applications. The generation of these pulses is by no means trivial: the simultaneous requirement of high pulse energies (> 1 mJ) and high repetitions rates (> 5 kHz) necessitates high average power pumping. Thermal management then becomes the key to the operation of these highly pumped lasers. Improved thermal properties of sapphire at 77 °K (Moulton, 1986) allows for much efficient extraction of energy from the crystal in an amplifier making it possible to achieve millijoule pulses at kHz repetition rates in a single amplifier stage (Backus et al., 2001). Lowering the crystal temperature way below the ambient only reduces and does not eliminate the deleterious thermal effects. Thus in order to increase the overall efficiency of the chirped pulse amplifier system an extensive thermal analysis and characterization of the crystal in the amplifier becomes inevitable as it provides a better understanding of these thermal effects.

In this thesis we develop and characterize a high average power, single-stage, chirped pulse amplifier system that generates 40-45-fs pulses with pulse energies close to a 1mJ at 5 kHz repetition rate. We present a systematic investigation of the thermal loading effects in such amplifier systems. We experimentally characterize thermal aberrations in a regenerative amplifier using a variety of techniques. Using Finite Element Analysis (FEA) we compute the temperature distributions, optical path deformations (ΔOPD) and corresponding thermal focal lengths for a variety of pumping conditions. Excellent agreement between the FEA modeling and

the experimental results allow us to predict optimal pumping conditions for minimizing thermal aberrations that could further increase the efficiency of the system. The usage of the acousto-optic programmable dispersive filter (AOPDF) as a pulse shaper makes this a unique and a compact system capable of delivering ultrashort pulses in the millijoule range. High brightness sources such as this is ideally suited for high harmonic generation which is essential for the generation of attosecond pulses, plasma generation and acceleration of free electrons in plasma. Applications such as femtosecond micromachining and surface characterization using nonlinear frequency conversion techniques will benefit from the amplifier's high average powers for the high signal-to-noise measurements via lock-in detection.

The layout of the dissertation is as follows: in Chapter 2 we discuss the principles of ultrashort pulse generation and characterization. The design and construction of the various components of a high average power, single-stage chirped pulse amplifier is described in detail in Chapter 3. Chapter 4 deals with issues relating to the design, modeling and characterization of the host of thermal effects in a regenerative CPA system. The experimentally measured results are validated numerically using Finite Element Analysis (FEA). The characterization and the optimization of the pulses from the amplifier system are elaborated in Chapter 5 along with techniques that can further improve the efficiency of the CPA system. Finally we conclude in Chapter 6.

CHAPTER 2
ULTRASHORT PULSE GENERATION AND CHARACTERIZATION

Before we begin to delve into the details of the construction and performance of a high average power chirped pulse amplification system, it is beneficial to understand more about the fundamentals of generation and characterization of femtosecond pulses. This chapter discusses the various aspects of femtosecond pulses that are extremely crucial to the work described in this thesis.

Beginning with a mathematical relationship between pulse width and the spectral bandwidth the chapter discusses dispersion of broad bandwidth pulses. Principles of nonlinear effects such as the second and third order effects that are crucial for pulse characterization and the generation of ultra board brand sources respectively are discussed in the final sections of this chapter.

2.1 Relationship between Duration and Spectral Width

A plane monochromatic wave of frequency ω_0 (Figure 2-1 (a)) has an infinite spread in the time domain.

$$E(t) = \mathrm{Re}\left(E_0 \exp\left(i\omega_0 t\right)\right) \tag{2.1}$$

A light pulse can be generated from a sinusoidal electric field as in equation (2.1) by multiplying it with a bell shaped function for the amplitude modulation. Choosing a Gaussian function the above equation then transforms as

$$E(t) = \mathrm{Re}\left(E_0 \exp\left(-\Gamma t^2 + i\omega_0 t\right)\right) \tag{2.2}$$

The time evolution of equation (2.2) is shown in Figure 2-1(b). Γ is the shape factor of the Gaussian envelope. The spectral content of the two kinds of light pulses can be obtained by

performing a Fourier transform to the temporal domain. Figure 2-2 (a) and (b) are the numerical Fourier transforms for the cosine and the Gaussian function in equations (2.1) and (2.2).

The monochromatic plane wave oscillates with a single frequency ω_0 whereas the Fourier transform of the Gaussian function is also a Gaussian, with the width proportional to Γ.

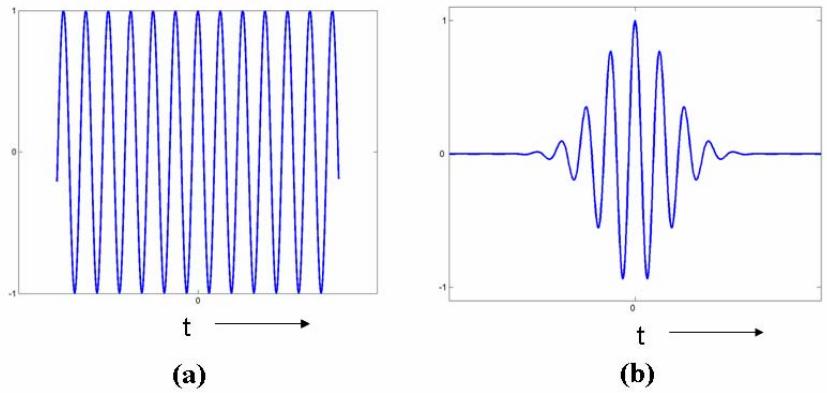

Figure 2-1: Evolution of a plane monochromatic wave in time (a) and a plane wave with Gaussian amplitude modulation in time (b).

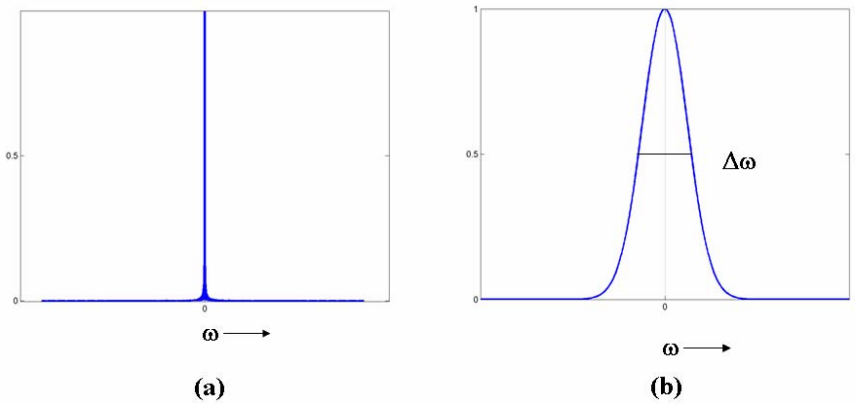

Figure 2-2: Fourier transform of the (a) cosine function in Figure 2-1(a) and (b) Gaussian function in Figure 2-1 (b).

From the empirical relationship between the spectral width and the pulse duration of the pulse, we can now derive a more formal relation (Seigman, pp.331). For a Gaussian electric field as in equation (2.2), the instantaneous intensity can be expressed as

$$I(t) = |E(t)|^2 = E_0^2 \exp\left[-(4\ln 2)\left(\frac{t}{\tau_p}\right)^2 \right] \qquad (2.3)$$

where τ_p is the duration of the pulse measured at half the maximum intensity and is known as the Full Width at Half Maximum (FWHM).

$$\tau_p = \sqrt{2\ln 2} \tag{2.4}$$

The Gaussian spectrum in frequency is the Fourier transform of equation (2.2)

$$E_0(\omega) = \exp\left[-\frac{(\omega-\omega_0)^2}{4\Gamma}\right] \tag{2.5}$$

The power spectrum of the Gaussian pulse can be written in the same form as the instantaneous intensity as in equation (2.3)

$$I(\omega) = \left|E_0(\omega)\right|^2 = \exp\left[-(4\ln 2)\left(\frac{\omega-\omega_0}{\Delta\omega_p}\right)^2\right] \tag{2.6}$$

The FWHM bandwidth of the Gaussian pulse is

$$\Delta f_p = \frac{\Delta\omega_p}{2\pi} = \frac{\sqrt{2\ln 2}}{\pi} \tag{2.7}$$

If in equation(2.2) , $\Gamma = (a - ib)$, where b is known as the chirp factor, then the pulsewidth τ_p and Δf_p undergo the following modification

$$\begin{aligned} \tau_p &= \sqrt{\frac{2\ln 2}{a}} \\ \Delta f_p &= \frac{\sqrt{2\ln 2}}{\pi}\sqrt{a\left(1+\left(\frac{b}{a}\right)^2\right)} \end{aligned} \tag{2.8}$$

Incorporating the Γ in the expression for electric field equation(2.2), in the time domain

$$E(t) = E_0 \exp\left(-at^2\right)\exp\left[i\left(\omega_0 t + bt^2\right)\right]$$
$$E(t) \propto \exp\left[i\phi_{tot}(t)\right] \tag{2.9}$$

where,

$$\phi_{tot}(t) = \omega_0 t + bt^2 \tag{2.10}$$

is the time varying phase of the Gaussian pulse. An instantaneous phase gives rise to an instantaneous frequency ω_i.

$$\omega_i = \frac{d\phi_{tot}(t)}{dt} \tag{2.11}$$

For the Gaussian pulse described above this instantaneous frequency is given as

$$\omega_i(t) = \frac{d}{dt}\left(\omega_0 t + bt^2\right) = \omega_0 + 2bt \tag{2.12}$$

Thus a Gaussian pulse with a time-varying instantaneous linear frequency is known as being *chirped* with the parameter *b* being a measure of this chirp. Figure 2-3 demonstrates a chirped Gaussian pulse.

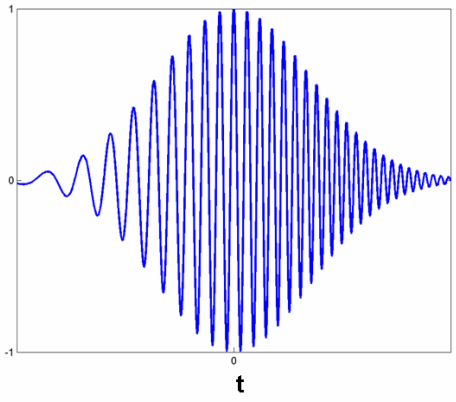

Figure 2-3: Time evolution of a Gaussian electric field with a quadratic chirp $(b = 10)$ on it.

2.2 Time Bandwidth Product

The product of pulsewidth and spectral bandwidth is known as the time bandwidth product (TBP). Multiplying equations (2.4) and (2.7) we get

$$\Delta f_p \tau_p = \frac{2\ln 2}{\pi} \approx 0.44 \qquad (2.13)$$

According to the uncertainty relation the time bandwidth product for a Gaussian pulse cannot be less than 0.44. Chirp on a Gaussian pulse increases the TBP.

$$\Delta f_p \tau_p = \left(\frac{2\ln 2}{\pi}\right) \times \sqrt{1+\left(\frac{b}{a}\right)^2} \approx 0.44 \times \sqrt{1+\left(\frac{b}{a}\right)^2} \qquad (2.14)$$

Thus for a Gaussian pulse the minimum TBP is 0.44 and such a pulse is known as 'transform-limit' as the linear chirp-factor $b = 0$.

The TBP depends on the shape of the pulse and the definitions of Δf and Δt (rms, FWHM, etc.). The table below compares the TBP for 3 fundamental pulse shapes suitable for laser beams, for other forms of intensity profiles such as square, triangular, exponential etc. the reader is urged to refer Sala et al (1980).

Table 2-1: Time bandwidth product for different pulse shapes (Figure 2-4)

Pulse Shape	Intensity $I(t)$	Time bandwidth product $\Delta f \, \Delta t$
Gaussian	$= e^{-x^2}$	0.4413
Hyperbolic Secant	$= \sec h^2 x$	0.3148
Lorentzian	$= \frac{1}{1+x^2}$	0.2206

Note: Adapted from Sala et al. (1980).

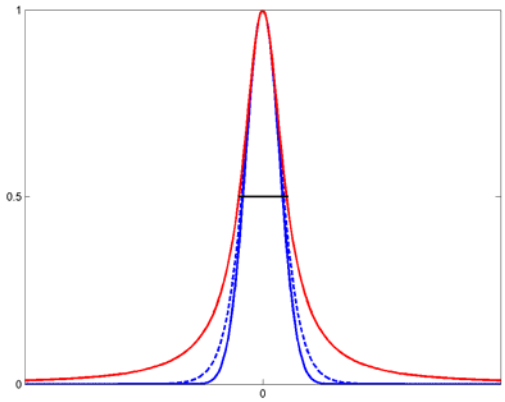

Figure 2-4: Intensity profile for a Gaussian pulse (solid blue curve), hyperbolic secant (dashed blue curve) and a lorentzian (red curve).

2.3 Dispersion

Ultrashort pulses, with its broad spectral content undergo dispersion as they propagate in air, materials, etc. Dispersion is said to occur when the phase velocity of the wave depends on its frequency (Born and Wolf). The vacuum dispersion relation is given as: $\omega = ck$, where ω is the angular frequency of the radiation, k is the wave number and c is the velocity of light in free space. For such a dispersion relation the phase velocity $\left(v_\phi\right)$ and the group velocity $\left(v_g\right)$ are the same. In a dispersive medium, the dielectric constant is a function of frequency $\varepsilon(\omega)$, with the consequence that $v_\phi \neq v_g$. Different components of the wave travel with different speeds and tend to change phases with respect to one another. An ultrashort pulse propagating through such a media will undergo changes in its shape ultimately leading to temporal broadening.

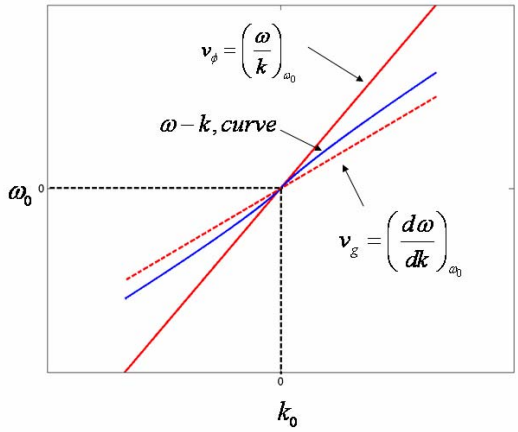

Figure 2-5: Schematic relationship between phase and group velocities for a transparent medium $\left(v_g < v_\phi\right)$.

The electric field of an ultrashort pulse, in the frequency domain is given by equation (2.5). After the beam propagates through a distance x, its spectrum is modified accordingly as

$$E(\omega) = E_0(\omega)\exp\left[\pm ik(\omega)x\right] \tag{2.15}$$

where $k(\omega) = n\omega/c$ is a frequency dependent propagation constant, with n being the refractive index of the medium. If the propagation constant $k(\omega)$ is a slowly varying function of ω: it can expanded in a Taylor series expansion about a central frequency ω_0 as long as $\Delta\omega \ll \omega_0$.

$$k(\omega) = k_0 + \left.\frac{\partial k}{\partial \omega}\right|_{\omega_0} (\omega - \omega_0) + \frac{1}{2!}\left.\frac{\partial^2 k}{\partial \omega^2}\right|_{\omega_0} (\omega - \omega_0)^2 + \frac{1}{3!}\left.\frac{\partial^3 k}{\partial \omega^3}\right|_{\omega_0} (\omega - \omega_0)^3 + \ldots \quad (2.16)$$

The frequency dependent propagation constant $k(\omega)$ will modify the pulse as it propagates through the medium. Substituting the above expression in equation (2.15)

$$E(\omega) = \exp\left[-ik_0(\omega)x - ik'x(\omega - \omega_0) - \left(\frac{1}{4\Gamma} - ik''x\right)(\omega - \omega_0)^2 + \ldots\right] \quad (2.17)$$

where, $k' = \left(\partial k/\partial\omega\right)\big|_{\omega=\omega_0}$ and $k'' = \left(\partial^2 k/\partial\omega^2\right)\big|_{\omega=\omega_0}$. The temporal evolution of such a pulse can be obtained by a Fourier transform of its spectral shape (Rulliere, pp.33).

$$E(t) = \frac{1}{2\pi}\int_{-\infty}^{\infty} E(\omega)\exp(-i\omega t)\,d\omega \quad (2.18)$$

$$E(t) = \sqrt{\frac{\Gamma(x)}{\pi}}\exp\left[i\omega_0\left(t - \frac{x}{v_\phi(\omega_0)}\right) - \Gamma(x)\left(t - \frac{x}{v_g(\omega_0)}\right)^2\right] \quad (2.19)$$

The first term in the exponent produces a time delay by an amount x/v_ϕ after propagation though a distance x. The quantity $v_\phi(\omega_0) = (\omega/k)_{\omega_0}$ is the phase velocity of each of the plane wave components of the pulse in the medium. $v_g(\omega_0) = (dk/d\omega)^{-1}$ is known as the group velocity and determines the speed of the pulse in the medium. For cases where $\omega \ll \omega_0$, $v_g < v_\phi$, and the pulse is said to undergo normal dispersion. Now $\Gamma(x) = 1/\Gamma + 2ik''x$, where $k'' = d/d\omega\left(v_g(\omega)^{-1}\right)$ is known as the group velocity dispersion. Figure 2-5 is a schematic of the dispersion effect in a

medium with a dispersion relation $\omega = ck(\omega)$. Thus the equation (2.19) demonstrates that a short pulse propagating through a transparent medium undergoes delay, a broadening of its pulse duration accompanied by a frequency chirp.

2.4 Nonlinear Effects

2.4.1 Second Order Susceptibility

Light intensities generated by an ultrashort pulse can change optical properties of the medium that they pass through. The intensity dependent changes to the optical properties of the material constitute nonlinear optics. Many of these nonlinear optical effects tend to be useful while generating and characterizing ultrashort pulses.

On expanding the polarization in a Taylor series expansion

$$P = \chi^{(1)}\mathrm{E} + \chi^{(2)}\mathrm{EE} + \chi^{(3)}\mathrm{EEE} + \ldots \qquad (2.20)$$

The first term in the above equation is the linear term whereas it's the higher-order terms that account for the nonlinear optical effects.

Second-order optical effect or second harmonic generation (SHG) is caused due to the second order susceptibility term $\chi^{(2)}$. It is characterized by the second-order polarization $P^{(2)}(t)$.

$$P^{(2)}(t) = \chi^{(2)}EE^{*} \qquad (2.21)$$

Two photons of frequency ω combine in a medium to give rise to a single photon of frequency 2ω (Figure 2-6). But the process of second harmonic generation is dependent on the orientation of the crystal axis and the polarization of the incoming light. If the medium posses an inversion symmetry, $\chi^{(2)}$ vanishes uniformly over the bulk of the medium. SHG in such cases can be observed either at an interface or on the surface of the medium. For an impinging intensity $I(\omega)$ of frequency ω with a propagation constant k_1, the intensity of the second

harmonic signal $I(2\omega)$ with the propagation constant $k_2 = 2k_1$ through a nonlinear crystal of length l is given as (Boyd)

$$I(2\omega) = \frac{2^7 \pi^3 \omega^2 \chi^{(2)} \lambda^2}{n^3 c^3} I^2(\omega) \left(\frac{\sin(\Delta k l / 2)}{\Delta k l / 2} \right)^2 \qquad (2.22)$$

where, $\Delta k = k_2 - 2k_1$ is known as the wavevector mismatch. The SHG process is most efficient for the perfect phase matched condition where $\Delta k = 0$.

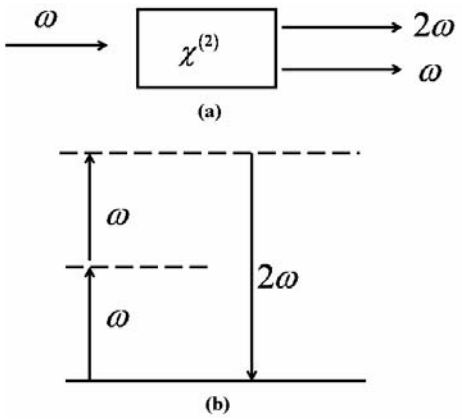

Figure 2-6: Geometry of second-harmonic generation (a) and schematic energy level diagram (b).

As the SHG signal for a given crystal length, orientation and polarization of the incoming light is directly dependent on its intensity, it is extensively used to measure the pulsewidth of an ultrashort pulse as described in detail in appendix A.

The second order susceptibility is also responsible for a variety of other effects that involve 3 photons such as the sum-frequency generation (SFG) where two incoming photons of frequency ω_1 and ω_2 combine in a nonlinear crystal and generate a signal at the sum frequency $\omega_3 = \omega_1 + \omega_2$. Difference frequency generation (DFG) is a process where the two incoming photons generate a signal at the difference frequency $\omega_3 = \omega_2 - \omega_1$ where $\omega_2 > \omega_1$. The satisfaction of the phase marching condition $\Delta k = k_1 + k_2 - k_3$ determines the efficiency of all these process within a non-centrosymmetric crystal.

2.4.2 Third Order Susceptibility

Three photons mix to generate third order nonlinear effects due to the third order susceptibility $\chi^{(3)}$ term equation(2.20). The third order polarization term can be written as

$$P^{(3)} = \chi^{(3)} E.E^{*}.E$$
$$P^{(3)} = \chi^{(3)} I.E \qquad (2.23)$$

Some of the third order effects include third harmonic generation (as in Figure 2-7) where three photons of frequency ω combine to generate a photon of frequency 3ω. Unlike the second order effect, the third order effect can occur in any media irrespective of the symmetry and can also occur in liquids and amorphous materials such as fused silica.

The number of effects increases as the order of nonlinearity increases. The primary focus of this chapter will be to discuss the effects related to generation and characterization of ultrashort pulses.

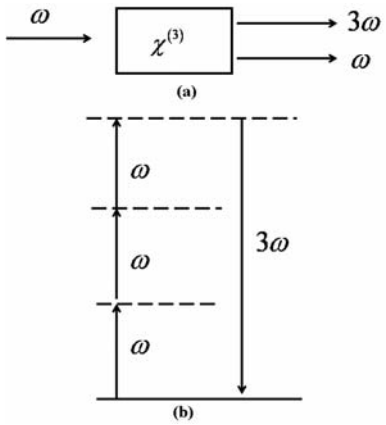

Figure 2-7: Geometry (a) and schematic of third order generation (b).

2.4.2.1 Nonlinear index of refraction

The intensity of the ultrashort pulse in a medium changes its optical properties. The third order polarization in equation (2.23) when combined with the linear polarization term becomes

$$P = \chi^{(1)} E + 3.\chi^{(3)} I.E = \chi_{eff} E(\omega)$$
$$where, \chi_{eff} = \chi^{(1)} + 3.\chi^{(3)} I \qquad (2.24)$$

where $I = \left|E^2\right|$ is the intensity of the incident ultrashort pulse. The second order term can be made to vanish in the above equation due to symmetry conditions in the crystal. For a centrosymmetric medium $\chi^{(2)}$ vanishes and for non-centrosymmetric medium the second order effects can be eliminated by orienting the crystal in such a way so as to satisfy the phase matching condition only for $\chi^{(3)}$ effects. The refractive index of the material is defined as: $n^2 = 1 + 4\pi\chi_{eff}$. Substituting for χ_{eff}, the refractive index can be expressed as

$$n^2 = 1 + 4\pi\chi^{(1)} + 12\pi\chi^{(3)}\left|E(\omega)\right|^2 \tag{2.25}$$

The refractive index of a material, when a high intensity laser beam is incident on it, can also be described by the following relation

$$n = n_0 + n_2\left|E\right|^2 \tag{2.26}$$

where n_0 and n_2 are the linear and nonlinear index of refraction respectively.

Comparing the relations (2.25) and(2.26), one can obtain expressions for n_0 and n_2

$$\begin{aligned} n_0 &= \left(1 + 4\pi\chi^{(1)}\right)^{1/2} \\ n_2 &= \frac{6\pi\chi^{(3)}}{n_0} I \end{aligned} \tag{2.27}$$

For an ultrashort pulse the intensity is a function of both space and time $I(r,t)$. Both the spatial and temporal dependence of intensity leads to interesting effects such as Kerr lens effect, self-phase modulation, self-focusing, filamentation etc. Effects that lead to the generation of ultrashort pulses are discussed in the following sections.

2.4.2.2 Kerr lens effect

The spatial intensity profile of a Gaussian laser beam propagating in a $\chi^{(3)}$ material is

$$I(r) = \exp\left(-gr^2\right) \tag{2.28}$$

The refractive index of the material also gains a spatial gradient given as

$$n(r) = n_o + n_2 I(r) \tag{2.29}$$

This generates a refractive index gradient as in Figure 2-8 that follows the gradient in the intensity profile of the incident ultrashort pulse. For a nonlinear index of refraction $n_2 > 0$, the refractive index is greater at the center of the medium as compared to the sides. The amount of nonlinear phase accumulated by the ultrashort pulse as it passes through this graded index material is

$$\Phi(r) = -\frac{2\pi}{\lambda} n_0 l - \frac{2\pi}{\lambda} n_2 l I(r) = -\Phi_0 - \frac{2\pi}{\lambda} n_2 l I(r) \tag{2.30}$$

This effect similar to a static lens, increases the focal power of the material due to the spatial variation in the phase of a traversing beam such that beam focuses into the material. This effect known as Kerr lens effect is of utmost importance in understanding self mode-locked Ti: sapphire laser oscillators.

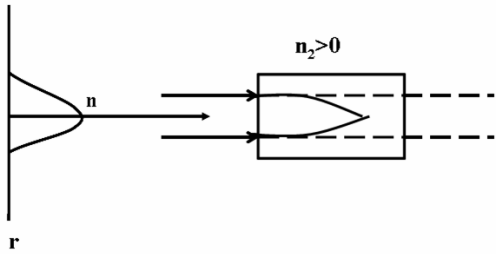

Figure 2-8: Schematic representation of the Kerr lensing effect. The KLM effect leads to the self-focusing of the intense ultrashort pulses.

2.4.2.3 Self phase-modulation

The temporal profile of a Gaussian pulse incident on a $\chi^{(3)}$ material is

$$I(r) = I_0 \exp\left(\frac{t^2}{\tau^2}\right) \tag{2.31}$$

Thus the refractive index is then transformed as

$$n(t) = n_0 + n_2 I_0 \exp\left(\frac{t^2}{\tau^2}\right) \tag{2.32}$$

The time varying intensity leads to a time varying refractive index as the pulse propagates

$$\frac{dn}{dt} = n_2 \frac{dI}{dt} = n_2 I_0 \exp\left(\frac{t^2}{\tau^2}\right)\left(-\frac{2t}{\tau^2}\right) \tag{2.33}$$

An instantaneous refractive index brings about a change in the total phase ($\Phi = -2\pi nl/\lambda$) accumulated by a pulse or a phase delay as it propagates through such a medium.

$$\Phi(t) = -\frac{2\pi}{\lambda} n_0 l - \frac{2\pi}{\lambda} n_2 l I(t) = -\Phi_0 - \frac{2\pi}{\lambda} n_2 l I(t) \tag{2.34}$$

where λ is the vacuum wavelength of the carrier and $n_0 l$ is the optical length traversed by the pulse. This generates a time varying shift in frequency

$$\begin{aligned} \omega(t) &= \frac{d\Phi}{dt} = -\omega_0 - \frac{2\pi}{\lambda} n_2 l \frac{dI}{dt} \\ \Delta\omega(t) &= -\frac{4\pi}{\lambda\tau^2} l n_2 I_0 \exp\left(\frac{t^2}{\tau^2}\right) t \end{aligned} \tag{2.35}$$

A plot of $\Delta\omega(t)$ (Figure 2-9) shows that the leading edge of the pulse shifts towards the lower frequencies (‘red’ shift) and the trailing edge shits towards higher frequencies (‘blue’ shift), generating an overall increase in the bandwidth of the pulse.

Although the spectral content of the pulse is increased as it passes through such a crystal the temporal structure remains unaltered by the self-focusing effect. But natural dispersion occurring within the crystal tends to broaden the pulse.

Ti: sapphire-based laser oscillators make use of the Kerr-lensing effect to generate pulse as short as 6-fs (Jung et al., 1997) directly from an oscillator which is described in detail in the following chapter.

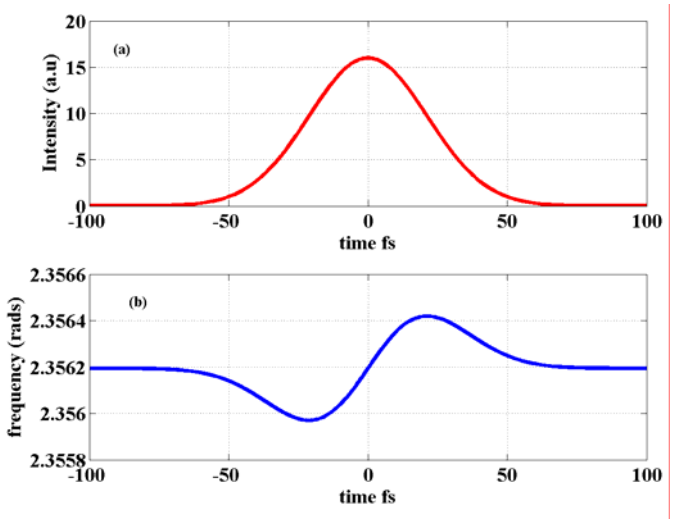

Figure 2-9: Schematic of Self-phase modulation. (a) A Gaussian pulse propagating through a nonlinear system undergoes self focusing effect (b) which gives rise to additional frequency components which when compensated for material dispersion generates a short pulse.

2.5 Summary

We briefly discussed in this chapter the essential theoretical background needed to understand the various nonlinear process such as the generation of femtosecond lasers through the Kerr lensing effect. Also processes such as the second harmonic generation which is a commonly used tool to characterize ultrashort pulse widths, were discussed in considerable detail. More on the technique of measuring ultrashort pulses are elaborated in Appendix A at the end of this dissertation.

CHAPTER 3
DESIGN AND CONSTRUCTION OF A HIGH AVERAGE POWER, SINGLE STAGE CHIRPED PULSE AMPLIFIER

3.1 Introduction

Strickland and Mourou (1985) developed the first ultrashort laser in the year 1985, capable of delivering millijoule pulses at picosecond time scales ($2x10^{-12}$ secs) at a wavelength of 1.06 μm, by the technique of chirped pulse amplification. Ultrashort pulses by definition support a large spectral bandwidth $\left(\Delta\upsilon\Delta\tau = const\right)$. Amplification of ultrashort pulses enforces certain minimum requirements on an amplifier system. First, the amplifier bandwidth must be wide enough to accommodate the spectral bandwidth of the seed or the un-amplified pulses. As a wide range of Fourier components is required to produce an ultrashort pulse, a gain medium with a narrow emission bandwidth could not possibly support ultrashort pulses. The central wavelength λ_0 of the seed pulses must efficiently extract the stored energy in the amplifying medium, i.e the fluence of a pulse must be close to the saturation fluence of the amplifying gain medium $J_{sat} = h\upsilon/\sigma_g$ where σ_g is the gain cross-section of the gain medium. Finally the peak intensities generated within the amplifier must be well below a certain critical level above which nonlinear effects as discussed in chapter 2 can distort both the spatial and the temporal profile of the amplified beam and in some cases can damage the optical components within an amplifier as well.

3.2 Why Chirped Pulse Amplification?

While amplifying femtosecond pulses, the phase shift experienced by a propagating ultrashort pulse in an amplifying medium can be both linear and nonlinear

$$\phi_{Total} = \frac{2\pi}{\lambda} nl = \frac{2\pi}{\lambda}\left(n_0 + n_2 I(r,t)\right) l$$
$$\phi_{Total} = \phi_{Linear} + \phi_{NL} \tag{3.1}$$

The linear phase $2\pi n_0 l/\lambda$ arises due to the linear index of refraction n_0. The nonlinear phase shift arises from the nonlinear response (distortion) of the electron cloud surrounding an ion subjected to an intense electric field. As can be seen from equation (3.1), the peak intensities associated with an ultrashort pulse introduce additional phase delay $\left(n_2 > 0\right)$ and therefore experience enhanced nonlinearities, which are manifested both in temporal as well as spatial distortions of the laser pulse. One can calculate the nonlinear phase accumulated by an ultrashort pulse along an optical path L as (Koechner, 1976)

$$\Phi_{NL} = \frac{2\pi}{\lambda}\int_0^L \frac{\Delta n}{n} dl = \frac{2\pi}{\lambda}\int_0^L n_2 I(r,t) dl \tag{3.2}$$

where n_2 is the nonlinear index of refraction of the lasing medium and $I\left(r,t\right)$ is the instantaneous pulse intensity within the amplifier cavity. A peak value of 5 for the nonlinear phase Φ_{NL} (for historical reasons also known as the 'B integral') corresponds to a critical intensity (Maine et al., 1988) above which only high spatial frequencies are preferentially amplified, reducing the spectral bandwidth of the amplified pulses that ultimately results in longer pulses. As noted in the previous chapter a host of nonlinear effects are associated with the spatial as well as the temporal variation of the intensity of an ultrashort pulse. And if the accumulated nonlinear phase exceeds this critical value, the ultrashort beam becomes distorted due to these nonlinear processes (Boyd, 2003). Thus keeping the amount of nonlinear phase that an ultrashort pulse can gather, much below the threshold value is of utmost importance in amplifying these pulses to high energy levels.

Given a suitable gain media like $Ti^{3+}:Al_2O_3$ (which shall be discussed in the following section), the technique of chirped pulse amplification circumvents the generation of excess amplified intensities capable of damaging amplifier materials or causing nonlinear effects. Figure 3-1 illustrates a schematic of a chirped pulse amplification system.

This technique relies on increasing the duration of the pulse being amplified by introducing a controlled amount of dispersion ('chirping' the beam) and then optically compressing (Treacy, 1969; Martinez, 1987; Martinez, et al.,1984) the amplified beams to its original pulse duration.

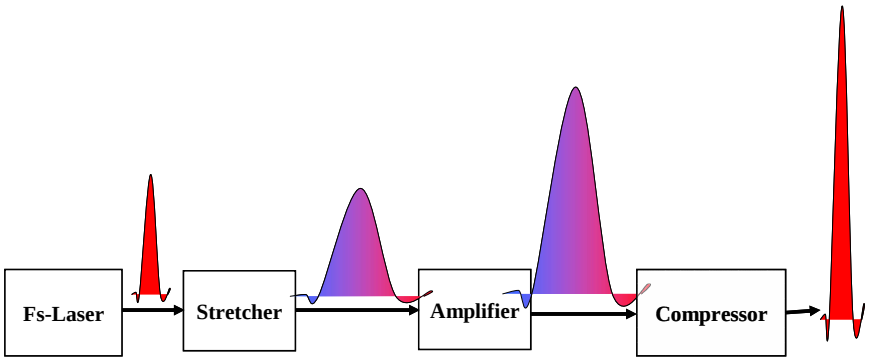

Figure 3-1: A schematic representation of a Chirped Pulse Amplifier system. The pulse cartoons represent the temporal structure of the pulse at each stage in the amplification process.

Temporally lengthening (or 'stretching') the pulses reduces the peak intensity, enabling efficient energy extraction from the amplifier gain media by distributing the total energy content of the pulse over a broader time scale. Chirped pulse amplification becomes particularly useful for amplifiers utilizing solid-state gain media with high stored energy densities (1—10 J/cm^2) well above the damage threshold of several optical components, in order to efficiently extract the entire stored energy in the gain media.

The following sections contain an in depth discussion of the various components of a single stage, CPA system in our laboratory.

3.3 Ti: Sapphire as Gain Medium

Ultrashort pulse amplification needs very broadband gain media. Femtosecond amplifiers in the past relied heavily on broadband laser dyes and excimer gain mediums as the amplifying material (Ippen and Shank, 1986; Downer et al., 1984; Knox et al., 1984). Due to the low saturation fluences offered by these media, the amplified output powers were severely limited by the size of the amplifying medium. But solid-state media such as Nd: glass, Cr^{3+} doped $BeAl_2O_4$ (Alexandrite), Cr^{3+} and Ti^{3+} doped Al_2O_3 (sapphire) not only posses much higher stored energies (~ 1J/cm^2) but also display extremely broad emission bandwidths to support ultrashort pulses (Moulton, 1992).

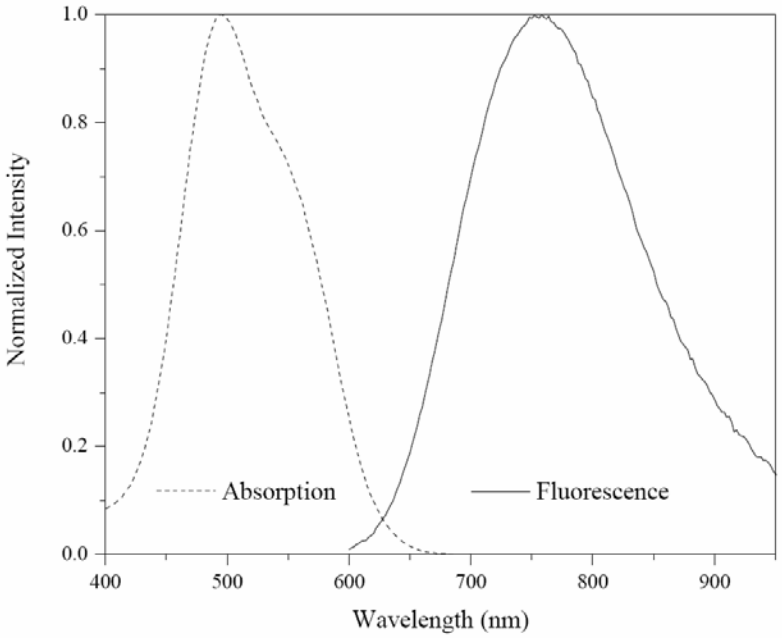

Figure 3-2: Absorption and emission spectra for Ti: sapphire. [Adapted from Rulliere (1998)].

Of all the solid state materials available, Ti^{3+} doped Al_2O_3 (commonly referred to as Ti: sapphire) emerged to be the most promising material (Moulton, 1986). The early nineties saw a boom in the use of Ti: sapphire as an active medium to produce femtosecond pulses due a number of its features that were desirable as a laser host material. With a damage threshold of 8-10 J/cm^2 (comparable with metals), high saturation fluence of 0.9 J/cm^2, a peak gain cross-

section σg of 2.7 × 10-19 /cm^2 (Backus et al., 1998) and an extremely broad gain bandwidth of 230 nm (Moulton, 1986), there is little doubt as to why Ti: sapphire is a favorite among femtosecond-laser developers! Ti: sapphire exhibits a peak absorption maximum at 500 nm. Figure 3-2 indicates the absorption and emission bandwidths for Ti^{3+} doped Al_2O_3. With the availability of high average power diode-pumped solid-state lasers, such as the frequency doubled Nd: YAG and Nd: YLF laser source (laser emission at 532 nm), Ti: sapphire quickly became the obvious choice in the development of table-top terawatt sources (Backus et al., 2001).

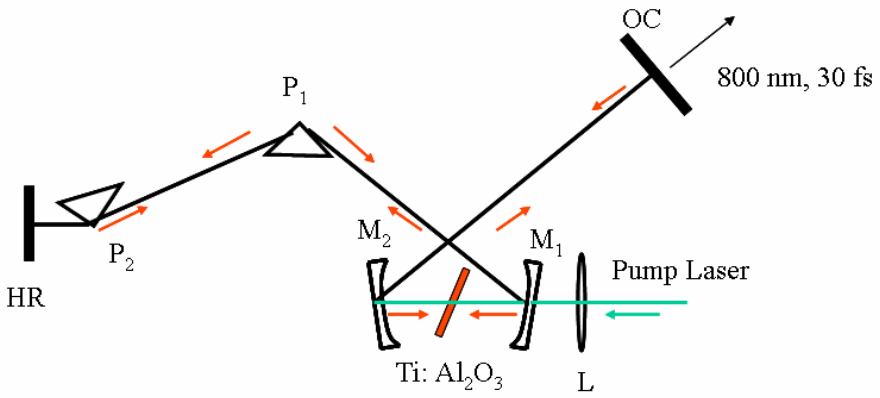

Figure 3-3: Self-mode-locked Ti: sapphire laser oscillator. The cavity is formed by a high reflecting mirror (HR) and an output coupler (OC). The pump beam is focused on to the crystal which is placed in a sub-resonator formed by mirrors M_1 and M_2. Dispersion compensation is achieved by prisms P_1 and P_2.

There has been a tremendous amount of progress in the generation of femtosecond pulses since the construction of the first self mode-locked Ti: sapphire laser by Spence et al. in 1991 generating 60-fs pulses. With further improvisations to their optical design (Figure 3-3), it became possible to generate pulses as short as 6 fs (Jung et al., 1997) directly from a laser oscillator. Short pulses were achieved by the process of Kerr-Lens mode-locking (discussed in the previous chapter), wherein an inherent nonlinearity of the Ti: sapphire crystal was creditably exploited, which is yet another reason why Ti: sapphire is the most revered material for ultrashort pulse generation!

3.4 Mode-locked Laser

Mode-locking is the essential mechanism to generate pulses from a laser oscillator. A laser cavity allows oscillation only for discreet resonance frequencies that satisfy the condition $\upsilon_m = mc/2L$, where c is the velocity of light and L is the length of the laser cavity and m is an integer. The longitudinal modes of a laser cavity oscillate freely and the output intensity consists of different modes with no specific phase relation with respect to each other and the laser is said to be operating in a 'continuous wave' or cw mode. These modes which initially possess random phases, when forced to oscillate with a well defined phase constitutes a pulse and the laser is then said to be lasing in a pulsed mode with a finite bandwidth spectrum as in Figure 3-4.

Mode-locking in dye lasers and in certain solid state media was achieved either by an external modulation (active mode-locking) or by placing saturable absorbing medium in the laser cavity (passive mode-locking).

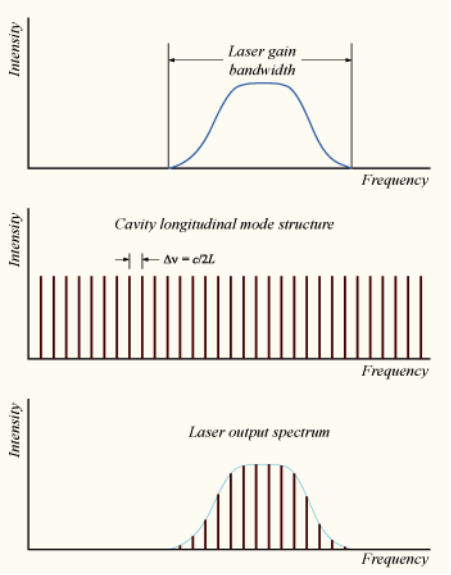

Figure 3-4: Generation of ultrashort pulses by the mechanism of mode locking.

Ti: sapphire laser does not require either external stimulation or saturable absorbers to generate ultrashort pulses. This is known as self mode-locking. As discussed in the previous

chapter, an intensity dependent variation of the refractive index of the Ti: sapphire crystal, arising from a non-uniform power density distribution in Gaussian beams gives rise to an intensity dependent phase-shift that leads to the generation of multiple modes within the oscillator cavity. The amplitude of the short pulse is modulated in such a way that intense pulses experience less loss than weaker pulses and can therefore sustain within the cavity.

Figure 3-3 is a schematic of a self-mode-locked Ti: sapphire laser oscillator. The laser cavity is formed by two plane mirrors, one a high reflecting mirror (HR) and an output coupler (OC) which is partly transmitting. The Ti: sapphire crystal is placed in a sub resonating cavity formed by two identical spherical mirrors of radii of curvature 10-cm, which are dichroic in nature, transmitting 532-nm and reflecting 800-nm. Two fused silica prisms placed in the longer arm of this asymmetric cavity provide the phase compensation necessary to achieve mode locking. The Ti: sapphire crystal is pumped by a 5 W Coherent Verdi which is a diode pumped Nd: YVO_4 laser system.

The refractive index of sapphire varies with the intensity of the incident pulse as $n = n_0 + n_2 I(r)$. The crystal behaves like a converging lens as $n_2 > 0$. The Kerr lensing effect in conjunction with the self-focusing of the laser beam within the crystal gives rise to the broadening of the spectral content of the pulse.

Although the spectral content of the pulse is increased as it passes through the Ti: sapphire crystal the temporal structure remains unaltered by the self-focusing effect. But natural dispersion occurring within the crystal tends to broaden the pulse. The prism pair inside the oscillator cavity generates negative dispersion to compensate for the positive dispersion introduced by the crystal (Martinez et al., 1984; Fork et al., 1984), enabling the generation of femtosecond pulses from the oscillator. Careful balancing of the self-phase modulation effects

and the group velocity dispersion due to the prism pair causes all the modes in the oscillator to have the same optical path length through the crystal, forcing them to oscillate in phase to generate a train of mode-locked pulses with a repetition rate $1/\tau_R$ where τ_R is the round trip time around the cavity.

The peak intensities inside the Ti: sapphire crystal must be high enough to induce nonlinearity but well below a critical level, which can distort the beam within the cavity. In order to favor the high intensity pulsed operation of the laser over the continuous-wave (cw) mode, old designs of the Ti: sapphire oscillator used a hard aperture blocking out the large waist modes that correspond to low intensity levels.

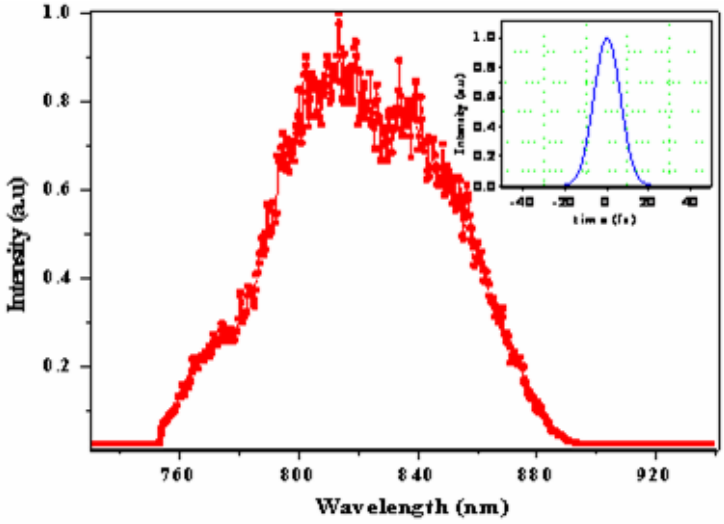

Figure 3-5: Oscillator spectrum as measured by a fiber spectrometer[1] and its Fourier transform. Inset is the calculated temporal profile (temporal bandwidth of 14 fs) assuming a constant phase across the entire spectral bandwidth.

Instead of the hard aperture, the pump beam in the oscillator is overlapped on the crystal with the pulsed beam, such that it preferentially keeps the cw beam in the cavity at extremely low intensities, enabling mode-locked operation. Mode locking is readily achieved by gently

[1] The modulations in the measured spectrum are an artifact of the fiber spectrometer. The temporal profile was calculated on first filtering the measured spectrum with a Savitzky-Golay smoothing function and then performing an inverse Fourier transform on the smoothed spectrum.

stroking the prism next to the high reflecting mirror. The oscillator routinely generates 300-400-mW mode-locked pulses at the repetition rate of 90 MHz (defined by the cavity length), centered at 800-nm and a full width of half-maximum bandwidth (FWHM) of 80-90-nm, an average pulse energy of 2-5 nJ depending on the alignment. A pair of razor edges that form a slit allows tuning of the mode locked spectrum. In order to stabilize the laser in the mode locked state, the Ti: sapphire crystal is maintained at a constant temperature of 20 °C by a circulating water chiller. Also for prolonged stability, the laser is isolated from the environment by enclosing it in a protective case. Due to the absence of an external compensator to generate transform limit pulses from the oscillator, the temporal FWHM is always greater than calculated as in the inset of Figure 3-5.

The seed pulses from the oscillator are then introduced into a pulse stretcher to temporally broaden the pulses before they can be injected into the amplifier.

3.5 Dispersion

The phenomenon of dispersion is very important to the field of ultrafast optics. As ultrashort pulses, with their broad spectral content undergo dispersion as they propagate in air, materials, etc., dispersion management then becomes the key to developing really short pulses. As previously noted, dispersion is said to occur when the phase velocity of the wave depends on its frequency (Born and Wolf). Different components of the wave travel with different speeds and tend to change phases with respect to one another. An ultrashort pulse propagating through such a medium will undergo changes in its shape ultimately leading to temporal broadening. The electric field of an ultrashort pulse is represented in the frequency domain as

$$E(\omega) = \tilde{\mathrm{E}}(\omega)\exp\left(i\phi(\omega)\right) \tag{3.3}$$

where $\tilde{E}(\omega)$ is the amplitude modulation for a finite beam and $\phi(\omega)$ is the phase of each of the frequency components present in the beam. If the spectral phase $\phi(\omega)$ is a slowly varying function of ω (this does not hold true in regions of 'anomalous dispersion' where $n(\omega)$ varies rapidly over narrow intervals of ω) then it can expanded in a Taylor series expansion about a central frequency ω_0.

$$\phi(\omega) = \phi_0 + \left.\frac{\partial\phi}{\partial\omega}\right|_{\omega_0}(\omega-\omega_0) + \frac{1}{2!}\left.\frac{\partial^2\phi}{\partial\omega^2}\right|_{\omega_0}(\omega-\omega_0)^2 + \frac{1}{3!}\left.\frac{\partial^3\phi}{\partial\omega^3}\right|_{\omega_0}(\omega-\omega_0)^3 + \ldots \quad (3.4)$$

where $\partial\phi/\partial\omega$, $\partial^2\phi/\partial\omega^2$ and $\partial^3\phi/\partial\omega^3$ are the derivatives of phase with respect to frequency and are known as group delay, second-order dispersion or group velocity dispersion (GVD), third-order dispersion (TOD), fourth-order dispersion (FOD) and so on. The variation of the group delay $\tau = \partial\phi/\partial\omega$ with frequency is

$$\tau = \frac{\partial\phi}{\partial\omega} = \phi'(\omega_0) + \phi''(\omega_0)(\omega-\omega_0) + \phi'''(\omega_0)(\omega-\omega_0)^2 + \ldots \quad (3.5)$$

From the above expression, it is clear that the $\phi''(\omega_0)$, known as frequency-sweep rate linearly chirps the pulse and $\phi'''(\omega_0)$ generates a quadratic chirp on the pulse, etc. Figure 3-6 (a) and (b) illustrate a Gaussian pulse with a second-order and third order phase on it that generates a linear and quadratic chirp on it respectively.

For pulses that undergo normal dispersion in materials, the phase change is given by $\phi_{mat}(\omega) = L_{mat}n(\omega)\omega/c$. Thus longer wavelength components in the pulse travel faster than the shorter wavelength components i.e 'red' travels faster than 'blue', introducing a positive chirp. A pulse compressor then becomes inevitable to compensate for this positive chirp.

The management of spectral phase is thus of utmost importance in the design of a chirped pulse amplifier system. The next section deals with the broadening or the chirping of the pulses

in order to effectively amplify them in an amplifier and their recompression back to femtosecond time scales.

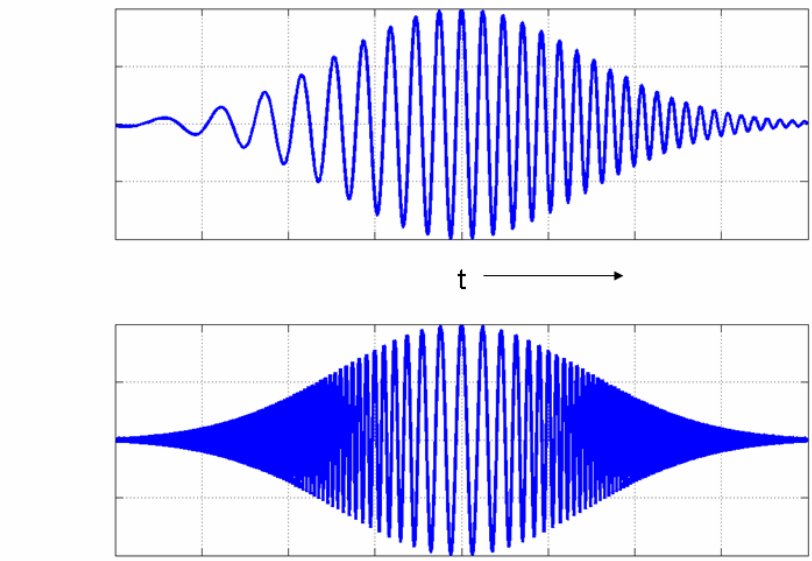

Figure 3-6: A Gaussian pulse possessing (a) linear chirp $\left(\phi''(\omega_0)\right)$ on it and (b) quadratic chirp $\left(\phi'''(\omega_0)\right)$ on it.

3.6 Pulse Stretching and Recompression

As an ultrashort pulse propagates through the different optical components in an amplifier cavity, the material dispersion accumulated must be compensated for in order to achieve shorter pulse durations. Also in order to reduce the risk of damaging the amplifier components and to keep the amount of accumulated non-linear phase [equation(3.2)] well below the threshold level, femtosecond pulses obtained from the Ti: sapphire oscillators must be temporally broadened before they can be injected into an amplifier. Also, in order to generate ultrashort pulses in a mode-locked Ti: sapphire oscillator it becomes necessary to compensate for the group velocity dispersion (GVD) such that all the spectral components of the pulse can travel with the same group velocity around the oscillator cavity. Thus dispersive components become an integral part of a chirped pulse amplifier system.

Pulse stretching can simply be accomplished by material dispersion. As beams traverse through material they tend to broaden temporally owing to normal dispersion. But for most materials significant lengths are needed to achieve stretch factors of 10^4 which are required to amplify nanojoule level femtosecond pulses to the millijoule level. In addition, one cannot avoid beam distortions due to the increased B-integral.

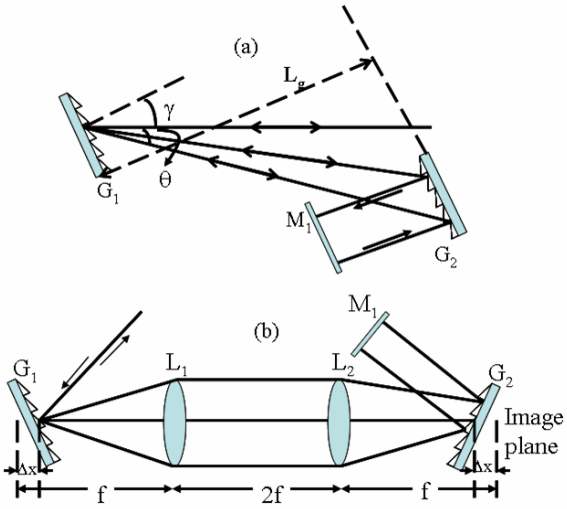

Figure 3-7: Dispersive delay lines. (a): A pair of anti-parallel gratings forms a pulse compressor (Treacy, 1969) and (b) Pulse stretcher formed by anti-parallel gratings with a unit magnification telescope between them by Martinez et al. (1984).

In 1969 E. B. Treacy showed an extremely clever way of broadening pulses in time by using an anti-parallel grating pair (Figure 3-7(a)). Significant stretch factors could be achieved with this arrangement, although as originally conceived the Treacy configuration was designed to produce negative group delay dispersion that could compensate for positive material dispersion. The grating pair disperses the spectrum of the pulse, such that the 'blue' edge of the spectrum travels faster than the 'red' edge through the grating arrangement. The first grating serves the purpose of dispersing the spectral content of the pulse and hence the negative GVD, and the second grating recollimates the different wavelengths. Martinez (1987) designed a compressor with dispersion opposite to that of the Treacy's design (Figure 3-7(b)). A telescope

placed between a pair of anti-parallel gratings modified the effective length between them yielding positive group velocity besides providing a high magnification yielding compression factors as high as 3000.

The phase shift across the spectrum of the pulse as the beam propagates though the grating pair can be calculated as (Treacy, 1969)

$$\phi(\omega) = \frac{2\pi L_g}{\lambda_0 \cos(\gamma - \theta)}\left[1 + \cos\theta - \frac{\lambda_0}{d}\sin(\gamma - \theta)\right] \qquad (3.6)$$

where L_g is the perpendicular distance between the gratings, γ is the incidence angle, θ is the angle between the incident and the diffracted beams, λ_0 is the central wavelength of the spectrum of the pulse and d is the grating constant. One can derive the group velocity dispersion (GVD) from the above equation

$$\frac{\partial^2\phi}{\partial\omega^2} = \frac{\partial\tau}{\partial\omega} = -\frac{4\pi^2 c L_g / \cos(\gamma - \theta)}{\omega^3 d\left[1 - \left(\frac{2\pi c}{\omega d} - \sin\gamma\right)^2\right]} \qquad (3.7)$$

The expression for GVD for the Martinez stretcher (Figure 3-7 (b)) is the same as eq.(3.7) except with an opposite sign. The above expression is for a single pass through the grating pair. The beams are made to pass once again through the arrangement to remove the wavelength dependent spatial walk-off, by reflecting them off a retro-reflector or a pair of mirrors used in a roof geometry. Due to the ease of their construction the stretcher and the compressor are designed in such a way as to exactly reproduce the input pulse temporally.

Martinez et al. (1984), showed that negative GVD can also be generated from a pair of prisms arranged in parallel. While the reflective grating geometry as in Figure 3-7 (b) is not an easily adjustable design the prism arrangement in Figure 3-8 provides both low loss as well as tunability from negative to positive values of GVD and hence is incorporated into the mode-

locked Ti: sapphire oscillator to compensate for the varying pulse GVD which is alignment dependent. It is based on the idea that wavelength dependent phase delay caused by angular dispersion always yields negative GVD.

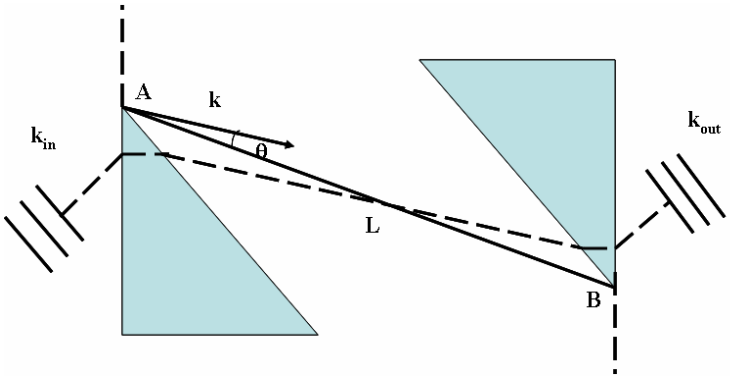

Figure 3-8: Prism delay line. A pair of parallel prisms generates negative GVD that can be varied by changing the distance between the prisms (Martinez, 1984; Fork, 1984).

In the Figure 3-8, the optical path between the points A and B is

$$\Delta = \phi c/\omega = nL\cos\theta \qquad (3.8)$$

The GVD term is given as

$$\frac{d^2\phi}{d\omega^2} = \frac{\lambda^3}{2\pi c^2}\frac{d^2\Delta}{d\lambda^2} \qquad (3.9)$$

Substituting for Δ from equation (3.8) in equation (3.9) and calculating the GVD along the direction of the wave vector $(\theta = 0)$ yields

$$\frac{d^2\Delta}{d\lambda^2} = \left[\frac{d^2n}{d\lambda^2} - n\left(\frac{d\theta}{d\lambda}\right)^2\right]L \qquad (3.10)$$

The above expression yields a negative GVD regardless of the sign of the term $d\theta/d\lambda$. The first prism, as in the case for the grating pair, causes the angular dispersion and the second prism serves to recollimate the different wavelengths. The net dispersion is also easily adjustable by

translating one of the prisms normal to the incident beam without altering the optical alignment. This allows for the introduction of material dispersion without changing the negative GVD.

For amplified pulse duration < 35-40 fs, getting rid of the residual phase over a large spectral bandwidth becomes a formidable task due to the mismatch of the compressor i.e when it is not able to compensate completely the chirp introduced in the stretching and the amplification process. The all-refractive stretcher design by Martinez et al. (1987) introduces strong chromatic aberrations (a wavelength component that diffracts from the first grating at an angle of θ must arrive at the second grating at the same angle) inevitably causing a mismatch between the dispersive delay lines in a CPA. A. Offner (US Patents, 1971) came up with an all-reflective triplet combination that reduces the effects of chromatic aberration. When used as a stretcher, this design makes it possible to recompress amplified pulse to near transform-limit. The Offner triplet consists of a single grating and the refractive unit magnification lens telescope in the traditional stretcher design by Martinez is replaced with two concentric spherical mirrors, one concave and the other convex. The use of spherical mirrors reduces the aberrations to only spherical order, which in turn are further reduced owing to the fact that the ratio of their radii of curvature is two and they are of opposite signs. Although any deviation of the grating from the center of curvature (Gill and Simon, 1983) of the two mirrors, causes astigmatism leading to degradation in the temporal pulse profile.

Cheriaux et al. used a slightly modified version of the Offner triplet in their stretcher design for their CPA system (1996). Although they had to place the grating out of the plane of curvature for stretching purposes, the spherical aberrations as a result of this arrangement were calculated to be very small such that the temporal shape of the pulses remained unchanged. Their calculations also indicated that the spherical aberrations were significantly less severe than a

slight misalignment of the components in Offner's triplet design. Further improvisation to the stretcher design by Cheriaux et al., (1996) M. B. Mason et al. (2000) came up with an all-reflective doublet geometry (Figure 3-9) that lets the diffraction grating lie at the aberration-free position in a stretcher configuration, enabling nearly perfect recompression of the broadened pulses. It has the capability of achieving large stretch factors with over-sized optics while totally eliminating any aberrations to the pulses.

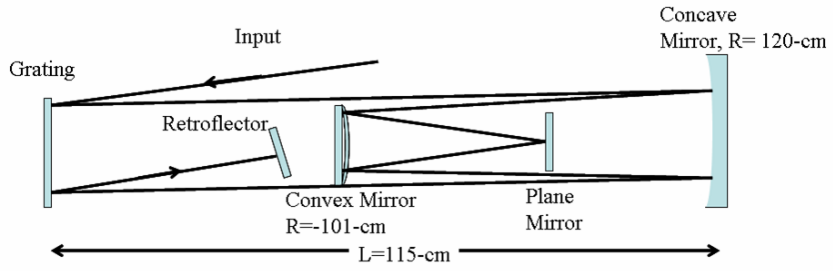

Figure 3-9: Schematic of the stretcher layout. Oscillator pulses of duration ~20 fs are stretched to ~ 200 ps without any chromatic aberrations.

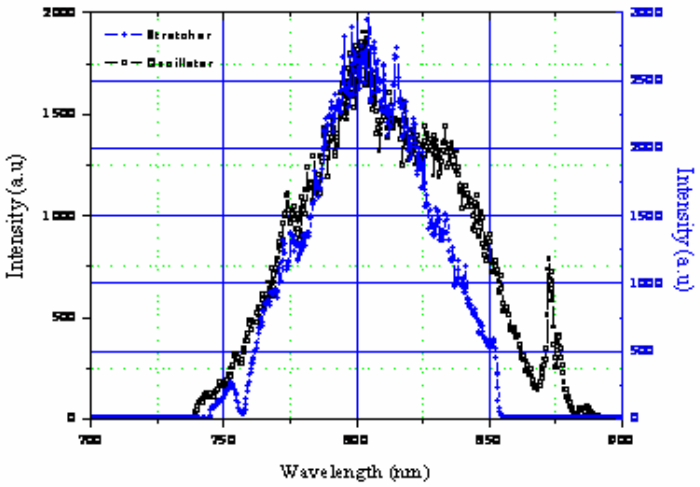

Figure 3-10: Spectrum measured from the oscillator and after propagation through the pulse stretcher. Spectral clipping on the red side of the spectrum is due to insufficient width of the optics in stretcher.

The stretcher in our CPA system uses the Mason doublet design to achieve stretch factors as high as 10^4. The pulses from the oscillator are broadened to ~200-ps. Pulses are incident into the stretcher at an angle of 8.24° (close to Littrow angle). We use an 8-inch diameter concave

mirror of radius of curvature of 120-cm to set a band-pass limit of ~100 nm on the spectrum of the seed pulses. A convex mirror of radius of curvature 101-cm is placed about 70-cm from the concave mirror. This arrangement produces an effective length (L_g, as in eq.(3.7)) of 121-cm. A schematic of the stretcher setup is given in Figure 3-9. Some spectral clipping (Figure 3-10) is observed in spite of the use of large optics in the stretcher.

For ideal compensation the incident angles and the effective lengths for the stretcher and compressor must be close. But the incident angle for the compressor in our setup is 18° and the effective length is about 125 cm. This is to account for the material dispersion and the higher order dispersion terms added to the total phase of the pulse due to the amplification process.

3.7 Ti: Sapphire based Laser Amplifier

Amplifying femtosecond pulses in the milli-joule range was once only possible using dye-amplifiers (Knox, 1988). Ti: sapphire based regenerative amplifier was first introduced in 1991 by J. Squier, et al. following the introduction of Ti: sapphire based laser oscillators by Spence et al. (1991). These systems demonstrated a two-fold increase in the pulse energies. Also due to their wide tunability and low background as compared to the dye amplifiers, it was possible to generate more than 2 W of average power from Ti: sapphire amplifiers at a repetition rate of 10 kHz (Squier et al., 1993). Due to the low pulse energies of the order of micro-joules in high repetition rate pump lasers, low repetition rate systems soon grew more popular as pulse energies as high as a joule were available at a repetition rate of 10 Hz (Sullivan et al., 1991; Zhou et al., 1995). A few millijoules of amplified pulse energy were attainable at 1 kHz repetition rate (Vailliancourt et al., 1990; Backus et al., 1995). When high average power pump sources became available, pumping water-cooled Ti: sapphire crystal in the amplifier cavity generated huge thermal loading which then limited the pulse energies to a few micro-joules in high

repetition rate CPA systems. As the pump power is increased to achieve large amplification factors, the residual heat in the Ti: sapphire crystal gives rise to deleterious effects that influence pulse energies and mode quality, limiting the overall efficiency of the system. Specifically, the thermal gradient generated within the crystal due to the pump beam, consequently gives rise to a gradient in the index of refraction of sapphire that causes the crystal to act as a positive lens (De Franzo and Pazol, 1993; Moulton, 1986).

Moulton (1986) and later Schulz and Henion (1991) observed that the thermal properties of sapphire improved upon cooling to 93 °K. They noted that calculations of the thermo-optic aberrations indicated an increase in the output power capabilities of a Ti: sapphire laser by 200 times at 77 °K than at room temperature. Several groups have since developed high brightness, high repetition rate ultrafast laser systems which mitigate or circumvent these thermal effects. Backus et al. (2001) produced a millijoule level, femtosecond single-stage multi-pass chirped pulse amplifier at 7 kHz repetition rate utilizing cryogenically (LN_2) cooled Ti:sapphire crystal. By cooling the crystal to temperatures near 77 K, a forty-fold increase in the thermal conductivity (Touloukain et al., 1973; Holland, 1962) and five-fold reduction in the temperature dependent refractive index term (dn/dT) at low temperatures (Feldman et al., 1978) is obtained. Zhavoronkov and Korn (2004) demonstrated single-stage regenerative Ti: sapphire amplification at multi-kilohertz repetition rate to powers of 6.5 W at 20 kHz, using thermoelectric cooling to 210 K and a cavity design that takes into account the strong astigmatic thermal loading of the Ti: sapphire rod. Zhou, et al. (2005) have used two stages to avoid large thermal loading present in single-stage systems to generate 7 W of average power at a repetition rate of 5 kHz.

3.7.1 Process of Amplification

Optical amplification occurs in a medium where the equilibrium configuration of the system comprises of its atoms or molecules in a state with higher energy content as compared to the ground state of the system. This electronic exchange between the two energy states is achieved by an external pump source. Amplification occurs when an electromagnetic wave of appropriate frequency passes through such an 'inverted' medium, resulting in a release of photons as the atoms drop back to a lower energy state, thereby extracting energy from the system. The gain of the amplifying medium is defined as the ratio of the output intensity to that of the input intensity. For a gain curve or emission line shape g_0 of a laser medium of length L, the gain in energy through a single pass is expressed as

$$G_0 = e^{g_o L}$$
$$g_0 = n\sigma \tag{3.11}$$

where *n* is the population density in the upper energy level of the system and σ is the gain cross section. For successive passes through the amplifying medium, the energy content in the seed pulse grows exponentially. This exponential increase in the gain with increasing paths through a laser medium with limited gain bandwidth leads to narrowing of the amplified spectrum as the central portion of the spectrum experiences more gain as compared to the spectral components on the wings. Figure 3-11 (which is a schematic) illustrates an amplified pulse that undergoes gain narrowing in the amplifier upon multiple round trips within the laser cavity. To circumvent this, the amplifying medium should have a very broad gain bandwidth, such that in spite of the gain narrowing effect, the amplified pulse bandwidth is still quite significant.

Just as the amplified bandwidth depends on the gain narrowing effect, the gain saturation effects in the amplifier limit the maximum energy of the amplified pulse. As the energy of the input pulse increases with each pass through the amplifying medium, the number of photons

extracting energy from the medium becomes comparable to the population density in the upper level of the host material. Consequentially the amplifier's gain falls lowering the energy of the amplified pulses after it reaches the peak attainable gain in the cavity.

For a homogeneously broadened medium, the gain saturation is expressed as

$$g = \frac{g_0}{1 + E/E_{sat}} \tag{3.12}$$

where, g_0 is the small signal gain coefficient, E is the signal fluence and E_{sat} is the fluence of the amplifying medium.

This effect is less pronounced for materials with large saturation fluence such as the Ti: sapphire (E_{sat} = 0.9 J/cm^2). While gain narrowing determines the amplified bandwidth and hence the pulse duration, gain saturation effect determines the pulse energy and these effects often dictate the type of amplifiers (either regenerative or multipass) one may need.

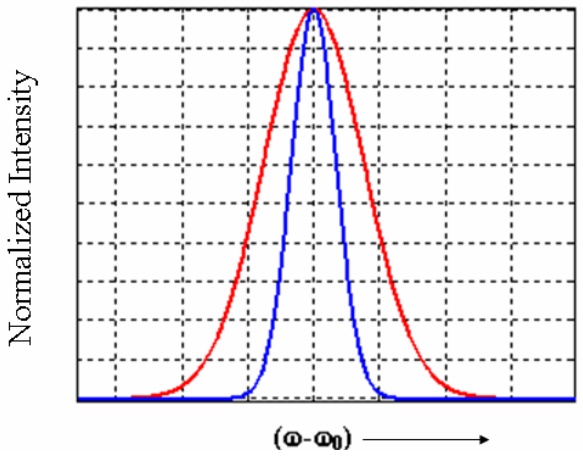

Figure 3-11: Effect of gain narrowing in amplifiers, the red curve is the fundamental laser spectrum and the blue curve is after five passes through the laser medium.

3.7.2 Types of Amplifiers

Amplifiers can be classified into two broad categories: Multipass and Regenerative amplifier systems.

In a multipass amplifier as in Figure 3-12 (the exact geometry may vary from system to system) (LeBlanc et al., 1993; Zhou et al., 1994; Backus et al., 1995; 2001; Lenzer et al., 1995) the seed pulse is made to pass through the gain medium just a few times and each time it follows a different path through the laser medium everytime. For media with a high gain co-efficient and where the pump power is not an issue, the multipass system is often the best scheme of amplification. One can get around the effects of gain narrowing with just a few roundtrips within the multipass amplifier cavity while achieving a high output power. This configuration limits the amount of gain that can be extracted from the medium and hence is suitable only when the energy of the input pulse is high enough to begin with.

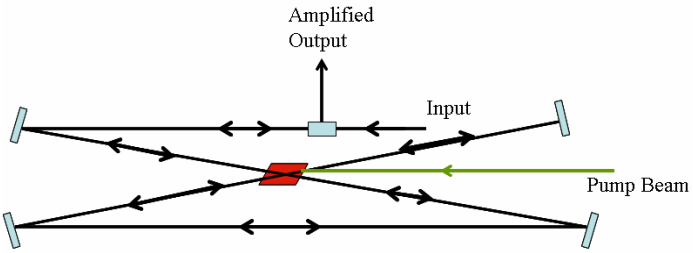

Figure 3-12: Schematic representation of a multipass amplifier system. The seed pulses pass the gain medium several times but through a different path each time.

On the other hand a regenerative amplifier allows one to achieve very high gain factors on the order of 10^5-10^6 (Wynne et al., 1994; Barty et al., 1996; Zhavoronkov et al., 2004; Ramanathan et al., 2006). Hence pulse energies of the order of a millijoule can be realized with input seed pulse energy as low as a few nanojoules, as is obtained from a mode-locked Ti: sapphire oscillator. Figure 3-13 is a schematic representation of the regenerative amplifier in our lab. One of the main advantages of a regenerative amplifier is it's a laser cavity configuration which determines the spatial profile and the pointing of the amplified beam. It is capable of delivering highly energetic pulses with excellent beam quality. Although one of its major drawbacks is that due to the high gain per pass and since the number of passes is usually large to

obtain high factors of amplification, the effect of gain narrowing restricts the bandwidth of the amplified pulses. In addition, amplified spontaneous emission can deplete the gain faster than the seed pulse. Thus systems that generate ultrashort pulses in the 1-10 mJ range often use a high gain preamplifier followed by one or two power amplification stages.

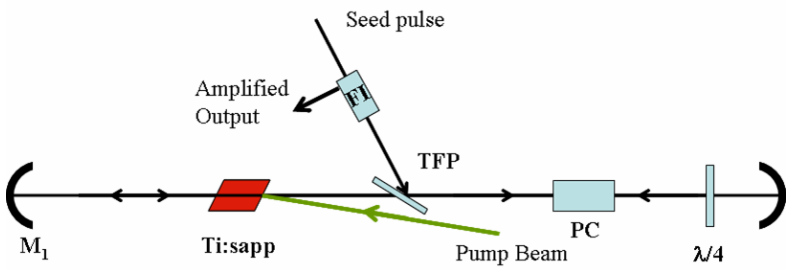

Figure 3-13: A schematic representation of the regenerative amplifier in our laboratory. The seed pulses are injected through a Faraday Isolator (FI) and reflected off a Thin film Polarizer (TFP). The pockel cell (PC) and the λ/4 waveplate confine the seed pulses for ~250 ns (15-16 roundtrips) in a cavity formed by mirrors M1 and M2. The amplified output is obtained through the other exit in the FI.

But with the advent of high average power pump lasers such as the diode pumped solid state lasers, using high thermal conductivity crystals such as the Ti: sapphire, it is now possible to generate millijoule level pulses at kHz repetition rates in a single amplifier stage (Backus et al., 2001; Zhavoronkov and Korn, 2004; Ramanathan et. al., 2006).

The effects of gain narrowing and gain saturation could be curbed to a certain extent by shaping the spectral amplitude of the seed pulses before injection into the amplifier cavity or during the amplification process. For positively chirped pulses in the amplifier, the leading edge or the 'red' edge of the pulse spectrum can experience a higher gain as compared to the 'blue' or the trailing edge of the spectrum. In the past etalons were placed within the amplifier cavity to compensate for the gain narrowing effects. Barty et al (Barty et al., 1996) used 3-μm thick air spaced etalon in their regenerative amplifier cavity to obtain a ~15% increase in the amplified bandwidth thereby measuring 18 fs pulses on compression. Specialized filters have been used in

the amplifier cavity to generate spectrally dependent losses such that the maximum gain around 800-nm is reduced and distributed over the wings of the gain curve. Bagnoud and Salin (2000) used a 580-μm thick birefringent filter to increase the spectra of the amplified pulses from 30-nm to ~50-nm. More recently Takada et al (2006) designed a multilayer dielectric film to introduce losses near the peak of the gain curve of Ti: sapphire, generating 12-fs pulses directly from a 1kHz repetition rate CPA system. But the usage of filters and etalons reduce the pulse energy as they rely on gain losses to increase the bandwidth of the amplified pulses.

3.8 Pulse Shaping

Pulse shaping techniques wherein an input pulse with a slight 'lean' in its spectral content towards the wings of the gain curve could offset the gain narrowing effect and lead to broader bandwidth with low pulse energy losses. Spatial light modulators (SLM) that serve as amplitude and or phase masks when placed in a zero-dispersion standard *4f* stretcher, serves as a pulse shaping devise for ultrashort pulses (Omenetto et al., 2001; Efimov and Reitze, 1998; Efimov et al., 1995). The SLM placed in the Fourier plane between the two lenses of the stretcher setup as in Figure 3-7(b), allows one to write complex amplitude and phase masks that when applied to an ultrashort pulse can generate arbitrary amplitude and phase profile.

Verluise et al (2000) demonstrated an acousto-optic programmable dispersive filter (AOPDF) or commonly known as the Dazzler as a pulse shaping device. Unlike the SLM pulse shapers, the dazzler is based on the acousto-optic interaction and does not need to be placed in a Fourier plane of a zero dispersion stretcher setting, making it a highly compact device. When placed between the stretcher and the amplifier, the dazzler can pre-compensate for gain narrowing and saturation effects in the amplifier. Pittman et al (2002) applied spectral and phase correction to the pre-amplified pulses using the dazzler to generate an amplified bandwidth of 51

nm. Figure 3-14 indicates an optimally shaped input pulse spectrum with the dazzler that generates the broadest bandwidth pulses from our amplifier. For more on the principles of operation of the dazzler system, consult Appendix B.

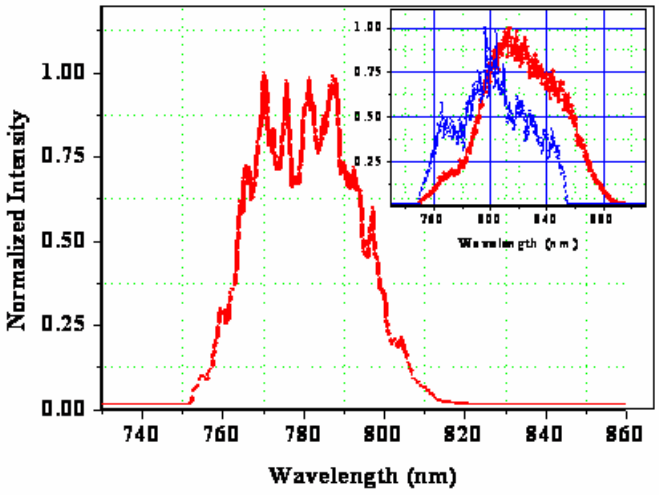

Figure 3-14: Amplified pulse spectrum shows a FWHM of 33-nm. Inset, blue curve is the shaped oscillator spectrum using an AOPDF, which yielded an amplified bandwidth of 33-nm, obtained from the original oscillator spectrum (red curve).

3.9 Ultrashort Pulse Measurement

Since electronic devices have response times that span a few nanoseconds to few picoseconds, they cannot be used to measure the temporal characteristics of an ultrashort pulse. In order to measure an event as short as few femtoseconds, we need a probe that is either shorter or the same duration as the event itself. The only way then to measure a femtosecond pulse, is to use the pulse to measure itself! The most common method to measure ultrashort pulse has been the auto-correlation method devised by Maier et al. (1966). The ultrashort pulse to be measured is split into two using a 50-50-beam splitter. The optical set up is similar to the Michelson Interferometer where one of the beams traverses a fixed path length through one of the arms of the interferometer and is known as the reference beam, the probe beam on the other hand passes through a delay stage (Figure 3-15). The two beams are then focused and spatially overlapped

on to a nonlinear crystal that generates a second harmonic generation (SHG) signal. The SHG signal which is twice the frequency of the fundamental beams is then measured as a function of the delay time τ between the two pulses. The field envelope of the second harmonic signal is then the product of the electric fields of the two pulses

$$E_{SHG}(t,\tau) \propto E(t)E(t-\tau) \tag{3.13}$$

If the two beams have an intensity distribution as $I(t)$ and $I(t-\tau)$, the auto-correlation of the two pulses is

$$\begin{aligned} &I_{SHG}(t,\tau) \propto I(t)I(t-\tau) \\ &\Rightarrow I_{ac}(\tau) = \int_{-\infty}^{\infty} I(t)I(t-\tau)dt \end{aligned} \tag{3.14}$$

The measured auto-correlation signal $I_{ac}(\tau)$ then gives us an estimate of the duration of the measured ultrashort pulse. It is evident from the above equation that the auto-correlation technique cannot uniquely determine the temporal phase structure of the pulse. For a given intensity profile as measured by the auto-correlation technique, one can construct several different pulses with different phase structures (Chung and Weiner, 2001).

To be able to determine the temporal phase of the pulse, one needs to know the frequency domain phase of the pulse along with its magnitude. But as the auto-correlation yields only the Fourier-transform magnitude, it represents a classic case of the unsolvable 1-D phase retrieval problem (Akutowicz, 1956; 1957).

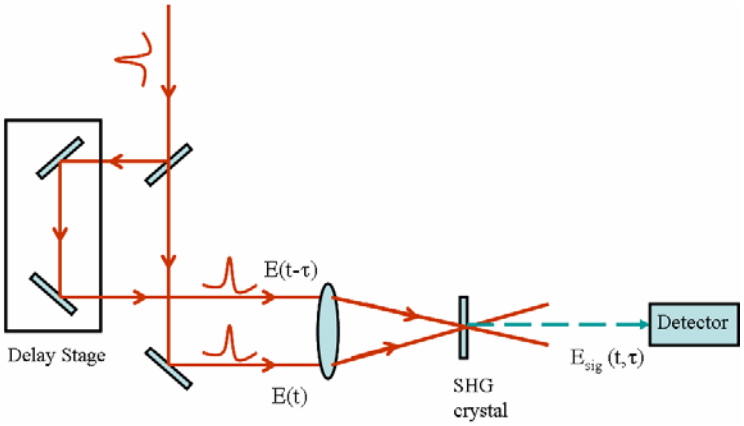

Figure 3-15: Experimental auto-correlator set up. The pulse to be measured is split into two; the pulses that are delayed with respect to each other are focused on a SHG crystal and measured in a detector.

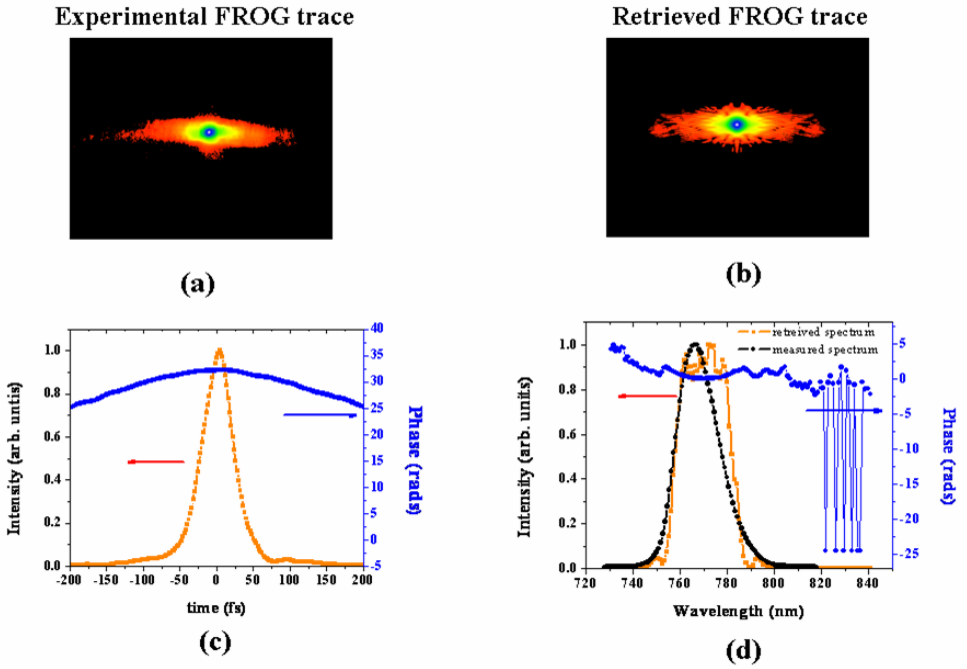

Figure 3-16: FROG: (a) experimental spectrogram, (b) Retrieved spectrogram with a Frog error of 0.002, (c) 43 fs pulsewidth and (d) spectrum from the retrieved Frog trace.

In the early 1990s, Trebino and Kane (1993) resorted to make the phase retrieval problem a 2-dimensional one wherein it could yield accurate information about the phase of the pulse as well (Stark, 1987). This technique known as the Frequency Resolved Optical Gating (FROG), spectrally resolved the SHG signal in an auto-correlator and the spectrogram obtained then uniquely determines the temporal pulse width and the corresponding phase by using a phase

retrieval algorithm. The spectrogram is a 2-dimensional representation of the pulse as a function of frequency and time delay $\left(S\left(\omega,\tau\right)\right)$. For a more detailed explanation of this technique refer to appendix A at the end of this dissertation.

$$S\left(\omega,\tau\right)=\left|\int_{-\infty}^{\infty}E(\omega_0)E(\omega-\omega_0)\exp(i\omega\tau)d\omega\right|^2 \qquad (3.15)$$

Figure 3-16 (a) and (b) is the experimental and retrieved FROG traces respectively for a compressed pulse from the CPA system in our laboratory and (c) and (d) is the retrieved temporal and spectral profile with the phase structure in the respective domains for a 43-fs pulse.

3.10 Chirped Pulse Amplifier system

The single stage chirped pulse amplifier system in our laboratory (Figure 3-17) employs a Coherent Corona laser, capable of generating 12-mJ pulses at an average power of 80 W at a repetition rate that can be varied from 1-25 kHz to pump a 5mm × 6 mm Ti: sapphire crystal. 20-30 fs pulses from a home-built Ti: sapphire oscillator is stretched to ~200 ps before injection into the amplifier. The crystal in the regenerative amplifier is placed in a cryogenic vacuum chamber and cooled to 87 °K by the use of liquid nitrogen. Two Faraday isolators placed in the beamline prevent the backtracking of the amplified pulses into the oscillator. Two spherical mirrors of radii of curvature 1 and 2m (high damage threshold custom coating from Rocky Mountain Inc.) form the regenerative amplifier cavity. The seed pulses are introduced into the amplifier via reflection off a thin film polarizer (Alpine Research Optics). A sol-gel coated Pockels cell (KD^*P) and a quarter waveplate combination help retain the amplified pulses for ~240-ns (15-16 roundtrips) within the amplifier cavity. The Pockels cell helps switch the amplified pulses out of the amplifier. The crystal is double pumped with roughly a total of 60 W of 532-nm light from both sides. An average amplified power of 6 W (1.2 mJ pulse energy) at 55 W of pump power

and 9 W (1.8 mJ pulse energy) at 80 W of pump power at 5 kHz repetition rate is obtained. The pulses are then magnified by an *8f*-telescope system before compression to minimize the risk of damage to the compressor gratings. The energy of the compressed pulses drops to 0.7 mJ and 1.3 mJ at 55 W and 80 W of pump power respectively due to an efficiency of about 70%, of the compressor gratings.

The amplifier exhibits a variety of temperature related effects such as thermal lensing, thermal birefringence, and stress. Thermal management within the amplifier cavity is of utmost importance in developing a high power, high repetition rate CPA. The next chapter is hence devoted to the understanding of these issues and some techniques adopted to develop a state-of-the-art CPA system.

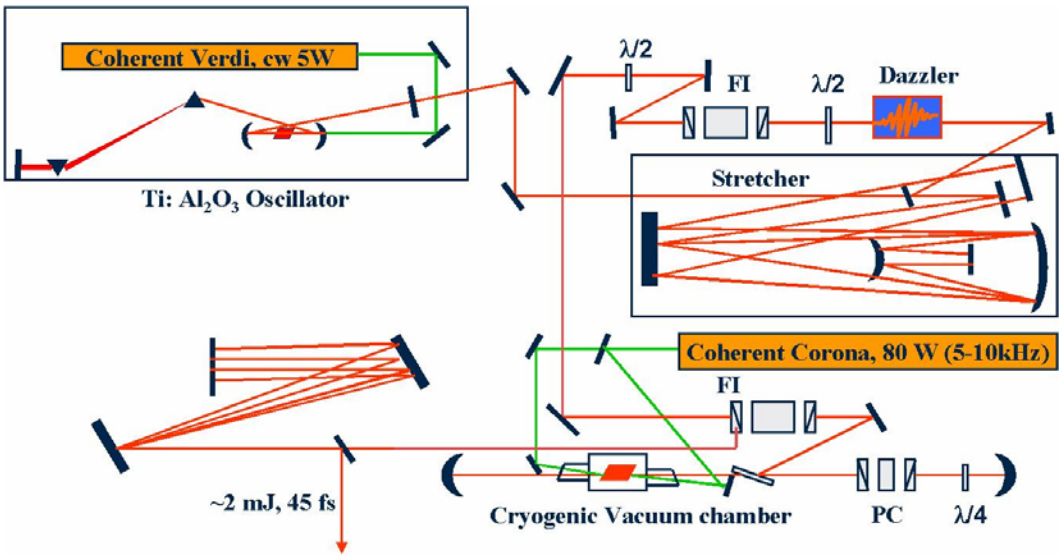

Figure 3-17: Schematic representation of CPA.

3.11 Summary

This chapter was devoted to the discussion of the design and construction of the various components that make a chirped pulse amplifier system in our laboratory. Since the system is a single-stage amplifier, the Ti: sapphire crystal is pumped with a high average power pump

source that gives rise to deleterious thermal issues. The following chapter characterizes these temperature related effects and its effect on the performance of the amplifier.

CHAPTER 4
THERMAL EFFECTS IN HIGH POWER LASER AMPLIFIER

As discussed briefly in the previous chapter, temperature related effects in the regenerative amplifier cavity causes detrimental effects to its performance. This chapter is dedicated to discussing these effects in detail and the steps undertaken to mitigate them to increase the overall efficiency of the system.

4.1 Introduction

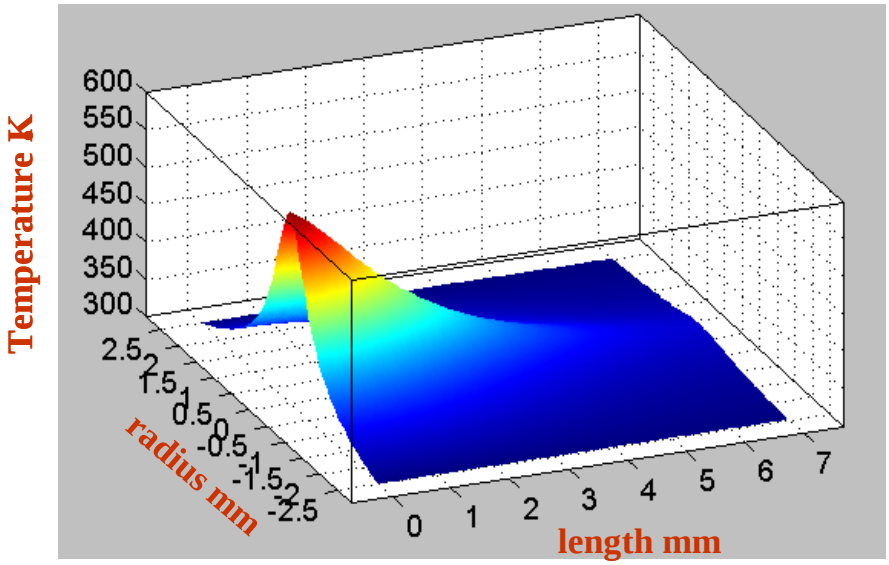

Figure 4-1: Simulation of the resultant temperature gradient in an end pumped Ti Al_2O_3 laser rod at room temperature when pumped by 70 W of 532 nm laser light. Courtesy Jinho Lee.

The output of a Ti sapphire (Ti: Al_2O_3) laser when pumped by 80 W of frequency- doubled Nd: YAG laser of wavelength 532 nm $\left(\lambda_{pump}\right)$ gives rise to a laser output peaked at 800 nm $\left(\lambda_{lasing}\right)$. Ti: sapphire has a wide absorption band in the green spectral region with significant absorption at 532-nm (figure2-2) due to which it absorbs 85-90% of the incident pump light (the absolute absorption is dependent on the doping levels of Ti^{3+} in sapphire). The quantum defect or the Stokes shift which is the energy difference between the pump photon and the lasing photon $\eta\left(=\lambda_{lasing}/\lambda_{pump}\right)$ is deposited as heat in the crystal. The radial intensity dependence of the beam

is translated into a spatial temperature gradient along the transverse axes in the crystal. This results in a 'hot' area at the center of the crystal as compared to its edges. As an example of the severity of this effect, Figure 4-1 is a numerical simulation of the temperature rise within a crystal whose boundary is maintained at room temperature, when a Gaussian beam of 532-nm source at an average power of 70 W is incident on it. For the sake of simplicity a 6-mm long and 2.5-mm radius cylindrically symmetric crystal was assumed for the simulation which was performed using a Finite Element Analysis package by Comsol Multiphysics or commonly referred to as Femlab. The spot size of the pump beam on the crystal was 500-μm and the absorption parameter $\alpha_{abs}L$ was 2.2. As Figure 4-1 indicates the center of the crystal is about 150 °K above room temperature. This spatial variation in the temperature along the two transverse radial axes alters the refractive index leasing to the following thermal effects (Koechner, 1976)

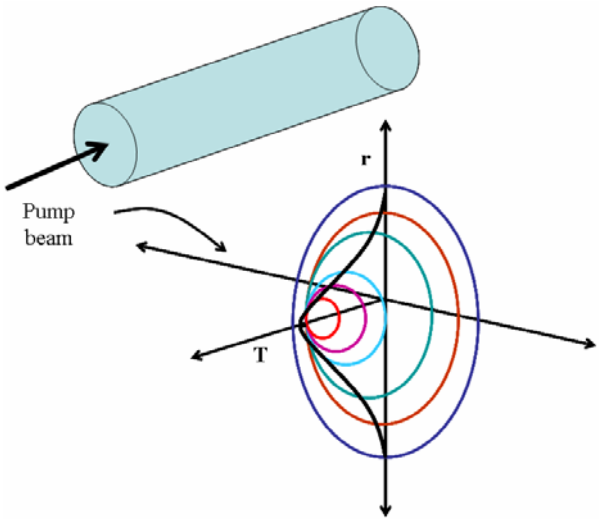

Figure 4-2: Refractive index changes to a crystal incident with 80 W of pump beam. The thermal gradient causes optical path deformation for a beam traveling along the z-axis.

1. **Thermo-optic effect:** The temperature gradient in the crystal changes the refractive index of the laser material along the axes perpendicular to the propagation axis $'z'$ as in Figure 4-2. A laser beam traversing through the crystal experiences a change in the optical path length (OPD) due to the position dependent refractive index $n(r,z)$.

$$\Delta OPD_T = \int_l \Delta n_T dz = \frac{dn}{dT}\int_l \Delta T dz \qquad (4.1)$$

where $\Delta T = T(r,z) - T(r_0, z_0)$, Δn_T is the temperature dependence of refractive index.

2. **Thermo-elastic deformations (Thermal Expansion):** The heat generated by the absorption expands and leads to radially curved end-faces because of the heat generated temperature gradients. The former effect does not affect the focal characteristics of the crystal, but the thermal gradients generate increased focal power (Figure 4-3). This end-face curvature causes a change in the optical path length of a transmitting laser beam.

$$\Delta OPD_e = \alpha \int_l \Delta T dz \qquad (4.2)$$

where α is the thermal expansion co-efficient.

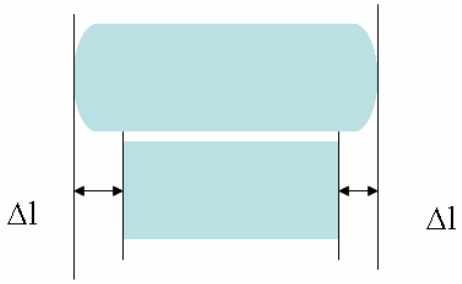

Figure 4-3: Radially curved end-faces due to increase in temperature caused due to absorption of incident pump beam.

3. **Elasto–optic effect:** The temperature distribution $T(r)$ also causes the center of the crystal to expand more rapidly as compared to the cooler outer edges. This generates mechanical stress in laser rod as the center is constrained by the edges of the crystal. The optical path length changes induced due to this effect is given as

$$\Delta OPD_{el} = \int_l \Delta n_{el} dz \qquad (4.3)$$

where Δn_{el} is the photo-elastic coefficients of the crystal.

Thus, the total optical path difference can be calculated as

$$\Delta OPD = \Delta OPD_T + \Delta OPD_e + \Delta OPD_{el} \tag{4.4}$$

These various thermal effects coupled with the fact that thermal constants of sapphire $(\alpha, \kappa, dn/dT)$ are functions of temperature, induce modal distortions in the lasing beam, which restrict the output power from the amplifier cavity besides distorting the shape of the beam. Table 4-1 gives a quantitative comparison of these thermal effects in sapphire indicating that the elasto-optic effects can be safely neglected while calculating the net thermal effects in the Ti: Al_2O_3 crystal (Lawrence, 2003). The comparison made in Table 4-1assumes that the heat incident on the crystal is absorbed uniformly over the entire length of the crystal whose radius *R* is much larger than the beam diameter ω. Considering only radial heat flow between the points $r = 0$ to $r = \omega$, the temperature differences where there is no appreciable change in the thermal constants of the crystal is thus calculated as

$$\delta T = \Delta T\big|_{r=0} - \Delta T\big|_{r=\omega} \approx \frac{P_a}{\kappa(2\pi\omega h)}\omega \tag{4.5}$$

where, P_a is the absorbed power by a crystal of length h, κ is the thermal conductivity. Integrating this quantity over the entire length of the crystal yields

$$\int \delta T dz = \frac{P_a}{2\pi\kappa} \tag{4.6}$$

The relative strengths of the various thermal effects can now be calculated and compared as equation (4.6) indicates that $\kappa/P_a \int \delta T dz$ is a constant for any material for small changes in temperature.

In order to achieve beam quality close to the diffraction limit and higher amplified pulse energies, these optical distortions in the cavity must be eliminated as much as possible. In the

past, numerous methods have been proposed that can lower these distortions (Schulz and Henion, 1991), including:

1. Pumping the crystal at lower powers such that the available heat limits the thermal distortions in the system.
2. Using a slab geometry for the crystal rather than a cylindrical rod design in the amplifier (Koechner, 1976) reduces the heat flow to a one-dimensional problem, which then simplifies the removal of heat.
3. Reducing the quantum defect η (which may be defined as $\lambda_{lasing}/\lambda_{pump}$ or $\lambda_{lasing} - \lambda_{pump}$ by pumping the crystal with a higher wavelength source (Moulton, 1986).

Table 4-1: Quantitative estimate of thermal effects in sapphire.

Thermo-optic effect	1
Thermal expansion	0.8
Elasto-optic effect	0.2

Note Adapted from Lawrence (2003)

For several reasons, the above mentioned measures cannot be easily implemented when designing high average power systems. Pumping the crystal at lower powers reduces the output power of the amplifier. Although a slab geometry produces lower optical distortions, is it found (Miyake et al., 1990) that the cylindrical rod geometry for Ti: Al_2O_3 produces higher powers when cooled to liquid nitrogen temperature. Besides a slab geometry can also give rise to various parasitic modes that can lower the useful stored energy in the crystal (Koechner, 1976). Special coatings to suppress these parasitic modes and to enhance the thermal coupling to the cooling unit can add to the cost and the design complexities of slabs. In addition slab geometries are not easily implementable in regenerative amplifier systems.

The heat generated in the crystal is given by the product of the amount of heat absorbed by the crystal and the quantum defect $\left(H = P_a \times \eta\right)$. Pumping Ti: Al_2O_3 at 600 nm instead of 500 nm

reduces the quantum defect by a factor of two (Schulz, 1991). In order then, to achieve the same absorbed power at 600 nm, the concentration of Ti^{3+} ions has to be increased in the crystal as, the absorption coefficient of Ti: Al_2O_3 is lower for 600 nm as compared to 500 nm (figure 2-2) (Moulton, 1986). Thus high quality crystals must be used to limit losses due to the absorption of the crystal at the lasing wavelength. Most significantly the availability of high-powered pump sources at 600-nm restricts operation at this regime.

This prompts a more detailed study and analysis of the two most damaging thermal effects in Ti: Al_2O_3 to gain a better understanding of the problem so as to be able to suggest remedial measures.

4.2 Theoretical Background

As explained above, refractive index changes of Ti: sapphire with incident pump beam leads to optical distortions. These changes can be separated into temperature- and stress-dependent changes

$$n(r) = n_0 + \Delta n(r)_T + \Delta n(r)_\varepsilon \tag{4.7}$$

where $n(r)$ is the radial variation of refractive index; n_0 is the index at the center of the laser rod and $\Delta n(r)_T$ and $\Delta n(r)_\varepsilon$ are the temperature and stress dependent coefficients of refractive index respectively. Ignoring the effects of the stress-dependent changes (Lawrence, 2003) as per explanation above, $n(r)$ can be expressed as

$$\Delta n(r)_T = \left[T(r) - T(r_0)\right]\left(\frac{dn}{dT}\right) = \Delta T(x, y, z)\left(\frac{dn}{dT}\right) \tag{4.8}$$

This results in an OPD change as given in equation (4.1).

As sapphire exhibits peak absorption at 532-nm, there usually is some physical distortion of the flatness of the rod ends that result in a change of the optical path length of a laser beam that traverses through it. This deviation can be calculated as

$$L(r) = \alpha_0 L_0 \Delta T(r) \tag{4.9}$$

where, α_0 is the coefficient of expansion and L_0 is the original length of the laser crystal. This results in an OPD change as per equation (4.2) . Thus the transverse optical path difference for propagation along the *z*-direction can be written in general as

$$\Delta OPD(x, y) = \int_0^L (n[T(x, y, z)] - 1)\, dz \tag{4.10}$$

Expanding n and dz in powers of ΔT , using equation (4.8) and (4.9) equation (4.10) becomes

$$\begin{aligned} \Delta OPD(x, y) &\approx \int_0^L (n_0 + \frac{dn}{dT}\Delta T - 1)(\, dz + \alpha_0 \Delta T dz) \\ &= \int_0^L \frac{dn}{dT}\Delta T dz_0 + \int_0^L n_0 \alpha_0 \Delta T dz_0 - \int_0^L \alpha_0 \Delta T dz_0 + (n_0 - 1) + O([\Delta T]^2) \end{aligned} \tag{4.11}$$

Neglecting the constant term and terms in $(\Delta T)^2$, the integrated optical path length is then given by

$$\Delta OPD(x, y) = \int_0^L \left(\frac{dn}{dT} + \alpha_0 (n_o - 1) \right) \Delta T(x, y, z)\, dz \tag{4.12}$$

Analytical solutions to the above equation for cylindrically symmetric crystal geometry can be obtained by solving the steady-state heat diffusion equation with the appropriate boundary conditions.

$$-\nabla \bullet \left[\kappa \nabla T(x, y, z) \right] = Q(x, y, z) \tag{4.13}$$

M. E. Innocenzi et al. (1990) solved the heat diffusion equation for an axially heated cylinder with a thermally conductive boundary at the periphery. For an incident pump beam that is Gaussian in nature, the steady state temperature difference is calculated as

$$\Delta T(r,z) = \frac{\alpha_{abs} P_{in} \exp(-\alpha_0 z)}{4\pi\kappa} \times \left[\ln\left(\frac{r_0^2}{r^2}\right) + E_1\left(\frac{2r_0^2}{\omega_p^2}\right) - E_1\left(\frac{2r^2}{\omega_p^2}\right) \right] \tag{4.14}$$

where, P_{in} is the incident pump power, α_{abs} is the absorption coefficient that results in the heating, ω_p is $1/e^2$ radius of the Gaussian pump beam, r_0 is the radius and κ is the thermal conductivity of the laser rod. The expression for $\Delta T(r,z)$ can be obtained by neglecting $E_1\left(2r_0^2/\omega_p^2\right)$ as its small for most practical cases and expanding $E_1\left(2r^2/\omega_p^2\right)$ (Abramawitz and Stegun, 1965) as a power series and retaining only the terms quadratic in *r*. Plugging it into equation (4.1) (their calculations do not include the thermal expansion of the crystal) yields the resultant phase change or the transmitting laser beam of wavelength λ through the crystal

$$\begin{aligned} \Delta\phi &= \frac{2\pi}{\lambda}\Delta OPD(r) \\ \Delta\phi &= \frac{2\pi P_{in}\left(dn/dT\right)}{2\pi\lambda\kappa\omega_p^2}\left[1-\exp(-\alpha_{abs} l)\right] r^2 \end{aligned} \tag{4.15}$$

comparing the above equation to the phase changes that occur in a lens like medium with a quadratic variation in its refractive index (Kogelnik, 1965)

$$\Delta\phi = \frac{2\pi r^2}{\lambda f} \tag{4.16}$$

where, f is the effective focal length. Comparing equation (4.15) with equation (4.16) the effective focal length for the laser rod can be written as

$$f_{th} = \frac{\pi\kappa\omega_p^2}{P_{in}\left(dn/dT\right)}\left(\frac{1}{1-\exp(-\alpha_{abs} l)}\right) \tag{4.17}$$

This effect known as thermal lensing because it alters the modal properties of a beam that transmits through it, just like a static lens but unlike a static lens, it's dynamic in nature due to its implicit dependence on pump power. In an amplifier cavity formed by two spherical end mirrors, this effect can destabilize the cavity as the modal properties of the lasing beam starts to exhibit the same dynamism as the thermal lens in the crystal for various pump power levels. A positive value of dn/dT for a material generates a converging thermal lens and a negative value generates a diverging lens. Although the above equation is calculated for a cylindrical crystal pumped with a continuous laser source, we can nevertheless use it to obtain an estimate of the focal length for a Brewster cut Ti sapphire crystal pumped with a pulsed laser source (Coherent, Corona). The thermal constants for sapphire at room temperature are: $\kappa = 0.33 W/cm^2$ (Holland, 1962), $dn/dT = 1.28 \times 10^{-5} / K$ (Feldman et al., 1978). For a crystal with its boundaries at room temperature and pumped with 60W of green light with a spot of 500-μm on the crystal and a constant pump absorption-length product, $\alpha_{abs} L = 2.2$, yields a thermal lens of focal length $f_{th} \approx 4cm$!

To increase the thermal lens focal length or conversely to decrease the thermal lens power (defined as $1/f_{th}$), the pump power can be decreased or alternatively the pump spot size on the crystal can be increased. Recalculating the focal length for a pump spot of radius 1-mm and a decreased incident pump power of 30 W, increases the focal length to ~ 30-cm. Although reducing the pump power increases f_{th}, but this necessarily decreases the amplified output power. Since a high overlap integral between the pump spot and the lasing beam spot sizes on the crystal is required for efficient energy extraction from the Ti: sapphire in the amplifier. This integral is a maximum when the pump beam is smaller or equal to the amplified beam. Increasing the spot

size ω_p of the pumping beam may alter the overlap integral, again bringing about a reduction in the extracted energy from the amplifier.

Thus to be able to achieve high average amplified power from a regenerative Ti sapphire amplifier cavity the thermal lens effect needs to be either eliminated (ideal solution) or at least minimized (practical solution).

4.3 Methods to Reduce Thermal Effects

In the past, researchers have used various methods to reduce thermal effects in their laser systems. A quick review through some of these measures brings about a deeper understanding of this issue.

The most intuitive method of eliminating or reducing thermal effects in a laser cavity would be to introduce a diverging lens in the beam path to compensate for the induced positive or converging thermal lens generated by the crystal. Due to the variable nature and broad range of the thermal lens, a fixed focal length passive optical element cannot compensate for a range of incident pump powers. Also such an optical element will change the beam diameter on the crystal with each pass, increasing modal distortions in the laser beam.

Salin et al. (1998) introduced the concept of thermal eigenmode amplifiers. A thermally-loaded multipass amplifier is equivalent to a series of lenses separated by a distance L that corresponds to the beam round trip length inside the cavity. An unfolded resonator with two spherically curved mirrors with radii of curvature $2 f_{therm}$, with the crystal at the center is equivalent to a series of lenses of focal length f_{therm} separated by a distance L. An eigenmode of this resonator, calculated from the paraxial Gaussian beam propagation relations, reproduces itself for each round trip, which for a multipass is equivalent to re-imaging the beam onto itself after each pass. If the input beam has the same size and characteristics of the eigenmode of the

resonator then the amplified output beam characteristics are similar to those of the input beam producing diffraction limited amplified pulses. This is suitable when the incident pump power is maintained at a constant value, as any change in this parameter causes a change in the focal length thus changing L. This is also based on the assumption that the host medium is cylindrical, such that the thermal lens is mostly spherical over the entire pump beam diameter and the length between the successive passes is a constant. A Brewster cut rod (Figure 4-4) instead of a cylindrical laser rod generates an aspherical thermal lens and it then becomes difficult to calculate the thermal eigenmode accurately. MacDonald et al. (2000) have reduced the thermal lensing effect in diode-pumped Nd: YAG laser with multiple composite rods. These rods had undoped end caps to remove the part of thermal lens formed due to the bending of the end faces of the laser rod.

Zhavoronkov and Korn (2004) thermoelectrically cooled a 3-cm Ti sapphire crystal in a three-mirror astigmatic regenerative amplifier cavity to 210 °K that took into account the huge positive thermal loading of the sapphire rod. Their single-stage, multi-kilohertz laser was able to generate 6.5 W of average amplified power at 20 kHz repetition rate. While high output powers were obtained, the thermal and thermo-optical constants did not differ significantly from their room temperature values, and it is likely that higher order spatial aberrations were present in the output beam.

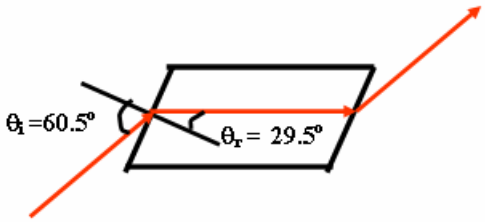

Figure 4-4: Brewster cut Ti sapphire crystal.

Zhou X et al. (2005) used two multipass amplification stages after a regenerative amplifier cavity in order to avoid large thermal loading present in single-stage systems. They were able to generate 7W of average amplified output at a repetition rate of 5 kHz. Although they were able to solve the thermal-loading problem in their CPA system, managing multiple amplifier stages can get cumbersome.

An often used technique to reduce thermal lensing in high power continuous wave Nd:YAG laser systems (Graf et al., 2001; Wyss et al., 2002; Mueller et al., 2002) can be incorporated to compensate for thermal effects in single-stage high repetition rate systems. The idea is to use self-compensating (adaptive) methods to thermo-optically compensate for the thermal lens effects that change with changing power. This technique essentially uses adaptive optical devices such as self-adjusting lenses within the laser cavity that can compensate for every single pass of the lasing beam through the cavity. A material with a negative thermal dispersion coefficient is placed in the cavity that generates a power dependent thermal lens that compensates for the positive dn/dT induced by the temperature gradient in the laser crystal. Th. Graf et al. (2001) were the first to successfully use an adaptive negative thermal lens to compensate for the positive thermal lens in a transversely diode-pumped Nd: YAG laser rod. The compensating element must absorb a small fraction of the incident laser power and hence should posses a strong thermal dispersion dn/dT to effectively compensate for the positive dn/dT . This technique has also been extended to correct thermally induced optical path length changes induced by absorption of transmissive optical components such as electro-optic modulators and Faraday isolators, of gravitational wave interferometer (Mueller et al., 2002).

We attempted to extend the concept of thermo-optical compensation to our regenerative amplifier. Curing gels or index matching fluids such as the OCF-446 (Nye Opticals) possesses

the combined advantages of solid materials (no convection) with a strong negative dn/dT . With a negative thermal dispersion value as high as 3.5×10^{-4} °C^{-1} and a large expansion co-efficient of 8×10^{-4} it seems like an ideal candidate as a compensating material with the added advantage of low absorption at the lasing wavelength of 800-nm (< 2×10^{-4} %/μm). Although numerical simulations by Jinho Lee seem to suggest that the thermo-optical compensation method should work for an OCF thickness of ~ 3mm for a pump power of 80 W, but preliminary experiments have revealed the high intracavity peak powers in the regenerative amplifier cavity causes damage to the cell containing OCF 446. It is not clear from these experiments if the damage occurred to the cell holding the OCF or if the OCF itself burns due to the absorption at the lasing wavelength. Redesigning the cavity taking into consideration the OCF or changing the location of the OCF could potentially solve this problem but has not yet been experimentally verified and could possibly be one of the avenues that could further be explored to increase the efficiency of the present amplifier system.

Meanwhile the most efficient and convenient means of reducing thermal effects in Ti sapphire laser crystal in a chirped pulse amplifier is by cooling it to cryogenic temperatures (liquid nitrogen temperature (77°K) or below) (Moulton, 1986; Schulz and Henion, 1991). Sapphire exhibits excellent thermal properties on cooling to low temperatures. The next section delves on how the thermal properties of sapphire can be exploited to reduce the temperature related effects.

4.4 Liquid Nitrogen Cooled Ti Al_2O_3 Laser Amplifier

P.F. Moulton (1986) was the first to demonstrate the advantages of cooling the sapphire laser crystal to liquid nitrogen temperature in a quasi cw laser. He reported an increase in the output power of the laser from 45 mW to 150 mW when the crystal was cooled to 80 °K. He

attributed this effect to an increase in the thermal conductivity of sapphire with decreasing temperature. This idea was then extended by Schulz and Henion (1991) where they investigated the effects of thermal loading on a single-transverse-mode of Ti: sapphire laser cooled to 93 °K and reported a reduction in the thermo-optical refractive index changes by more than two orders of magnitude. They realized an output power from the Ti: sapphire laser that was 200 times larger at 77 °K than at room temperature!

Table 4-2: Thermal properties of sapphire at 300 and 77 °K.

Property	At 300 °K	At 77 °K
Thermal conductivity κ	0.33 W cm^{-1} K^{-1}	10 W cm^{-1} K^{-1}
Thermal dispersion *dn/dT*	1.28×10^{-5} K^{-1}	0.19×10^{-5} K^{-1}
Thermal expansion co-efficient α	5.0×10^{-6} K^{-1}	0.34×10^{-6} K^{-1}

Note: Adapted from Schulz and Henion (1991).

Table 4-2 compares the thermal properties of Ti sapphire at room temperature and liquid nitrogen temperature. Figure 4-5 (a) and (b) show the variation of thermal conductivity κ and dn/dT with temperature, the key parameters in minimizing thermal distortions.

The thermal lens focal length as given by equation (4.17) is directly proportional to the ratio $\kappa/(dn/dT)$. Figure 4-5 indicates that as the temperature is decreased, the thermal conductivity rises steeply, and the coefficient of refractive index with temperature decreases thereby making the ratio of thermal conductivity to dn/dT increase with increasing temperature. This leads to a decreasing thermal power (or an increasing thermal lens focal length). Backus et al. (2001) were able to generate 13 W of amplified output power at 7 kHz repetition rate from a cryogenically cooled single-stage multipass amplifier with good beam quality (measured M^2 of 1.2 and 1.36 along the X and Y axis).

We can now calculate the effective thermal lens focal length [equation (4.17)] of a Ti sapphire crystal at LN_2 temperature using the constants in Table 4-2 for an input pump power of

60 W and a spot size of 500-μm as mentioned above. On doing so, an f_{th} of ~8m is obtained! Thus we find that there is a tremendous decrease in the thermal lens power of about two orders of magnitude on cooling the crystal to 77 °K!

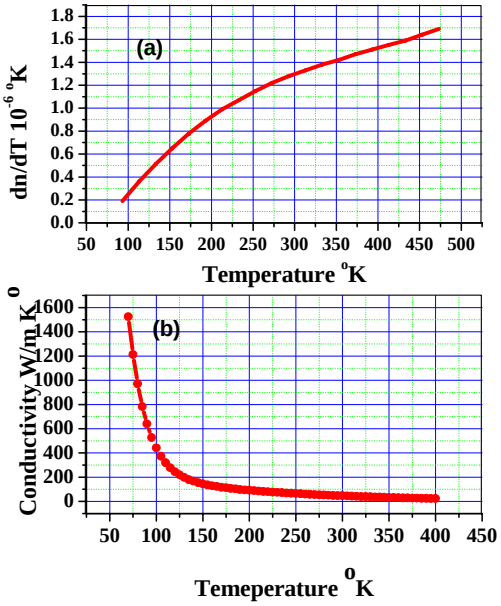

Figure 4-5: Dependence of (a) Thermal dispersion (*dn/dT*) (Feldman et al.,1978) and (b) Thermal conductivity κ (Holland, 1962) of Ti sapphire with temperature.

In order to design an effective regenerative amplifier cavity we accurately need to know the positive thermal lens generated by the crystal with changing pump power. We have made a very detailed study of this, which is elaborated in the remaining sections of this chapter. The next section deals with the construction of a regenerative chirped pulse amplifier since all the experiments and numerical calculation on thermal analysis were performed on this high average power CPA system.

4.5 Construction of a Regenerative Amplifier Cavity

The entire below mentioned discussion has been based on the current amplifier system in our CPA and this section delves into the details of the construction of this amplifier.

A 5-mm diameter and 6-mm long Ti sapphire crystal is the host material in our regenerative amplifier cavity. The crystal is cooled to 87 °K in a vacuum chamber that's placed underneath a liquid nitrogen dewar. The vacuum chamber was designed after extensive consultations with our in-house mechanical engineer Luke Williams. The LN_2 dewar is separated from the crystal by a thin copper wall of thickness ~100-μm. The crystal is held in a copper holder, and a 127-μm Indium foil is sandwiched between the crystal and the thin copper wall for better thermal contact between with the LN_2 in the dewar. A thermocouple placed along one of the edges of the crystal senses the temperature of the crystal at all times. The temperature sensor has an in-built relay circuit to automatically facilitate the turning off of the pump laser when the crystal temperature exceeds 185 °K. Figure 4-6 is a CAD drawing of the vacuum chamber-dewar assembly in our CPA system. As can be seen in the Figure 4-6 (a), the vacuum can has 2 extended arms on either side with brewster windows on it as entrance and exit for both the pump beam and the amplified IR beam. A view-port right in front of the crystal allows one to position the pump beams on the crystal. Figure 4-6 (b) is the copper holder in which the Ti sapphire crystal is placed.

This particular assembly generates almost 0.6 °C rise in temperature per Watt rise in the pump power (Figure 4-7). At zero watts of pump power the crystal temperature as measured by the thermocouple is 90 °K. With almost 65 W of pump power at 5 kHz repetition rate, the crystal temperature rises to about 127 °K when the lasing action within the regenerative amplifier cavity is inhibited and 108 °K when the cavity is in the lasing mode. The higher temperature rise when the cavity is not lasing is due to the absorption of fluorescence by the thermocouple which is considerably decreased during the lasing action. This allows for continuous operation of the regenerative amplifier to repetition rates as high as 12 kHz. The amplified pulse energy drops to

0.3 mJ at 12 kHz repetition rate with considerable disintegration of the beam shape of the amplified pulses (Figure 4-15).

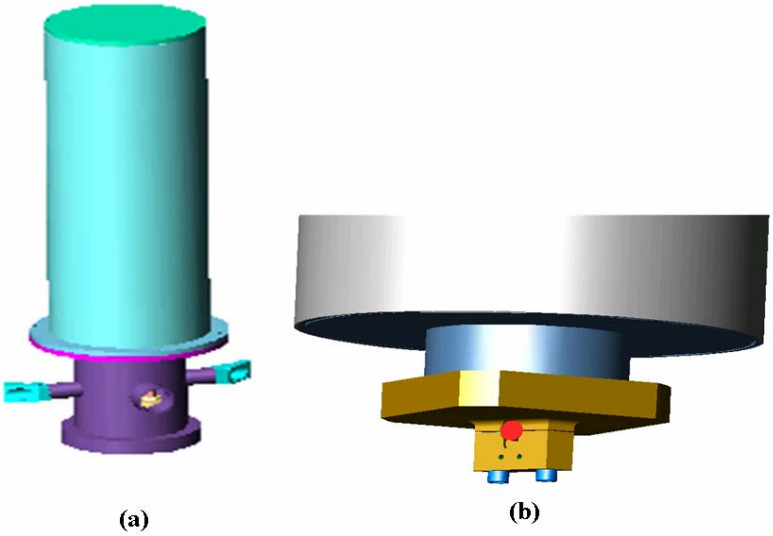

Figure 4-6: CAD drawings depicting (a) Vacuum dewar assembly and (b) copper crystal holder. Drawings by Luke Williams.

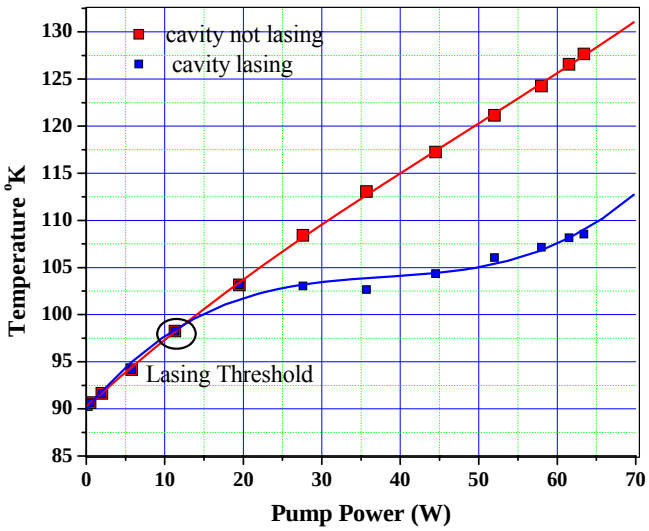

Figure 4-7: Boundary temperature rise as pump power is increased when lasing action is inhibited (red points) and when the cavity is lasing (blue points). The lines are guides to the eye.

4.6 Measurement of Thermal Lens

A laser beam transmitted through a material that acts as a thermal lens undergoes modal changes in its divergence angle relative to the input beam. By measuring these changes, one can

estimate the thermal lens power of the material. The design of an optimum regenerative amplifier cavity necessitates the need to characterize accurately the thermal lens in the Ti sapphire crystal.

To be able to measure the thermal lens in our laboratory we used a He-Ne laser to probe the Ti: sapphire crystal as a function of pump power. The He-Ne laser was mode matched to the pump beam spot on the crystal. The changes in the divergence angle of the beam after traversing the crystal were determined for a series of pump powers by measuring the position dependent spot sizes with a CCD camera. By comparison with the He-Ne beam waist position at zero pump power, the measured waist positions for the non-zero pump powers enabled us to calculate the thermal lens focal length within the thin-lens approximation using the ABCD matrix formulation. In Figure 4-8 is plotted the measured thermal lens power for the two transverse axes as a function of power. For a pump power of about 50-55 W the measured thermal lens focal length is about 1.1 m along the vertical axis on the crystal and 0.2-0.3 m along the horizontal axis. The asymmetry in the thermal lens is immediately evident as the thermal lens power along the horizontal axis rises much sharply as compared to the vertical axis.

An effective amplifier is one where the cavity maintains stability over a wide range of thermal lens power. The ABCD formalism was used in which the crystal was treated as a thin spherical lens. The cavity stability or the g-parameter was calculated for various combinations and permutations of the radii of curvature of the two end mirrors and the distance between them. The most suitable cavity was one that exhibited stability ($-1 \leq g \leq -1$) for a large range of thermal lens, where 'g' is the stability factor. This essentially translates as minimum changes to the spot size of the amplified beam on the crystal. The regenerative amplifier cavity currently being used is 2-m long, comprised of two spherical mirrors of radii of curvature 1-m and 2-m. Figure 4-9 is

a plot of the g-parameter calculated for different values of thermal lens power using the ABCD matrix formulation.

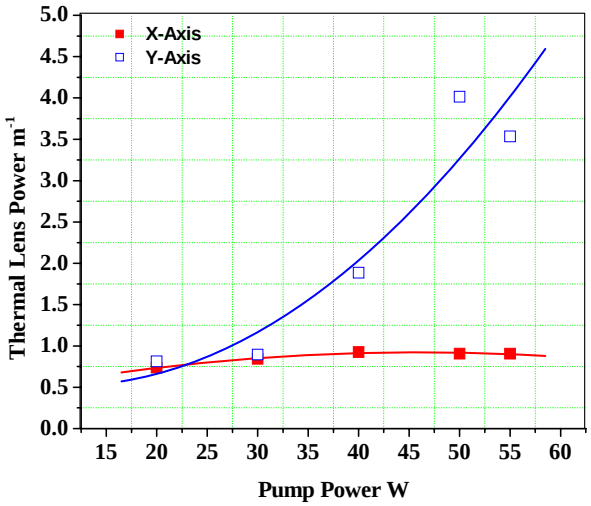

Figure 4-8: Measured thermal lens and thermal power for the two transverse axes; the boundary temperature was measured to be 87 K at zero pump power and 103 K at 55 W of pump power.

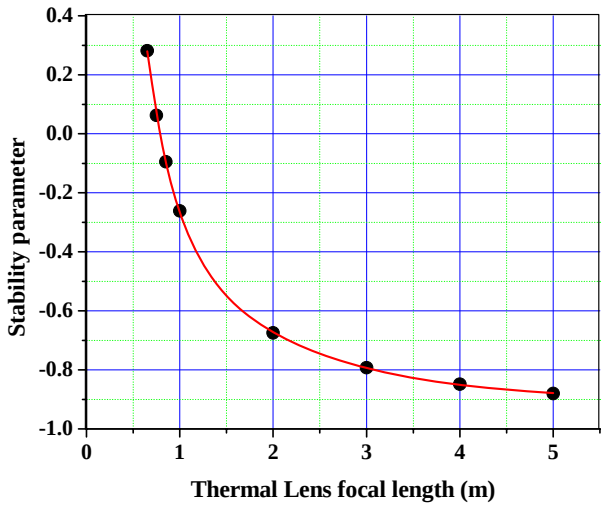

Figure 4-9: Cavity stability parameter as a function of measured thermal lens.

From the above plot, it's clear that the cavity is most stable for a thermal lens focal length values from 0.6-m to 5-m. Also the calculated laser beam spot size ($1/e$ radius) on the crystal shows a variation of about 15% from its minimum value of 343-μm at about 1-m thermal lens focal length. The imaging system of the pump beam on the crystal let us vary the pump spot

from a $1/e$ radius of 200-μm to 800-μm. This ensures a good overlap of the pump beam with the varying mode sizes of the amplified beam on the crystal, for a great range of pump powers.

In order to validate the thin lens approximation in calculating the thermal lens of the crystal as a function of pump power, we invoke the simple lens maker's formula for the effective focal length for both thin and thick lenses.

$$P_{thin} = \frac{1}{f_{thin}} = (n_{lens} - n_0)\left[\frac{1}{R_1} - \frac{1}{R_2}\right]$$
$$P_{thick} = \frac{1}{f_{thick}} = (n_{lens} - n_0)\left[\frac{1}{R_1} - \frac{1}{R_2} + \frac{(n_{lens} - n_0)d}{n_{lens}R_1R_2}\right] \quad (4.18)$$

where n_{lens} and n_0 are the refractive index of the lens medium and the medium in which the lens is placed. R_1 and R_2 are the radii of curvature of the two curved surfaces of the lens of thickness d. The difference in the thermal lens power resulting from the thin lens and the thick lens treatment of the sapphire crystal is given as

$$\Delta\left(\frac{1}{f}\right) = \frac{(n_{lens} - n_0)d}{R_1R_2} \quad (4.19)$$

For a Ti: sapphire of thickness $d = 6mm$ in vacuum and with refractive index, n_{lens}=1.76 and assuming $R_1 = 0.5m$ and $R_2 = -1m$, the change in the focal length is 3.4 × 10^{-3}. Due to the insignificant difference between the two treatments of the crystal thermal lens, it suffices to use just the thin lens approximation in all the calculations using the measured modal changes with pump power.

4.7 Calculation of Thermal Lens

Although cooling to 77 °K brings about a drastic reduction in the thermal lens power of the crystal, it is in practice difficult to achieve boundary temperatures close to the LN_2 temperature when pumping with high laser powers. For a 6-mm thick Brewster-cut sapphire crystal the thin

lens approximation does not accurately describe the thermal lens. Hence to validate the use of the thin lens approximation, we compared the measured thermal lens power with that obtained from a Finite Element Analysis (FEA). An accurate knowledge of the temperature gradient inside the crystal determines the thermal lens accurately.

The temperature gradient is obtained by solving the heat diffusion equation (4.13) with the appropriate boundary conditions. For cylindrically symmetric geometries, pumped with continuous sources, analytical solutions to the heat equation are intuitive (Quetschke et al., 2006). Analytical solutions have also been obtained for crystals pumped with pulsed sources (Lausten and Balling, 2003), however the crystal geometry was again a cylindrically symmetric one. For more complicated geometries such as Brewster cut crystals (Figure 4-4) numerical methods are needed to calculate the temperature gradient inside the crystal. Additionally, the physical quantities in these equations $(\alpha, \kappa, dn/dT)$ are temperature and therefore spatially dependent, and not analytically tractable. Hence we use a finite element analysis package (Comsol Multi-Physics) to model the pump pulse-induced temperature changes and numerically integrate equation (4.12) to compute ΔOPD. Calculations by Jinho Lee show that for a Brewster-cut geometry the source term on the RHS of the 3-D heat equation (4.13) takes the form

$$Q(x,y,z) = \frac{2P\alpha_{abs}}{\pi\omega^2}\cos\theta_i \exp\left(-\frac{2}{\omega^2}\left((y + x\tan\theta_r)^2\cos\theta_i^2 + z^2\right) - \alpha_{abs}\left(\frac{L}{2\cos\theta_r} + \frac{x}{\cos\theta_r}\right)\right)$$

(4.20)

where P is the incident laser power, α_{abs} is the absorption coefficient for the pump, ω is the pump waist ($1/e$ in field), L is the crystal length, and $\theta_{i,r}$ are the incident and refracted angles in the crystal, respectively. Even though the pump source is pulsed the steady state equation perfectly describes the situation as the thermal relaxation constant for Ti: sapphire laser rod is

measured to be ~0.5-secs (Ito et al., 2002) which is much longer than the repetition rate of the laser. Therefore, for pump repetition rates of > 1 kHz, we can safely neglect the time dependence of the thermal gradient.

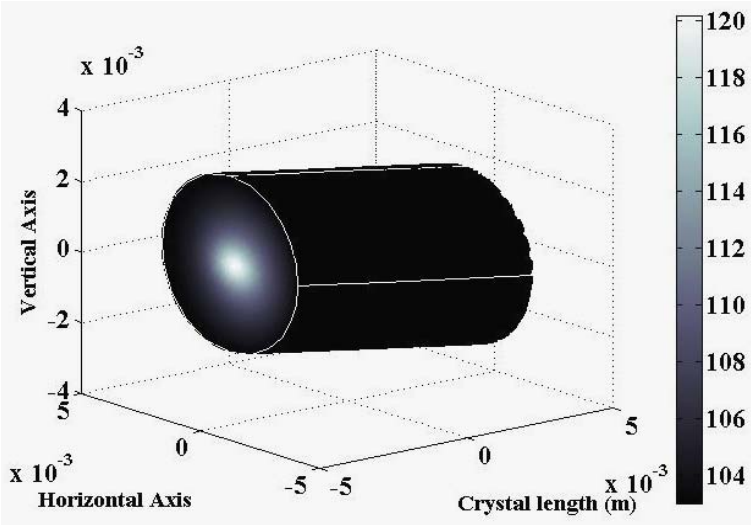

Figure 4-10: Computed temperature profile in a 6 mm long, 5 mm diameter Brewster-cut Ti: sapphire crystal single end-pumped by 50 W in a 0.4 mm pump spot waist radius for and absorption corresponding to $\alpha_{abs}L = 2.2$ and a boundary temperature of 103 K.

The geometry (shown in Figure 4-10) consists of a 3D-tilted cylinder corresponding to our Brewster cut crystal. Temperature dependent thermo-optical and mechanical constants were obtained from Touloukain et al. (1973) and Holland (1962) were fitted over 50 – 300 K. The absorption at the Ti: sapphire emission wavelength was not included as this has a negligible effect on the temperature for Ti:sapphire crystals with high figures of merit ($FOM = \alpha_{532nm}/\alpha_{800nm} \approx 200$; α being the absorption coefficient). The boundary conditions were specified as a temperature T_b along the barrel of cylinder as either a fixed or variable temperature (corresponding to contact with the bath) and on the ends as $dT/d\vec{n} = const$ (corresponding to the radiation). This allowed us to explore more physically realistic scenarios in our amplification

system. Calculating the temperature profile within the crystal, we can now estimate the changes in the optical path length or ΔOPD through the crystal.

The simulated ΔOPD were calculated for an ideal thin lens of the same focal length $f_{x,y}$ in vertical and the horizontal transverse dimensions as that obtained from the simulated temperature gradient within the crystal (Figure 4-11)The experimentally measured thermal lens values from the previous section were then compared to the thermal lens values obtained from the computed OPDs.

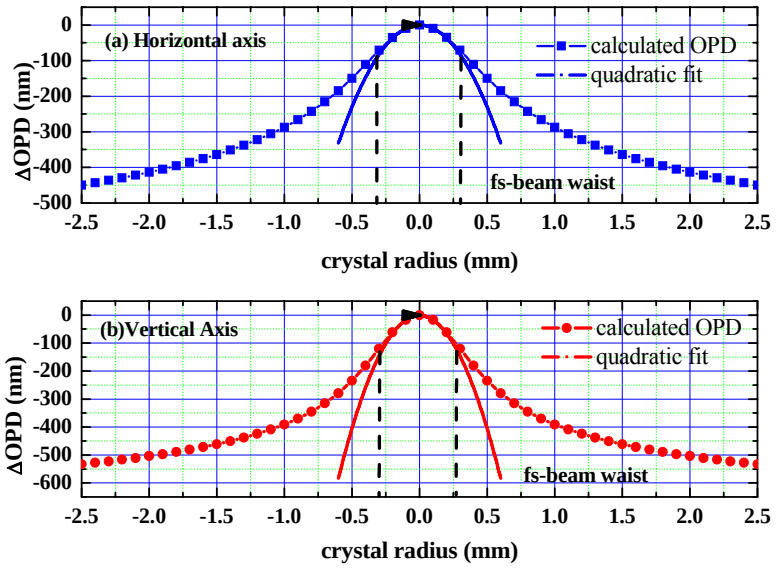

Figure 4-11: Plots (a,b) are the corresponding ΔOPD as a function of the transverse coordinates, for the computed temperature profile in figure (3-6).

These values were also compared with the analytical solution to thermal lens focal length [equation(4.17)] derived by Innocenzi et al. (1990), associated with the phase changes that occur inside a cylindrical laser rod due to temperature dependent refractive index $\Delta n(r,z)$.Figure 4-12, is a plot of the measured thermal lens focal lens power as a function of pump power, compared with the values obtained from the FEA calculations and the expression (4.17) . The κ and dn/dT values used in equation (4.17) corresponded to the maximum computed temperature rise

at the center of the crystal at each pump power. While the FEA calculations agree reasonably well with the measured values along the vertical crystal axis and quite well along the horizontal axis, the focal lens power calculated from Innocenzi's analytical equation significantly underestimates the lens power along both axes.

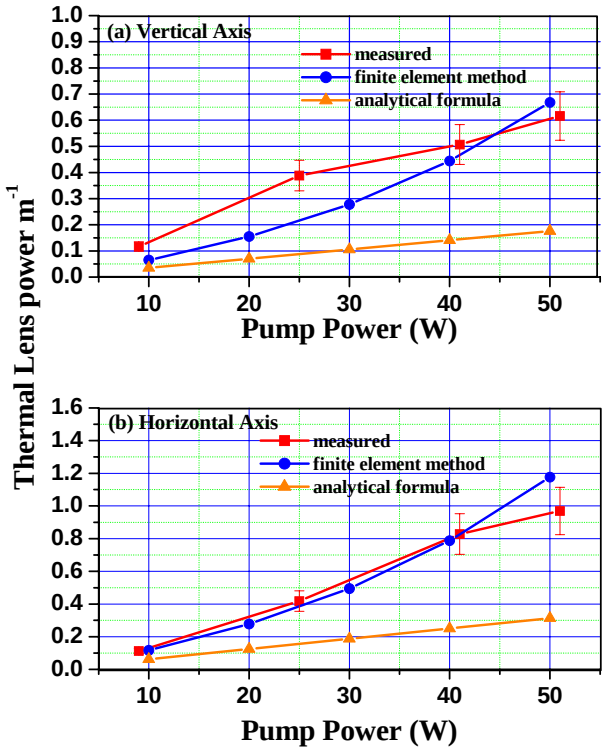

Figure 4-12: Comparison of experimentally measured thermal lens powers (squares) against numerically predicted values using finite element analysis (circles) and an analytical expression for thermal lensing (triangles). Formula derived from Innocenzi et al (1990).

The underestimation by the analytical expression is somewhat surprising, since treating κ and dn/dT as a constant over the entire crystal volume underestimates the effective thermal conductivity and over estimates dn/dT since κ (dn/dT) increases (decreases) as the temperature decreases away from the beam propagation axis. However, equation (4.17) neglects the physical expansion of the crystal, which can increase the thermal lens power by a factor of 1.8 over a pure thermo-optic lens (Lawrence, 2003). Nonetheless, the FEA lens power estimates

agree with experimental data when using boundary temperatures consistent with the experimentally measured boundary temperature values.

This present regenerative amplifier cavity designed with the above measured thermal lens measurement and the FEA analysis has been performing exceptionally well producing average powers as high as 9 W (before compression) when pumped with 80 W of green light at 5 kHz repetition rate.

4.8 Direct Measurement of the Optical Path Deformations

To directly measure the pump induced path length changes and further corroborate our simulations, the LN_2 cooled Ti: sapphire crystal was placed in one of the arms of a Michelson interferometer. A single frequency 1064-nm Nd: YAG laser (Lightwave Corporation NPRO) was split into two arms with the crystal in one arm and free space through the other. The interference pattern was recorded as a function of power on the WinCam CCD beam analyzer. Figure 4-13 is the recorded spatial interference pattern as a function of pump power.

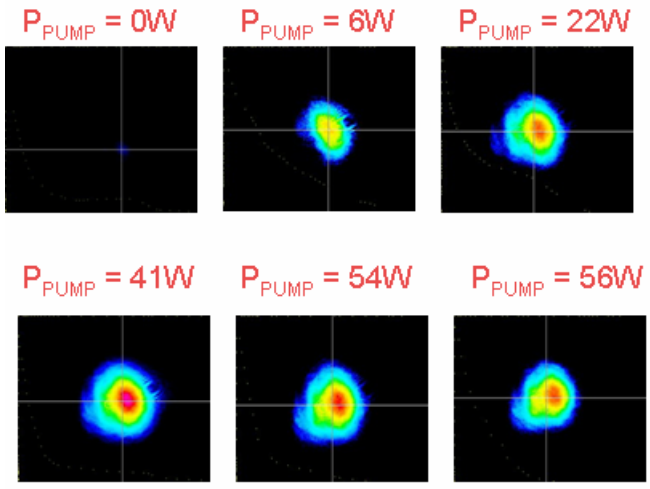

Figure 4-13: Spatial interference pattern in the Michelson interferometer recorded in a CCD camera as a function pump power.

The zero intensity frame corresponds to zero path difference at 0 W of pump power. As the pump power was gradually increased, the change in the intensity of the interference pattern

indicated the increase in the OPD through the crystal. Figure 4-14 is the measured optical path difference obtained from the recorded interference pattern, in the crystal as a function of pump power.

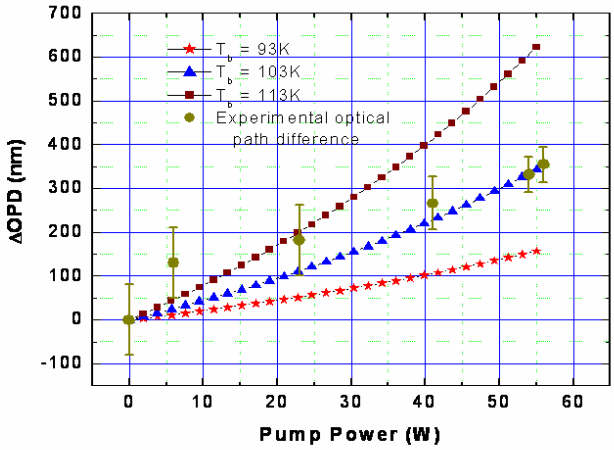

Figure 4-14: Measured OPD compared with the FEA calculated for three different boundary conditions. There is excellent agreement with a boundary temperature of $T_b = 103^{\circ} K$ at higher pump powers.

At the highest pump power (56 W), a ΔOPD of 350 nm +/- 80 nm was measured (or approximately 0.45λ at 800 nm), decreasing as the pump power was lowered. The intensity fluctuation of the NPRO laser $\left(10^2 - 10^3\right)$ as well as path fluctuations caused by acoustic perturbation of the interferometer optics most likely caused the large error bars at lower pump powers. Experimentally, a boundary temperature of 93K was recorded at the boundary for zero pump power. As the pump power was increased to 55 W, a boundary temperature rise of 20K was recorded, but a fraction of this rise was experimentally attributed to the absorption of scattered Ti: sapphire fluorescence by the thermocouple; only a portion of the experimentally recorded temperature rise was due to physical heating at the boundary. Thus, we simulated the ΔOPD for a range of constant boundary temperatures T_b, displayed in Figure 4-14. At the highest pump powers, we see good agreement between the predicted and measured optical path

length for $T_b = 103^\circ K$ (corresponding to 10 °K rise on the boundary), although the data and simulations deviate somewhat at lower temperatures and most severely at the lowest temperature. As expected, the ΔOPD is less severe as the boundary temperature is reduced due primarily to the strong temperature dependence of κ. Figure 4-10 and Figure 4-11displays the computed temperature rise and ΔOPD for a particular boundary temperature $T_b = 103^\circ K$ respectively.

4.9 Effects of Thermal Aberrations on Beam Shape

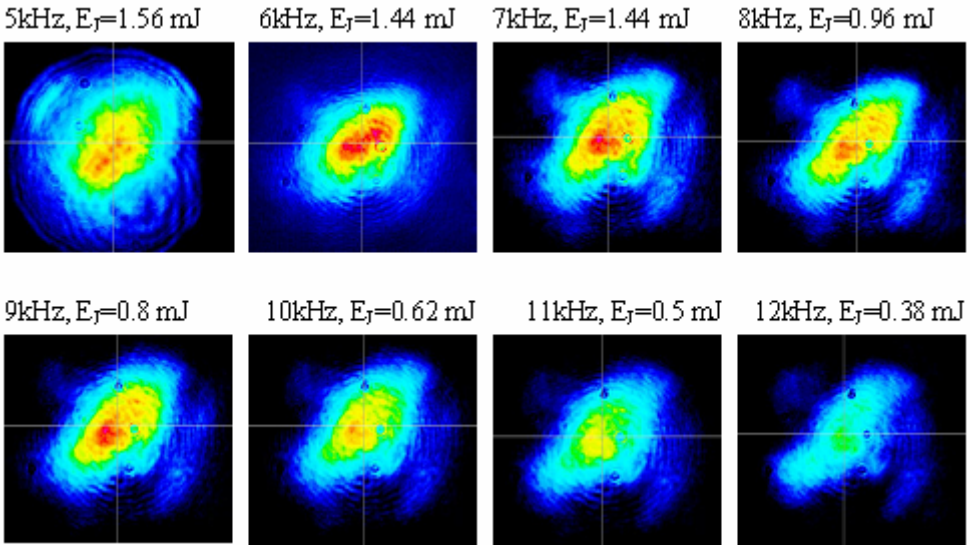

Figure 4-15: Beam shape as a function of repetition rate. Increasing the repetition rate of the pump beam introduces modal distortions.

The spatial quality of the amplified beam is highly sensitive to temperature changes within the crystal. The amplified beam shapes were measured using a WinCamD-UCM CCD beam analyzer after ample attenuation Figure 4-15 is a far field measurement of the spatial profile of the beam with increasing repetition rates.

As the pump power is increased the temperature within the crystal increases leading to increased spatial distortions to the beam profile. The boundary temperature as measured by a thermocouple on the crystal rose from 103 °K at 5 kHz repetition rate to 123 °K at 12 kHz repetition rate. Astigmatism due to the geometry of the crystal is evident in the elliptical shape of

the amplified beam even at a repetition rate of 5 kHz. The mode quality of the amplified beam was measured (5W output power) using the beam analyzer by attenuating it suitably and focusing with a 1 m focal length lens.

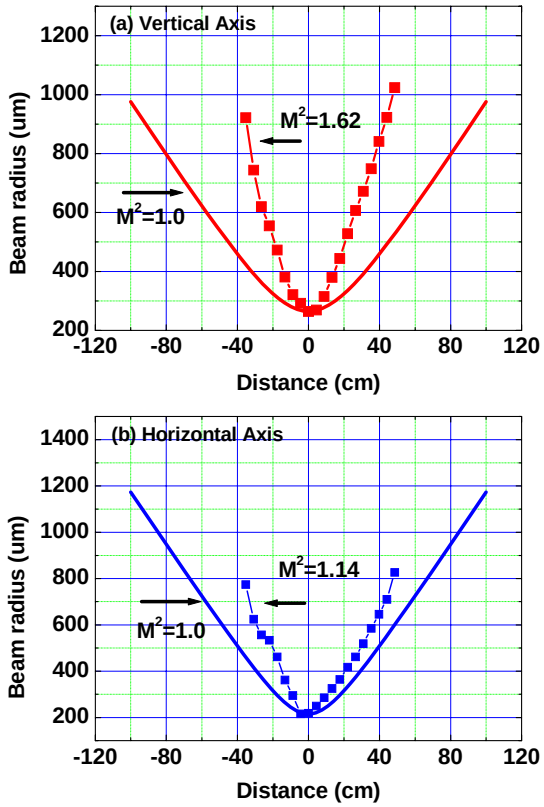

Figure 4-16: M^2 measurement for an uncompressed amplified beam of average power 5W at 5 kHz repetition rate in the (a) vertical and (b) horizontal axis

A common measure for the beam quality is known as M^2. It is defined as the ratio of divergence of the amplified beam to the divergence of an ideal Gaussian beam of equal beam waist.

$$M^2 = \frac{\omega_{0R}\theta_{measured}}{\omega_0\theta_{Gaussian}} \tag{4.21}$$

where ω_{0R} and $\theta_{measured}$ are the waist and the divergence respectively of the laser beam of unknown quality and ω_0 and $\theta_{Gaussian}$ are the waist and the divergence of a fundamental laser

mode (TEM_{00} mode). The transverse profile of the beam (ω_{0R}) was measured as a function of the propagation distance using a CCD camera. If $\omega_{0R} = \omega_0$ then

$$M^2 = \frac{\theta_{measured}}{\theta_{Gaussian}} \tag{4.22}$$

These results are shown in Figure 4-16. We observed that at lower repetition rates (5 kHz) corresponding to 5 W average power, the amplified beam M^2 values deviated from the ideal TEM_{00} mode by a factor of only 1.62 and 1.14 in the vertical and the horizontal axes respectively. The thermal astigmatism of the crystal geometry is evident in the measured M^2 value (a ratio of 1.42 in the divergence angle along the two axes). For higher repetition rates (8 kHz, average amplified power output of 9W and a boundary temperature $T_b = 108^\circ K$) this ratio increased further to 1.73 (measured M^2 values of 2.12 and 1.22 in the vertical and the horizontal axes respectively). The rise in the astigmatism of the beam shape can be attributed to the changes in the temperature related thermal constants for sapphire crystal as the boundary temperature increases at higher repetition rates.

4.10 Summary

Summarizing the contents of this chapter, we detailed the various temperature related effects in a high average power laser system and more specifically to liquid nitrogen cooled Ti: sapphire crystal in a regenerative chirped pulse amplifier. We thoroughly characterized these thermal effects using both experimental techniques (such as interferometry, M^2 analysis and measurement of focal power) as well as Finite Element Analysis. These measurements helped us in designing a suitable cavity for the regenerative amplifier that generates 5 W of 40fs, amplified output. The good agreement between the measurements and the numerical methods allowed us to extend the numerical methods to predict an optimal cavity configuration to further minimize

these thermal aberrations which are detailed along with the present status of the amplifier in the next chapter.

CHAPTER 5
CHARACTERIZATION AND OPTIMIZATION OF HIGH AVERAGE POWER CPA

Having fully investigated the fundamental aspects of designing and constructing a chirped pulse amplifier and the thermal issues inherent with high powered systems in prior chapters, this chapter concentrates on the characterization and performance of the amplifier and discusses methods to further enhance its efficiency.

5.1 Amplifier Performance

5.1.1 Average Power, Pulse Energy

The cryogenic amplifier cavity based on the extensive thermal analysis is capable of delivering 9 W of amplified power at 5 kHz repetition rate and 80 W of pump power. Figure 5-1is a plot of the measured average output power as a function of the pump laser's repetition rate.

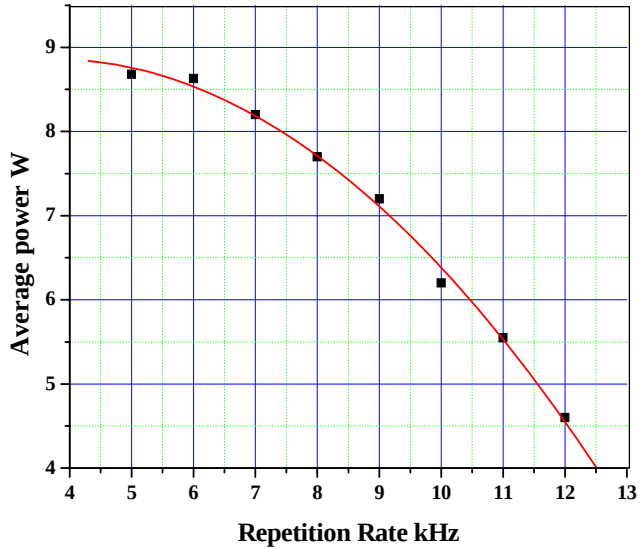

Figure 5-1: Amplified output power as a function of pump repetition rate (square points) measured before compression; the red-line is a guide to the eye.

As the repetition rate is increased the output power of the system drops. This drop coincides with the drop in the pulse energy of the pump laser (from 14.7 to 6 mJ). The boundary temperature around the crystal increases from 110 °K at 5 kHz to 123 °K at 12 kHz. Figure 5-2 indicates the amplified and the pump pulse energy with increasing repetition rate. The efficiency

of the regenerative amplifier (defined as $E_{amplified}/E_{pump}$) is approximately 14% at 5 kHz and drops to 5% at 12 kHz. The amplifier remains operational until 12 kHz repetition rate above which no lasing action is observed as the cavity ceases to be stable. By altering the cavity g-parameter, the amplifier can be made operational for repetition rates above 12 kHz. An average amplified output power of 4.5 W is generated at 12 kHz. About 60% of the amplified power was recovered from the compressor. This could easily go up by the usage of gratings with improved efficiency in the compressor setup.

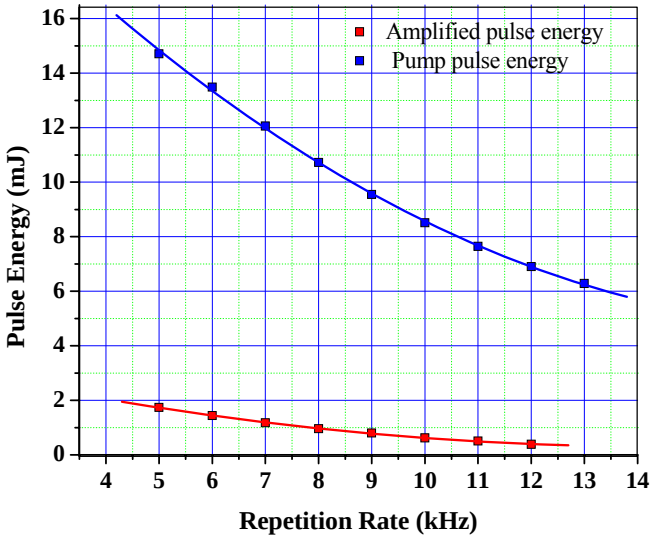

Figure 5-2: Amplified v/s pump pulse energy with increasing repetition rate. Amplified pulse energy is indicated by the red points and the pump pulse energy by the blue points. The solid lines are guides to the eye

5.1.2 Spatial Beam quality

The increasing thermal loading effects as a result of the increasing repetition rate also bring about degradation of the spatial profile of the amplified beam as in Figure 4-15. This is evident in the measured M^2 of the beam at 8 kHz repetition rate. As defined in the previous chapter, M^2 is a measurement of deviation of a laser mode from the fundamental TEM_{00} mode. A boundary temperature of 115 °K was recorded for an input pump power of 75 W at 8 kHz

repetition rate. A measured M^2 value of 1.22 and 2.12 was recorded in the vertical and the horizontal axes respectively. An average output power of 9 W (uncompressed) was obtained.

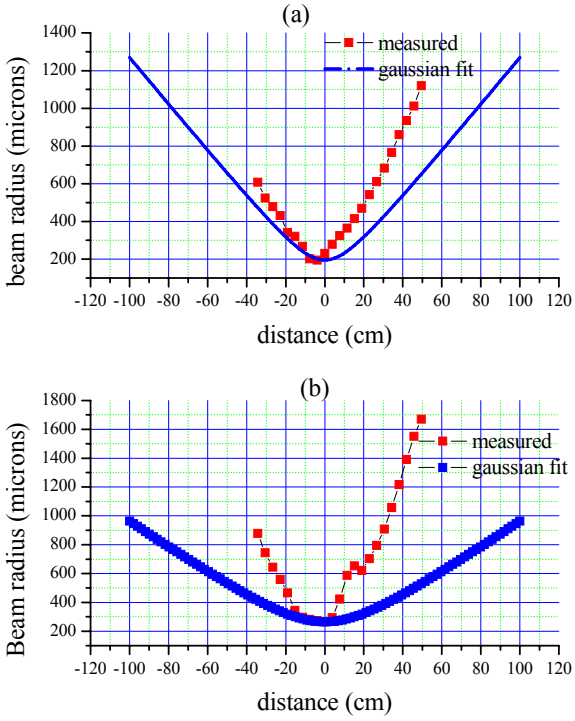

Figure 5-3: Measured M^2 for an uncompressed amplified beam of average power of 9 W at 8 kHz repetition rate in the (a) horizontal and (b) vertical axis.

The ratio of the divergence angle along the 2 axes is thus 1.73, which is a nearly 22% increase from its value at 5 kHz (1.42, Figure 4-16).

If the only source of astigmatism in the cavity is due to the Brewster crystal geometry, then increasing the repetition rate should have little or no effect to beam astigmatism. But the rise in the astigmatism of the beam shape with increasing pump power can be attributed to the changes in the temperature related thermal constants for sapphire crystal as the boundary temperature increases at higher repetition rates. Figure 5-3 is a plot of the measured M^2 along the two transverses axes plotted along with the respective divergence for a Gaussian beam of same waist.

5.1.3 Spectral Characteristics

The bandwidth of the amplified pulse is 25-30 nm (without any amplitude shaping) depending on the bandwidth of the seed pulses. The amplified spectrum is shifted to the 'blue' end of the spectrum as compared to the oscillator spectrum (Figure 5-4).

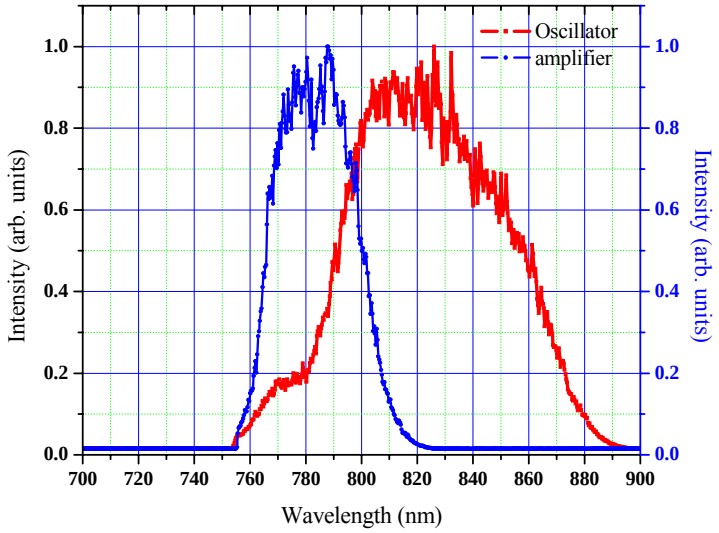

Figure 5-4: Amplified spectrum (blue-curve) for the corresponding oscillator spectrum (red curve) as measured using a fiber spectrometer.

Figure 5-5 is the emission spectra for Ti: sapphire at two different boundary temperatures: 87 °K and 300 °K. We observe that the emission spectrum is narrower at a crystal temperature of 87 °K than at room temperature. As the oscillator spectrum (Figure 5-4) is red-shifted with respect to the emission spectrum the gain of the amplifier (Figure 5-5) is pulled to the bluer edge of the spectrum due to which the amplified spectrum peaks at 780-nm as compared to 820-nm for the oscillator spectrum. The spectrum for the free-running laser for the regenerative amplifier cavity confirms the reason for this spectral shift towards the blue end (Figure 5-6). By reshaping the oscillator spectrum as in figure 3-14 using the dazzler towards the blue end not only increases the amplified output power from the regenerative amplifier but also reduces the amount of time the seed pulse needs to stay within the cavity to be able to extract gain from the crystal. This is since the gain of the sapphire crystal peaks at 775-nm (Figure 5-5), sculpting the spectrum of the

seed pulse towards the bluer edge of the spectrum leads to efficient extraction of the energy by the seed pulse from the crystal that in turn leads to a reduction in the number of roundtrips the seed pulse needs to make to be able to gain the same amount of energy as a pulse with its spectrum shifted towards the red-edge.

The amplified spectrum in Figure 5-4 generates 40-45 fs compressed pulses in a grating based compressor with an efficiency of about 60%.

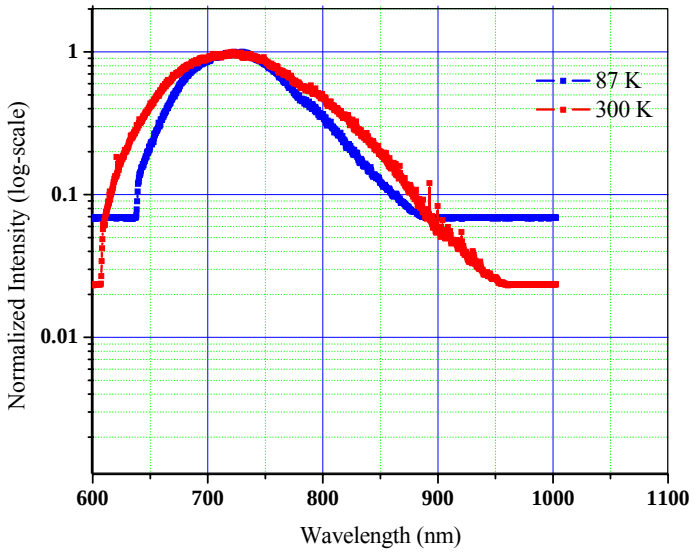

Figure 5-5: Emission spectra for Ti: sapphire.

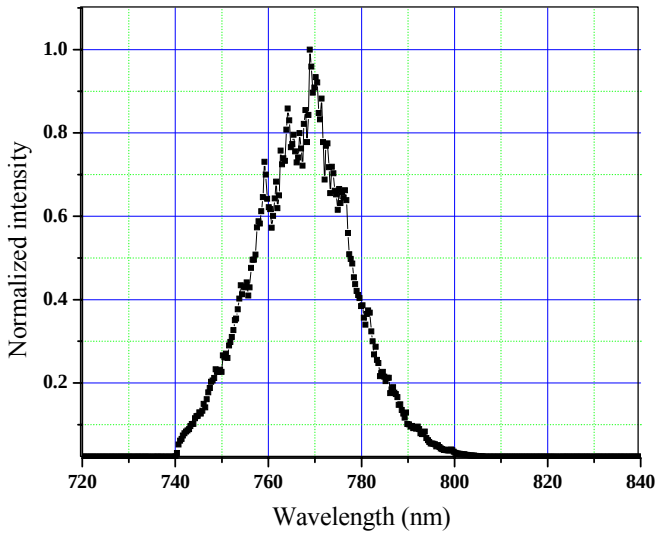

Figure 5-6: Free-running spectrum for the regenerative amplifier cavity at 5 kHz repetition rate.

5.1.4 Shot-to-shot Pulse Energy Characterization

Measuring the fluctuation of the amplified pulse energy for each amplified pulse gives one an indication of its stability. The shot-to-shot pulse fluctuations in the pulse energy were measured using a photo-diode (Thorlabs Det110) that was triggered by the repetition rate of the amplifier. A Labview based data acquisition system continuously tracked each and every pulse from the amplifier. The photo-diode was calibrated by measuring the average amplified power by using a power meter. The pulses were monitored for a time duration that was approximately 2 minutes collecting 614,987 shots at 5 kHz repetition rate (Figure 5-7).

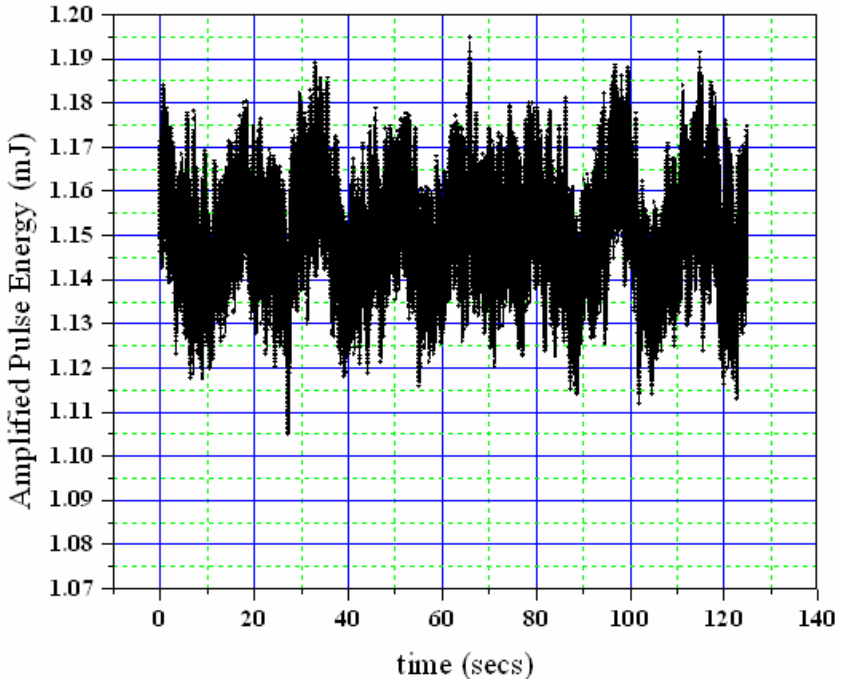

Figure 5-7: Shot-to-shot pulse energy measured for more than 600, 000 shots.

The mean pulse energy measured was 1.15 mJ. The standard deviation of the fluctuations was measured to be 0.9% of the mean pulse energy, making this CPA a very stable system with respect to pulse energy. Figure 5-8 is a histogram of the data in Figure 5-7. The excellent agreement with a Gaussian fit indicates that the fluctuations were Gaussian and hence totally random in nature.

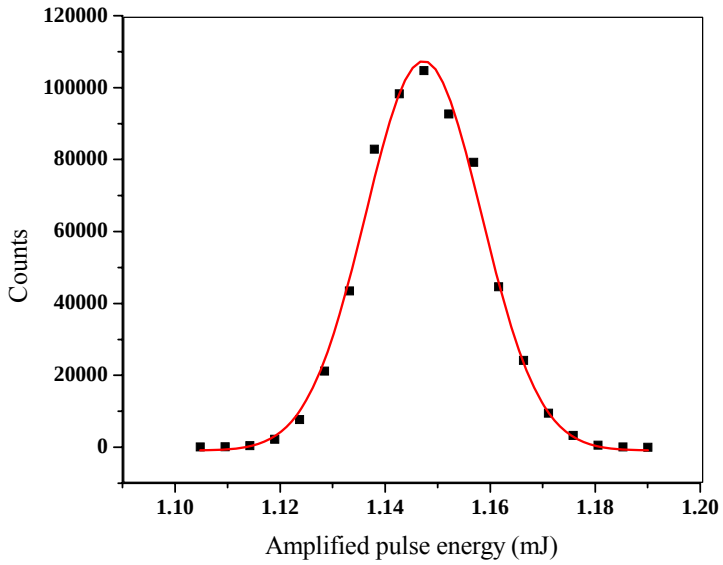

Figure 5-8: Histogram of the amplified output pulse energy. The black dots are the experimentally measured data with 20 bins and the red curve is a Gaussian fit to the data.

The following table summarizes the performance of the CPA system.

Table 5-1: Performance of the CPA system

Average compressed Power	4.68 W
Repetition rate	5 kHz
Pulse Energy	940 μJ
Bandwidth	30-35 nm
Pulse width	40-45 fs

5.2 Design Considerations for Single Stage Cryogenic CPA System

We now focus on methods to improve the efficiency of the amplifier system based on the FEA calculations described in chapter 4 and correcting for the thermally induced astigmatism in the spatial profile of the beam. Using the Finite Element Analysis described in detail in the previous chapter, one can obtain parameters of the amplifier rod geometry such as the length, radius, and boundary temperature that affect the thermal performance of the amplifier. By varying the length and the radius of the crystal while the other parameter was fixed gave useful insights into the optimum crystal geometry with least thermal loading effects.

Figure 5-9 displays the computed ΔOPD as a function of crystal length for a fixed crystal radius of 2.5-mm along both the vertical as well as the horizontal axis for two representative boundary temperatures, $T_{boundary} = 103^{\circ} K$ and $77^{\circ} K$. The incident pump power was 80 W (double pumping) with a pump waist size of 0.4-mm and a constant absorption length product, $\alpha_{abs} L = 2.2$.

Three features are evident from the above figure. First and foremost is that ΔOPD decreases by a factor of two as the length of the crystal is increased. This is particularly important for the case of $T_{boundary} = 103^{\circ} K$. Relative to the center wavelength of the amplifier (780-nm as in Figure 5-4) the aberrations are reduced from $\sim \lambda/10$ to $\lambda/18$ for the horizontal axis which displays maximum thermal loading. A ΔOPD of this magnitude only leads to changes in the focal power of the crystal as opposed to the introduction of higher order modes that are difficult to compensate. The focal power of the crystal can be easily compensated for by tuning the g-parameter of the cavity. The decrease in ΔOPD with increasing length is understandable for two reasons, the first being that for a constant absorption length product $\alpha_{abs} L = 2.2$, the increase in the length results in a reduced power density (since the power is distributed over a larger volume) and a consequent reduction in temperature throughout the crystal. Additionally, increasing the length of the crystal increases the conductive surface area thereby providing a greater path for the heat to leave the crystal. Note that the ΔOPD scales sublinearly with increasing length, thus extending the crystal beyond ~ 15 mm yield little improvement in thermal performance but a considerable increase in the group velocity dispersion (which is not desirable for ultrashort pulses).

For a boundary temperature of $77^{\circ}K$, thermal induced aberrations are diminished as compared to the 'hot' case of $103^{\circ}K$ by a factor of ~15. This comes about due to the severe temperature dependence of the thermal properties of sapphire. Thermal conductivity κ increases by a factor of 3 over this temperature range. In addition, dn/dT is also diminishing as temperature is reduced further reducing ΔOPD.

Finally there is a strong evidence of thermal astigmatism in the crystal besides the natural astigmatism due to the Brewster geometry of the crystal. For higher boundary temperature, the focal length along horizontal axis in the crystal is 1.4 times the vertical axis focal length over the entire range of crystal lengths. Although the crystal attains a slight focal power at $77^{\circ}K$, the magnitude of the thermal ΔOPD is negligible (a few nanometers).

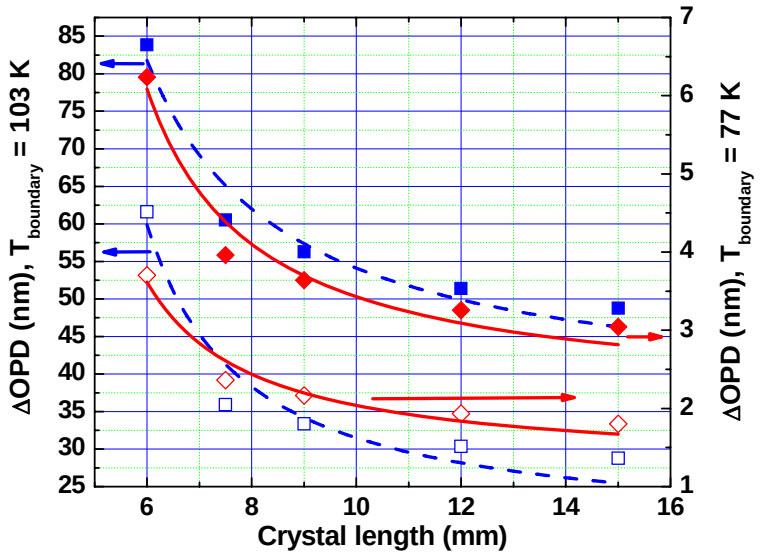

Figure 5-9: Thermally induced optical path difference versus crystal length for a fixed radius of 2.5 mm for $T_{boundary}$=103 °K (left axis) and $T_{boundary}$=77 °K (right axis). The computed OPD along the horizontal axis is shown in solid points and along the vertical axis are hollow points. The lines are guides to the eye.

Figure 5-10 displays the variance of ΔOPD with crystal radius. The calculations were again based on a total pump power of 80 W, a pump waist of 0.4 mm, a crystal length of 6mm and $\alpha_{abs}L = 2.2$. Again the thermal astigmatism for both boundary temperatures is immediately

evident with a much larger ΔOPD for $103^{\circ} K$. But the most striking features of this data are, first, that the ΔOPD increases as the radius is increased and second, the magnitude of the increase is approximately 30% less than that seen in changing the crystal length.

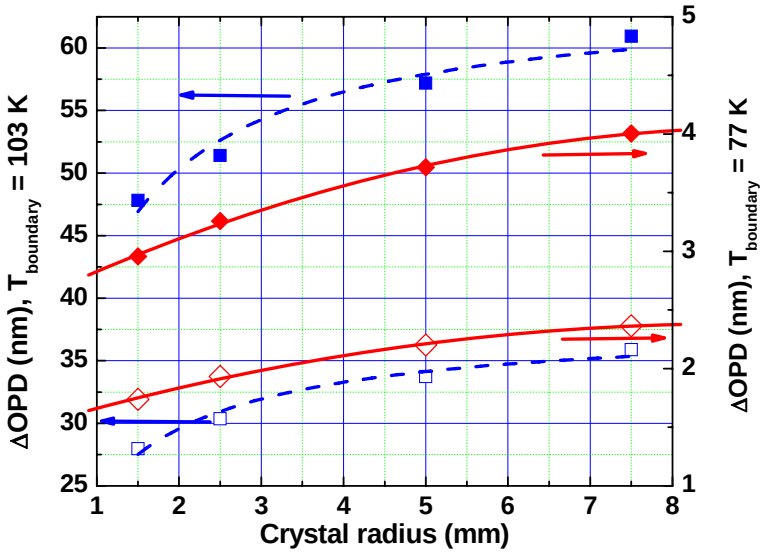

Figure 5-10: Thermally induced optical path difference versus crystal radius for a fixed length of 6 mm for $T_{boundary}$=103 °K (left axis) and $T_{boundary}$=77 °K (right axis). The computed OPD along the horizontal axis is shown in solid points and along the vertical axis are hollow points. The lines are guides to the eye.

Increasing the crystal radius also increases the surface area that should lead to better conduction of heat, reducing thermal lens effects. But by moving the boundary further from the pump area as the radius is increased, the thermal conductivity is reduced, resulting in a greater temperature rise and ΔOPD .

Thus the above simulations show that reducing the boundary temperature as much as possible result in dramatically reduced thermo-optic deformations in Brewster crystals due to the favorable thermal properties of sapphire at low temperatures. In addition, the use of longer but small radii crystal results in improved thermal performance at a given boundary temperature. While longer length and shorter radii crystals offer the best thermal performance the size of the crystal is limited by the critical heat flux (CHF) [equation(5.1)] (Kutateladze, 1948; Zuber, 1958)

of LN_2 which is defined as the maximum power that can be dissipated by the boiling liquid for a given surface area. For surface area smaller than the required minimum, vapour from the cryogenic liquid completely envelopes the surface insulating it and causing a dramatic spike in the boundary temperature.

$$CHF = (\pi/24)h_{fg}\rho_v[\frac{\sigma g(\rho_l - \rho_v)}{\rho_v^2}]^{1/4}(\frac{\rho_l + \rho_v}{\rho_l})^{1/2} \qquad (5.1)$$

where, h_{fg} is the latent heat of vaporization and is 199 J/g for LN_2, ρ_v is the vapour density and is 4.66 kg/m^3, $\rho_l = 806 kg/m^3$ is the liquid density, $\sigma = 0.00893 N/m$ is the surface tension for LN_2 and $g = 9.81 m/s^2$ is the acceleration due to gravity. Using these parameters the CHF for LN_2 is $0.163 W/mm^2$. Assuming boiling at the crystal surface, a 5mm diameter crystal would need to be at least 31.2mm long to dissipate 80 W. The crystal can also be made shorter and placed in a conductive holder with a greater surface area, but this will increase the conductive path and consequently the crystal boundary temperature.

5.3 Compensation of Modal Astigmatism

The presence of large thermal astigmatism suggests that the output mode quality is compromised, and our measurements have shown this. Measured M^2 values suggest that the ratio of the divergence angles for the vertical and the horizontal axes to be 1.42 (Figure 4-16) at 5 kHz and increasing to 1.73 at 8 kHz (Figure 5-3) repetition rate. Although the magnitude of the astigmatism is large, it does not lead to the introduction of higher order modes in the cavity. Mansell et.al. (2001) calculated the fraction of light power coupled into the higher order modes from an ideal TEM_{00} mode in thermally aberrated optical components based on modal coupling coefficients (Kogelnik, 1964). Their calculations were based on cylindrically symmetric optics that treated the two dimensional power coupling symmetrically. They found that for

$\Delta OPDs < \lambda/4$ all the distortions are to the sphericity of the beam wavefront which is a pure lensing effect and can be compensated by altering the cavity $g-$factor. By treating the thermal aberrations and the associated coupling into the higher order modes independently for both the vertical and the horizontal axes (figure 4-11) obviates the fact that the $\Delta OPDs$ can be calculated by a parabolic fit over the waist of the seed pulse on the crystal. Thus by designing an astigmatically compensated cavity, it should be possible to produce an almost pure TEM_{00} mode for a limited range of pump powers. This work is ongoing in our lab.

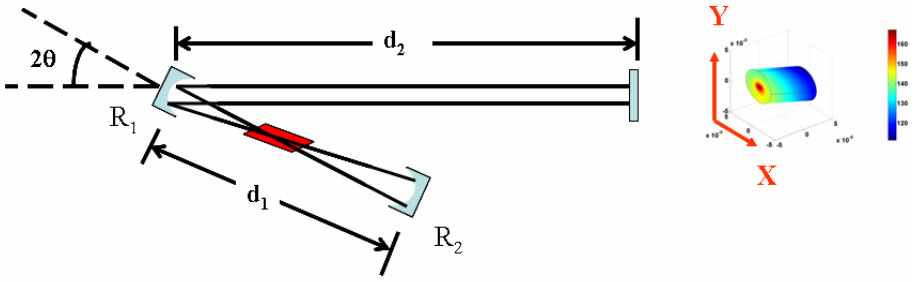

Figure 5-11: 3-mirror folded astigmatically compensated cavity.

A three mirror folded resonator cavity (Kogelnik, 1972) where the center mirror has an oblique angle of incidence (Figure 5-11) introduces astigmatism that could compensate for the thermally induced modal astigmatism. The angle of incidence is chosen to produce mode characteristics that are equal along the two transverse axes. The center mirror used at oblique incidence has two focal points, as it focuses the sagittal (xz) and the tangential (yz) at two different locations which are given as:

$$f_y = f/\cos\theta \qquad (5.2)$$
$$f_x = f \cdot \cos\theta$$

where f is the focal length of the mirror R_1 and θ is the angle of incidence. By solving the ABCD matrix independently for the two axes and carefully selecting the angle theta and the radii

of curvature R_1 and R_2, the spot sizes and hence the focal lengths f_x and f_y can be made equal and thus compensate for the thermally induced astigmatism.

5.4 Summary

Thus the amplifier generates 9 W of uncompressed amplified power at 5 KHz repetition rate and is operational for repetition rates as high as 12 kHz. The shot-to-shot energy variation of the amplifier is Gaussian in nature with the standard deviation of the fluctuations measuring 0.9% of its mean pulse energy at 5 kHz. Numerical analyses indicate that reducing the boundary temperature as low as possible results in lower thermo-optics aberrations through the crystal. Furthermore the efficiency of the amplifier could be further increased by using a sapphire crystal that is longer in length and shorter in diameter as compared to the crystal presently being used in the amplifier. Also compensating for the astigmatism in the amplified beam could lead to improved mode quality as well as an increase in output power from the amplifier.

CHAPTER 6
CONCLUSION

The need for ultrafast high brightness sources in various high laser field sciences has motivated the development of high average power, ultrashort chirped pulse amplifiers. This dissertation details the design and characterization of such a system that is capable of delivering millijoule range femtosecond pulses at repetition rates as high as 12 kHz.

In order to achieve high amplification factors $\left(\sim 10^6\right)$ in single stage systems, the crystal in the amplifier needs to be pumped with high power lasers which give rise to a host of thermal issues that prove detrimental to the system's performance. A high intensity pump laser when incident on Ti: sapphire crystal in the amplifier generates a refractive index gradient within the crystal such that the crystal gains focal power, altering the cavity parameters leading to deterioration in its performance. It is common knowledge now that cryogenic cooling of the Ti: sapphire crystal in the amplifier (Moulton, 1986; Schulz and Henion, 1991) changes its thermal properties that lead to the reduction of these thermal issues however these ideas had rarely been tried in femtosecond amplifiers and never in a single stage regenerative amplifier. Through investigations of several different cooling methods, we were able come up with an effective cooling unit housing the crystal, using liquid nitrogen that lowered the ambient temperature of the crystal to 87 °K with a mere 20 °K rise in the crystal's boundary temperature as the pump power was increased to 56 W.

While cooling the crystal reduced the various thermal effects but some remnant thermal loading effects still limited the performance of the CPA. A series of experiments were performed to fully characterize the effects of temperature on the performance of a regenerative amplifier. The experimental results were validated with a thermal model that was solved numerically for various boundary conditions using Finite Element Analysis (FEA). Measurement of the focal

powers of the crystal and the good agreement of the experimental data with the numerical model allowed us to design an effective regenerative amplifier cavity that was stable for a broad range of pump powers. The thermo-optical path deformations (ΔOPD) as a function of pump power and its effects on the mode quality of the beam was quantified using Michelson interferometry and by measuring the M^2 values for the amplified beam. In the interferometry experiment the liquid nitrogen cooled Ti: sapphire crystal was placed in one arm of a Michelson interferometer and the interference pattern as a function of pump power was recorded on a CCD camera. At the highest pump power a ΔOPD of 350-nm ± 80-nm was measured. The experimental data was compared to the computed ΔOPD values for three different boundary conditions and found that there was excellent agreement with the measured values for high pump powers for a boundary temperature of 103°K. Although the thermocouple measured a rise in the boundary temperature of 20 °K a fraction of this rise was attributed to the absorption of scattered Ti: sapphire fluorescence when the pump power was increased to 56 W. The agreement of the interferometry data with the calculated ΔOPD seemed to suggest a small 10 °K rise in the boundary temperature

We measured the mode quality of the amplified beam using a CCD camera at 5 kHz and 8 KHz repetition rates. The divergence of the amplified beam was compared to the divergence of an ideal Gaussian beam of equal waist. At 5 kHz repetition rate corresponding to 5.5 W of average power, a ratio of 1.42 in the divergence angle along the two transverse axes was measured. For an amplified power of 9 W at 8 KHz repetition rate, this ratio increased to 1.73 indicating the existence and the rise of temperature related astigmatism with increasing repetition rate besides the natural astigmatism due to the Brewster crystal geometry.

Using the FEA analysis, we explored how changing key parameters of the amplifier rod geometry (length, radius, and boundary temperature) affects the thermal performance. We found

that smaller radii and longer length crystals offer the best performance at any boundary temperature. The decreasing ΔOPD with increasing crystal length comes about from an increase in the total surface area that provides for a greater overall conductive path for the heat to leave the crystal. The increasing ΔOPD with increasing crystal radius, although less intuitive, arises from moving the boundary further from the pump area as the radius is increased, which reduces the thermal conductivity resulting in greater temperature rise and hence the increased ΔOPD. Taken together the simulations show that reducing the boundary temperature as much as possible result in dramatically reduced thermo-optical deformations in Brewster-cut crystals. This is not surprising as both κ and dn/dT have favorable thermal properties at lower temperatures. Also, the use of longer length and smaller radii crystals result in improved thermal performance at a given boundary temperature. But the size of the crystal is limited by the maximum power that can be dissipated for a given surface area known as the critical heat flux.

The large thermal astigmatism distorts the mode of the amplified beam. However the distortions are manifested as a pure lensing effect and can be easily compensated by altering the cavity g-factor.

In conclusion, we have presented in this work a state-of-the-art, high average power, single stage, state-of-the-art CPA system. The peak pulse power obtainable from this system is as high as 0.025 TW and peak intensities of the order of $10^{15} W/cm^2$ making it possible to use this system to observe a multitude of interesting nonlinear phenomena.

APPENDIX A
FREQUENCY RESOLVED OPTICAL GATING (FROG)

Ultrashort pulses have now reached the attosecond regime (Baltuska, 2003; Drescher, 2001). With such short pulses it is now possible to study dynamics of electronic motion within atoms. Intense femtosecond pulses are used to generate higher frequency harmonics that give rise to attosecond pulses. Precise information about the driving pulse is extremely important in generating pulses in the attosecond regime. Chirped pulses can cause much greater photodissociation than unchirped pulses (Kohler, 1995) and hence these experiments rely heavily on characterizing the chirp in the pulse accurately. Thus complete characterization of ultrashort pulses is of utmost importance in most ultrafast experiments.

A commonly used method for pulse measurements in laboratories is the Frequency Resolved Optical Gating (FROG) technique. It involves spectrally resolving an autocorrelation signal (Trebino, 1998). The experimental apparatus is hence similar to an autocorrelator, which is easily available in any ultrafast laboratory. SPIDER or spectral phase interferometry for direct electric-field reconstruction (Iaconis and Walmsley, 1998) is also an often-used pulse characterization technique. It is based on measuring the interference between two pulses that are almost identical expects that one pulse is slightly shifted in frequency with respect to the other by an amount Ω. This generates a spectrogram, which is essentially a spectrally resolved autocorrelation of the pulse. From the spectrogram one can obtain the spectral phase for a set of discreet frequencies separated by Ω and the amplitude is obtained from an independently measured power spectrum of the pulse.

The SHG-FROG technique overlaps a pulse with a replica of itself delayed in time. An ultrashort pulse is defined by its electric field $E(t)$ and $I(t)$ and $\phi(t)$ are its time-dependent intensity and phase respectively.

$$E(t) = \mathrm{Re}\left\{\sqrt{I(t)}\exp\left(i\omega_0 t - i\phi(t)\right)\right\} \tag{A.1}$$

A time-dependent phase gives rise to an instantaneous frequency $\omega(t)$:

$$\omega(t) = \omega_0 - \frac{d\phi}{dt} \tag{A.2}$$

The pulse in the frequency domain can be written as:

$$E(\omega) = \sqrt{I(\omega-\omega_0)}\exp\left(i\phi(\omega-\omega_0)\right) \tag{A.3}$$

Using FROG once can measure $E(t)$ [or $E(\omega)$] by measuring $I(t)$ [or $I(\omega-\omega_0)$] and $\phi(t)$ [or $\phi(\omega)$].

The autocorrelator splits the beam into two and combines them on a nonlinear crystal to generate a SHG signal $I_{SHG}(t,\tau)$:

$$I_{SHG}(t,\tau) \propto I(t)I(t-\tau) \tag{A.4}$$

As the $I_{SHG}(t,\tau)$ is a function of the delay time τ between the two pulses, it yields some measure of the pulsewidth as no second harmonic will be observed if there was no overlap between the two beams.

FROG measurements involve measurements in the time-frequency domain (spectrogram) that provide both temporal as well as spectral resolution simultaneously. A mathematical representation of the spectrogram is as follows:

$$S(\omega,\tau) = \left|\int_{-\infty}^{\infty} E(t)\,g(t-\tau)\exp(-i\omega t)\,dt\right|^2 \tag{A.5}$$

In the above equation, $g(t-\tau)$ is the gate function. The femtosecond pulse itself is used as the gate function.

If the signal measured is a SHG-based autocorrelator then the spectrogram takes the form:

$$I_{FROG}^{SHG}(\omega,\tau)=\left|\int_{-\infty}^{\infty}E(t)E(t-\tau)\exp(-i\omega t)\,dt\right|^2 \qquad \text{(A.6)}$$

Knowing the gate function allows one to accurately estimate $E(t)$ hence the above expression needs to be re-written to convert it to a two-dimensional phase-retrieval problem as the gate function is unknown. $E(t)E(t-\tau)$ for an SHG autocorrelator is $E_{sig}(t,\tau)$. Let $E_{sig}(t,\Omega)$ be the Fourier transform of $E_{sig}(t,\tau)$ with respect to Ω, such that $E_{sig}(t,\Omega=0)=E(t)$. Re-writing equation (A.6) with $E_{sig}(t,\Omega)$:

$$I_{FROG}^{SHG}(\omega,\tau)=\left|\int_{-\infty}^{\infty}E_{sig}(t,\Omega)\exp(-i\omega t-i\Omega\tau)\,dt d\Omega\right|^2 \qquad \text{(A.7)}$$

Equation (A.7) presents a classical phase retrieval problem in which the 2D spectrogram $I_{FROG}^{SHG}(\omega,\tau)$ is known (measured) and the complex quantity $E_{sig}(t,\Omega)$ is unknown. This 2D-phase retrieval problem is a common occurrence in imaging techniques and is solvable (Fienup, 1982). From the spectrogram one obtains the intensity both in the time and the frequency domain. In the 2D imaging problem, one estimates the spectral and hence the temporal phase by using an iterative algorithm such as the Gerchberg-Saxton algorithm (Gerchberg and Saxton, 1972) that performs Fourier transforms back and forth between the time and the frequency domain with known constraints in each domain. In the SHG-FROG technique the constraints on the Fourier-transform magnitudes are that they are zero outside a finite range of values of t and Ω. This additional information along with the measured $I_{FROG}^{SHG}(\omega,\tau)$ is sufficient to fully characterize the ultrashort pulse.

The experimental FROG traces are fed into an iterative Fourier transform algorithm similar to the one described above (DeLong, 1994). The algorithm continues with the iterations until the computed or the retrieved image satisfies the object image. The convergence of the algorithm is determined by the squared error defined as Z :

$$Z = \sum_{i,j=1}^{N} \left| E_{sig}^{(k)}(t_i, \tau_i) - E_{sig}^{(k+1)}(t_i, \tau_i) \right|^2 \qquad \text{(A.8)}$$

where $E_{sig}^{(k)}(t_i, \tau_i)$ is the computed electric field in the k^{th} iteration.

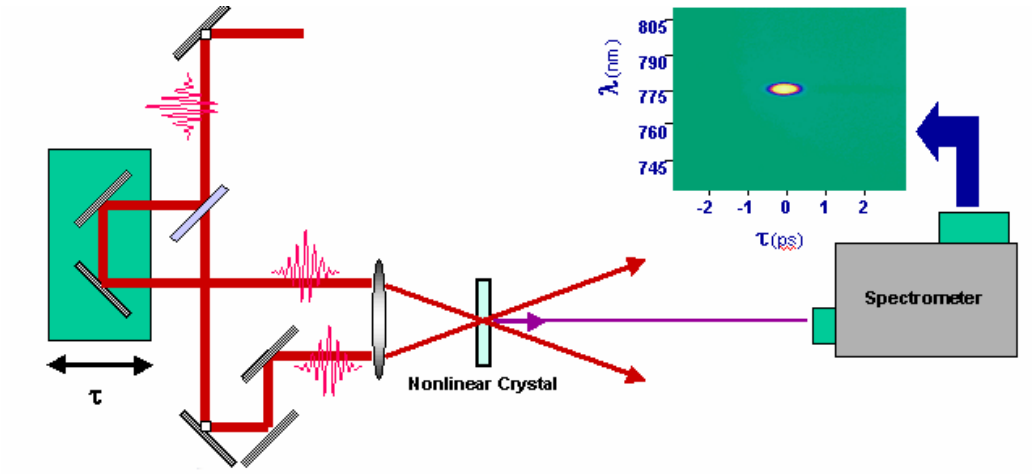

Figure A-1: Schematic of the experimental set up of the FROG apparatus in our laboratory. (Trebino, 1997)

The SHG-FROG trace is highly sensitive but it has an inherent temporal ambiguity. The pulse $E(t)$ and $E(-t)$ yield the same FROG traces as the SHG signal is symmetric with respect to delay. Thus it is possible that the actual phase is a time-reversed version of the retrieved phase. This ambiguity is easily inferred by inserting a piece of glass in the beam line that should increase the amount of positive dispersion.

The FROG apparatus in our laboratory is described in Figure A-1. The ultrashort pulse is split in two where one beam travels through a delay stage and the other through a fixed path

length. They are then focused and crossed using a cylindrical lens, on to a 100-μm KDP crystal. The SHG signal due to the mixing of the two beams is then imaged on to the slit of a spectrometer (Princeton Instruments) using a spherical lens after the crystal. The spectrometer contains its own imaging optics where the slit is further imaged on to 2D CCD chip that contains 1340 pixels along the delay axis and 100 pixels along the spectral axis. Liquid nitrogen is used to cool the CCD chip to reduce the effects of thermal noise in our measurements.

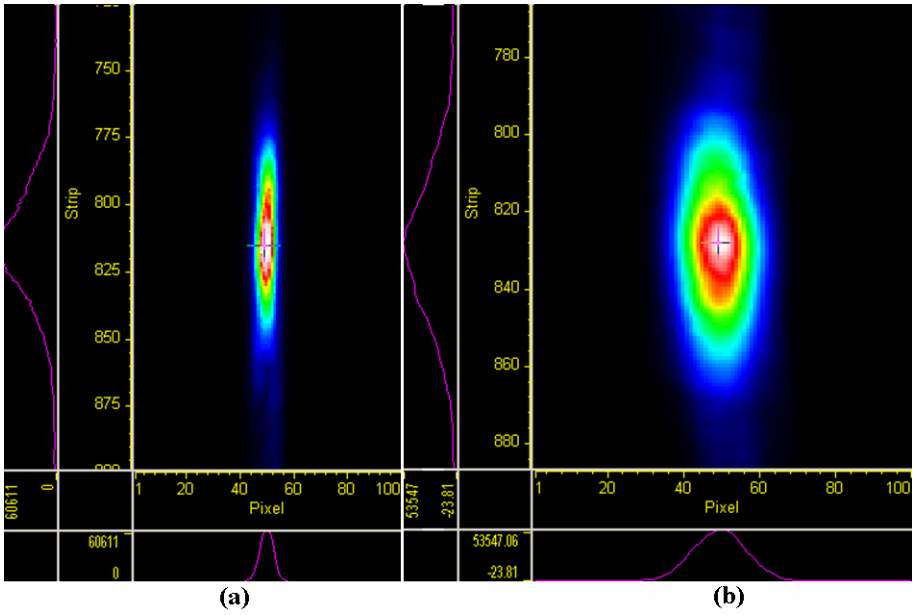

Figure A-2: Raw SHG-FROG spectrograms recorded using (a) 150 g/mm and (b) 300 g/mm grating. The horizontal axis is the wavelength axis and the vertical axis is the delay axis.

The CCD array needs to be calibrated before it can be used to obtain spectrograms. The wavelength axis was calibrated using a mercury lamp that generated spectral lines at 390-nm and 410-nm across the 100 pixels along the wavelength axis by using 300-g/mm grating in the spectrometer. By recording the pixel numbers where the spectral lines from the Hg-source were observed, one can obtain the pixel spacing in terms of nanometers and the wavelength of the first pixel. It is possible to calibrate the wavelength axis with more accuracy by using a lower resolution grating that yields many more spectral lines across the CCD chip, but the obtained

FROG traces almost always recover with huge errors than with traces that were obtained by using a higher resolution grating (Figure A-2). The temporal axis is calibrated by introducing a known amount of delay between the two beams and measuring the number of pixels the FROG image moved across the CCD chip. For a delay of 10-μm on the stepper stage, the center of the spectrogram moved by 16-17 pixels on the CCD chip. By averaging this over several 10-μm motions yielded the time (in fs) per pixel, which was usually calculated to be 1.9-2.3-fs/pixel.

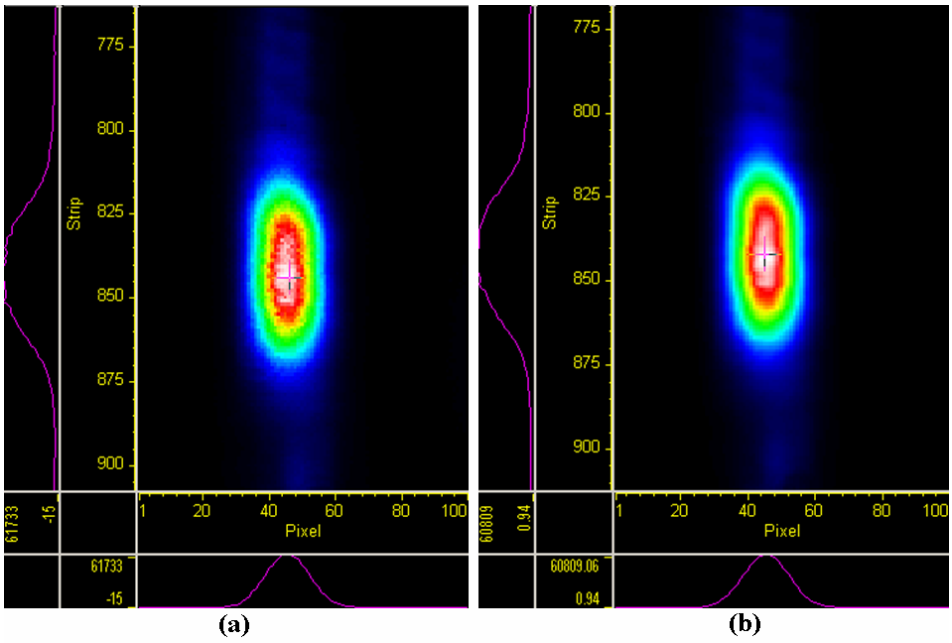

Figure A-3: Raw SHG-FROG spectrograms indicating (a) unfiltered (b) filtered traces. The horizontal axis is the wavelength axis and the vertical axis is the delay axis.

Spurious noise on the measured FROG traces that were caused due to either dust on the CCD chip or thermal noise caused due to overheating the chip, were filtered (Figure A-3) using a filtering/smoothing program available with the Princeton Instruments spectrometer driver software before introducing it through the iterative FROG software, to reduce FROG errors. The amplified pulses almost always recovered with FROG errors in the range 0.005-0.002. FROG errors higher than 0.005 were observed on the days when the amplified beam shape had

observable structures in it. The FROG traces were recovered using the software Femtosoft obtained from Swamp optics.

APPENDIX B
ACOUSTO-OPTIC PROGRAMMABLE DISPERSIVE FILTER

Pulse shaping is an important tool for generating; transform limited ultrashort pulses in a chirped pulse amplifier system. All the pulse-shaping work in this dissertation used an Acousto-Optic Programmable Dispersive filter (AOPDF) or commonly referred to as the Dazzler (manufactured by Fastlite). This section describes in detail the operation principles of an AOPDF and its several uses.

B.1 Bragg diffraction of light by Acoustic waves

An optical beam incident on a medium with a propagating acoustic wave experiences Bragg diffraction and the diffracted beam is shifted in frequency corresponding to the frequency of the acoustic wave (Yariv; Brillouin, 1922; Adler, 1967). For an incident field of frequency ω_i and an acoustic field of frequency ω_s, the frequency shift to the diffracting optical field is $\omega_{\mathrm{d}} = \omega_i + \omega_s$. Tournois (1997) was the first to demonstrated shaping of optical pulses through acousto-optic interaction in a birefringent crystal.

An acoustic wave can lead to a change in the optical properties of a birefringent medium that can cause a change in the polarization. The wave equation for an optical field through such a medium can then be written as:

$$\nabla^2 E = \mu\varepsilon \frac{\partial^2 E}{\partial t^2} + \mu \frac{\partial^2}{\partial t^2}(\Delta P) \qquad \text{(B.1)}$$

where μ and ε are the permeability constant and dielectric constant of the medium respectively and ΔP is change in the polarization of the medium due to the presence of sound wave. The change in polarization is characterized by the photo-elastic tensor p_{idkl} (a tensor of rank four)

$$\Delta P_i = -\frac{\varepsilon_i \varepsilon_d}{\varepsilon_0} p_{idkl} S_{kl} E_d \qquad (B.2)$$
$$i, j, k, l = 1, 2, 3$$

where, S_{kl} is the strain tensor and E_d is the electric field along the direction *d*.

$$S_{kl}(\vec{r}, t) = \frac{1}{2} S_{kl} \exp\left(i\left(\omega_s t - \vec{k}_s \cdot \vec{r}\right)\right) + c.c \qquad (B.3)$$

If the input optical field consists of two plane waves polarized along the i and the d direction with wave numbers k_i and k_d respectively:

$$E_i(\vec{r}, t) = \frac{1}{2} E_i(r_i) \exp\left(i\left(\omega_i t - \vec{k}_i \cdot \vec{r}\right)\right) + c.c$$
$$E_d(\vec{r}, t) = \frac{1}{2} E_d(r_d) \exp\left(i\left(\omega_d t - \vec{k}_d \cdot \vec{r}\right)\right) + c.c \qquad (B.4)$$

The RHS of equation (B.2) then takes the form:

$$\Delta P_i = -\frac{\varepsilon_i \varepsilon_d}{\varepsilon_0} p_{idkl} \frac{1}{2} S_{kl} \exp\left(i\left(\omega_s t - \vec{k}_s \cdot \vec{r}\right)\right) \frac{1}{2} E_d(r_d) \exp\left(i\left(\omega_d t - \vec{k}_d \cdot \vec{r}\right)\right) \qquad (B.5)$$

Applying the slowly varying envelope approximation to the left-hand side of equation (B.1), such that $\nabla^2 E_i \approx k_i \, dE_i / dr_i$:

$$\nabla^2 E_i(\vec{r}, t) \approx -\frac{1}{2}\left(k_i^2 E_i + 2ik_i \frac{dE_i}{dr_i}\right) e^{i(\omega_i t - k_i \cdot \vec{r})} + c.c \qquad (B.6)$$

With all the above substitutions the equality in equation (B.5) is satisfied only for the following condition:

$$\omega_i = \omega_d \pm \omega_s$$
$$k_i = k_d \pm k_s \qquad (B.7)$$

The above condition is known as the phase matching condition and is statement of conservation of total energy and momentum.

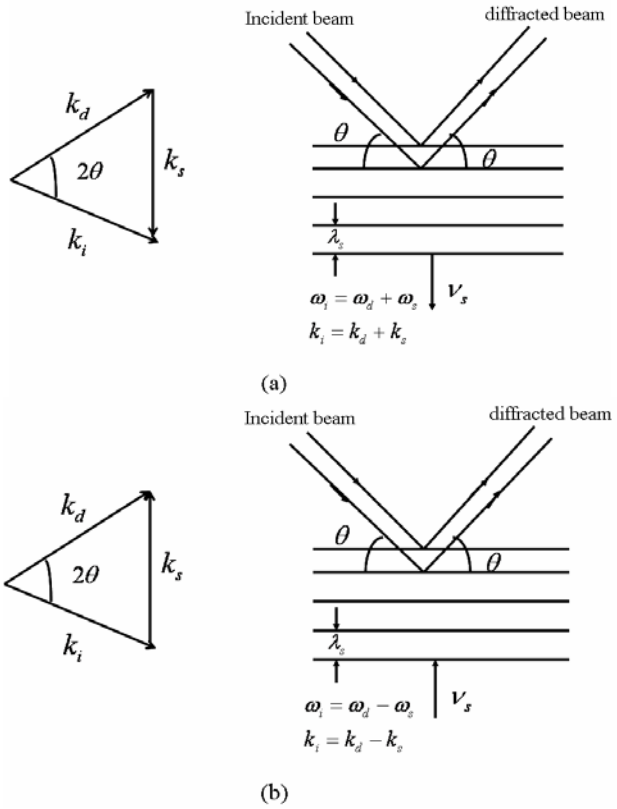

Figure B-1: Bragg vector diagram and physical configuration for (a) retreating and (b) oncoming sound waves. [Adapted from Yariv, 1989].

Figure B-1 depicts the vector diagram for two different phase matching conditions and their corresponding physical Bragg diffraction. The diffraction condition is identical to the first-order Bragg condition for the scattering of X-rays in crystals:

$$2\lambda_s sin\theta = \frac{\lambda}{n} \tag{B.8}$$

where, $k_i = k_d \approx k = 2\pi/\lambda$.

B.2 Amplitude and Phase control using an AOPDF

The AOPDF uses a birefringent uniaxial crystal that couples an ordinary (extraordinary) optical wave using an acoustic wave into the extraordinary (ordinary) optical wave. The acoustic signal is a programmable variable function of time and is used to control the group delay and the intensity of the acoustic signal controls the amplitude of the diffracted optical pulse thus

providing both phase and amplitude shaping in CPA laser systems (Tournois , 1997; Verluise, 1999; Verluise, 2000).

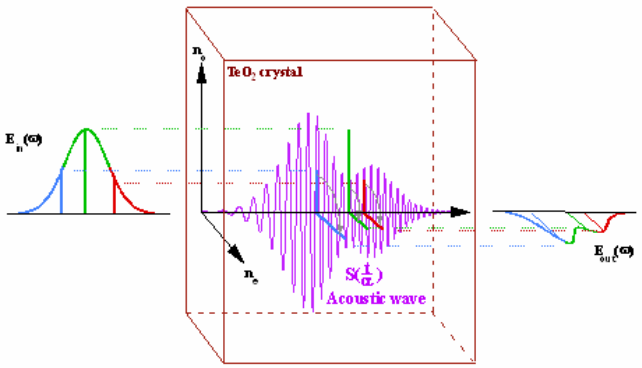

Figure B-2: Schematic of the AOPDF. [Reprinted with permission from Pittman (2002)].

As depicted in Figure B-2 an input optical pulse along the ordinary axis interacts with an acoustic wave launched along the same axis that then diffracts the optical pulse along the extraordinary axis of the crystal. For every frequency component in the input optical field to satisfy the phase-matching relation in equation (B.7), it needs to travel a minimum distance before it encounters a phase-matched spatial frequency in the acoustic grating. At this position $z(\omega)$, part of the energy is coupled (diffracted) into the extraordinary axis. Thus the pulse leaving the second axis consists of all the spectral components that have been diffracted at various positions. The amplitude of the diffracted optical field is controlled by intensity of the acoustic wave at $z(\omega)$.

Due to the difference in velocity between the ordinary and the extraordinary axes, each diffracted frequency will experience a different time delay. Then with a proper choice for a filter function in the temporal and the spectral domain one can create an arbitrary group delay distribution as a function of frequency. The optical output $E_{out}(t)$ from the AOPDF is function

of the optical input $E_{in}(t)$ and the acoustic signal $S(t)$. From the previous section we can represent the output as a convolution of the input and the acoustic signal.

$$E_{out}(t) = E_{in}(t) \otimes S\left(t/\alpha\right) \tag{B.9}$$

The scaling factor α is given as:

$$\alpha = \Delta n \frac{v}{c} \tag{B.10}$$

It is the ratio of the speed of sound to the speed of light times the difference in the refractive index between the ordinary and the extraordinary axes in the crystal. For TeO_2 $\Delta n = 0.118$, α is calculated as 0.13×10^{-6}, reflecting the much slower velocity for sound waves. The small value for α enables the control of optical signals in the hundreds of terahertz range with tens of megahertz range acoustic signals.

The acoustic wave is generated in a 2.5-cm long TeO_2 crystal, by a piezoelectric transducer. The maximum achievable group delay which is dependent on the crystal length is ~3-ps for 25-mm long TeO_2 crystal. The acoustic signal of the RF-generator that drives the crystal module is interfaced with a computer and is programmed using Labview based software (Figure B-3). The Labview based software allows one to use the dazzler in both open loop and closed loop control experiments. The RF-generator is triggered through a digital delay generator which itself is externally triggered by the mode-locked oscillator. For an amplifier repetition rate of 5 kHz, the dazzler is programmed to trigger after every 200-μs. The acoustic signal travels through the crystal area in a finite amount of time t_c which is 25-μs for a 2.5-cm crystal. Thus the maximum repetition rate at which the dazzler can be triggered is 40 kHz.

The three major application of this device in CPA laser chains is (a): amplitude shaping for the pre-compensation of the gain narrowing effect in the amplifier, (b): phase compensation to

correct for the mismatch in the stretcher and the compressor delay lines, and (c): arbitrary pulse shaping in both the spectral and the temporal domains.

.

LIST OF REFERENCES

Adler. R, “Interaction between light and sound”, *IEEE spectrum*, vol. 4, pp. 42, 1967.

Asaki. M. T, Huang. C. P, Garvey. D, Zhou. J, Kapteyn. H. C, and Murnane. M. M, “Generation of 11-fs pulses from a self-mode-locked Ti: sapphire laser”, *Opt. Lett.,* vol. 15, pp. 977, 1993.

Abramawitz M and Stegun I A, eds. Handbook of Mathematical Functions, Dover NY, 1965, p.227

Akutowicz. E. J, “On the determination of the phase of the Fourier integral I”, *Trans. Amer. Math. Soc*., vol. **83**, pp. 179, 1956.

Akutowicz. E. J, “On the determination of the phase of the Fourier integral II”, *Trans. Amer. Math. Soc.*, vol. 84, pp. 234, 1957.

Backus. S, Bartels. R, Thompson. S, Dollinger. R, Kapteyn. H. C and Murnane. M. M, “High efficiency, single-stage, 7 kHz high average power ultrafast laser system”, *Opt. Lett.,* vol. 26, pp. 465, 2001.

Backus. S, Durfree. C. G, Murnane. M. M, and Kapteyn. H. C, “High power ultrafast lasers”, *Rev. Sci. Intrum*., vol. 69, pp. 1207, 1998.

Backus. S, Peatross. J, Huang. C. P, Murnane. M. M, and Kapteyn. H. C, “Ti: sapphire amplifier producing millijoule-level, 21-fs pulses at 1 kHz”, *Opt. Lett*., vol. 20, pp. 2000, 1995.

Bagnoud. V and Salin. F, “Amplifying laser pulses to the terawatt level at a 1-kilohertz repetition rate”, *Appl. Phys. B*, vol. 70, pp. S165, 2000.

Baltuska. A, Udem. Th, Uiberacker. M, Hentschel. M, Goulielmakis. E, Gohle. Ch, Holzwarth. R, Yakovlev. V. S, Scrinzi. A, Hänsch. T. W, and Krausz. F, “Attosecond control of electronic processes by intense light fields”, *Nature*, vol. 422, pp. 611, 2003.

Bartels. R, Backus. S, Zeek. E, Misoguti. L, Vdovin. G, Christov. I. P, Murnane. M. M, and Kapteyn. H. C, “Shaped-pulse optimization of coherent emission of high harmonics of soft X-rays”, *Nature*, vol. 406, pp. 164, 2000.

Barty. C, Guo. T, LeBlanc. C, Raksi. F, Rose-Petruck. C, Squier. J, Wilson. V, Yakovlev. V, and Yamakawa. K, “Generation of 18-fs, multiterawatt pulses by regenerative pulse shaping and chirped-pulse amplification”, *Opt. Lett*., vol. 21, pp. 668, 1996.

Barty. C, Korn. G, Raksi. F, Rose-Petruck. C, Squier. J, Tian. A, Wilson. V, Yakovlev. V, and Yamakawa. K, “Regenerative pulse shaping and amplification of ultrabroadband optical pulses”, *Opt. Lett*., vol. 21, pp. 219, 1996.

Born. M and Wolf. E, “Principles of Optics”, Cambridge University Press, Cambridge, 1999.

Boyd. R, “Nonlinear Optics”, Academic Press, San Diego, CA, 2003.

Brillouin. L, “Diffusion de lumiere et des rayons X par un corps transparent homgene”, *Ann. Physique*, vol. 17, pp. 88, 1922.

Chambaret. J. P, LeBlanc. C, Cheriaux. G, Curley. P, Darpentigny. G, Rousseau. P, Hamoniaux. G, Antonetti. A, and Salin. F, “Generation of 25-TW, 32-fs pulses at 10 Hz”, *Opt. Lett.*, vol. 21, pp. 1921, 1996.

Cheriaux. G, Rousseau. P, Salin. F, Chambaret. J. P, Walker. B, and Dimauro. L. F, “Aberration-free stretcher design for ultrashort-pulse amplification”, *Opt. Lett.,* vol. 21, pp. 414, 1996.

Chung. J. H, and Weiner. A. M, “Ambiguity of ultrashort pulse shapes retrieved from the intensity autocorrelation and the power spectrum”, *IEEE Journal of Selected Topics in Quantum Electronics*, vol. **7**, pp. 656, 2001.

DeFranzo. A. C and Pazol. B. G, “Index of refraction measurements on sapphire at low temperatures and visible wavelengths”, *Appl. Opt*., vol. 32, pp. 2224, 1993.

DeLong. K. W, Fittinghoff. D. N, Trebino. R, Kohler. B, and Wilson. K, “Pulse retrieval in frequency-resolved optical gating based on the method of generalized projections”, *Opt. Lett.*, vol. 19, pp. 2152, 1994.

DeMaria. A. J , Stetser. D. A, and Heynau. H, “Self mode-locking of lasers with saturable absorbers”, *Appl. Phys. Lett*., vol. 8, pp. 174, 1966.

Descamps. D, Lynga. L, Norin. J, L’Hullier. A, Wahlstrom. C. G, Hergott. J. F, Merdji. H, Salieres. P, Bellini. M, Hansch. T. W, “Extreme ultraviolet interferometry measurements with high-order harmonics”, *Opt. Lett.,* vol. 25, pp. 135, 2000.

Drescher. M, Hentschel. M, Kienberger. R, Tempea. G, Spielmann. C, Reider. G. A, Corkum. P. B, and Krausz. F, “X-ray Pulses approaching the attosecond frontier”, *Science,* vol. 291, pp. 1923, 2001.

Downer. M. C, Fork. R. L, Islam. M, “3 MHz amplifier for femtosecond optical pulses”, *Ultrafast Phenomena IV*, 1984.

Efimov. A and Reitze. D. H, “Programmable dispersion compensation and pulse shaping in a 26-fs chirped-pulse amplifier”, *Opt. Lett.,* vol. 23, pp. 1612, 1998.

Efimov. A, Shaffer. C, and Reitze. D. H, “Programmable shaping of ultrabroad-bandwidth pulses from a Ti:sapphire laser”, *Journal of Opt. Soc. Am B.,* vol. 12, pp. 1968, 1995.

Feldman. A, Horowitz. D, Waxler. R. M, and Dodge. M. J, “Optical materials characterization”, *Final Tech. Rep.* NBS Tech. Note 993, Feb. 1, 1978-Sept. 30, 1978.

Fork. R. L, Greene. B. I, and Shank. C. V, “Generation of optical pulses shorter than 0.1 ps by colliding pulse modelocking”, *Appl. Phys. Lett*., vol. 38, pp. 671, 1981.

Fork. R. L, Martinez. O. E, and Gordon. J. P, "Negative dispersion using pairs of prisms", *Opt. Lett.,* vol. 9, pp. 150, 1984.

Gerchberg and Saxton, *Optik,* vol. **35**, pp. 237, 1972.

Gill. M. A, and Simon. J. M, "New plane grating monochromator with off-axis parabolic mirror", *Appl. Opt.,* vol. 22, pp. 152, 1983.

Graf. Th, Wyss. E, Roth. M, and Weber. H. P, "Laser resonator with balanced thermal lens", *Opt. Commun*., vol. 190, pp. 327, 2001.

Hentschel. M, Kienberger. R, Speilmann. C, Reider. G. A, Milosevic. N, Brabec. T, Corkum. P, Heinzmann. U, Drescher. M, and Krausz. F, "Attosecond Metrology", *Nature*, vol. 414, pp. 509, 2001.

Holland. M. G, "Thermal conductivity of several optical maser materials", *J. Appl. Phys*., vol. 33, pp. 2910, 1962.

Huang. C. P, Asaki. M. T, Backus. S, Murnane. M. M, Kapteyn. H. C, and Nathel. H, "17-fs pulses from a self-mode-locked-Ti:Sapphire Laser", *Opt. Lett.,* vol. 17, pp. 1289, 1992a.

Huang. C. P, Kapteyn. H. C, McIntosh. J. W, and Murnane. M. M, "Generation of transform-limited 32-fs pulses from a self-modelocked Ti: sapphire laser", *Opt. Lett.,* vol. 17, pp. 139, 1992b.

Iaconis. C and Walmsley. A, "Spectral phase interferometry for direct electric-field reconstruction of ultrashort optical pulses", *Opt. Lett.,* vol. **23**, pp. 792, 1998.

Innocenzi. M. E, Yura. H. T, Fincher. C. L, and Fields. R. A, "Thermal modeling of continuous-wave end-pumped solid state lasers", *App. Phys. Lett*., vol. 56, pp. 19, 1990.

Ippen. E. P and Shank. C. V, Subpicosecond Spectroscopy, *Picosecond Phenomena*, Shank C V, Ippen E P, Shapiro S L, Eds. New York: Springer-Verlag, 1986.

Ito. S, Nagaoka. H, Miura. T, Kobayashi. K, Endo. A, Torizuka. K, "Measurement of thermal lensing in a power amplifier of a terawatt Ti: sapphire laser", *Appl. Phys. B*, vol. 74, pp. 343, 2002.

Jung. I. D, Kartner. F. X, Matuschek. N, Sutter. D. H, Morier-Genoud. F, Zhang. G, and Keller. U, "Self starting 6.5 fs pulses from a Ti:sapphire laser", *Opt. Lett.,* vol. **22,** pp. 1009, 1997.

Kean. D. E, Kean. P. N, and Sibbett. W, "60-fs Pulse generation from a self-modelocked Ti: sapphire laser", *Opt. Lett.,* vol. 16, pp. 42, 1991.

Kimetec. J. D, Macklin. J. J, and Young. J. F, "0.5-TW, 125-fs Ti: sapphire laser", *Opt. Lett.,* vol. 16, pp. 1001, 1991.

Kitagawa. Y, Fujita. H, Kodama. R, Yoshida. H, Matsuo. S, Jitsuno. T, Kawasaki. T, Kitamura. H, Kanabe. T, Sakabe. S, Shigemori. K, Miyanaga. N, Izawa. Y, "Prepulse-free petawatt laser for a fast ignitor", *IEEE J. Quant. Electronics*, vol. 40, pp. 281, 2004.

Koechner. W, "Solid state Laser engineering", Springer-Verlag, New York ,1976.

Kogelnik. H, *Symposium on Quasi-Optics* , Polytechnic Institute of Brooklyn, Brooklyn, NY, pp. 333, 1964.

Kogelnik. H, *Bell Syst. Tech. J*., vol. 44, pp. 455, 1965

Kogelnik. H, Ippen. E. P, Dienes. A, and Shank. C. V, "Astigmatically compensated cavities for CW dye lasers", *IEEE J. Quant. Electronics,* vol. 8, pp. 373, 1972.

Kohler. B, Yakovlev. V. V, Che. J, Krause. J. L, Messina. M, Wilson. K. R, Schwentner. N, Whitnell. R. M, and Yan. Y, "Quantum control of wave packet evolution with tailored femtosecond pulses", *Phys. Rev. Lett.,* vol. 74, pp. 3360, 1995.

Knox. W. H, Downer. M. C, Fork. R. L, and Shank. C. V, "Amplified femtosecond optical pulses and continuum generation at 5 kHz repetition rate"*, Opt. Lett*., vol. 9, pp. 552, 1984.

Knox. W. H, "Femtosecond optical pulse amplification", *IEEE J. Quant. Electron*, vol. 24, pp. 388, 1988

Kutateladze. S. S, "On the transition to film boiling under natural convection", *Kotloturbostroenie*, vol. 3**,** pp. 10, 1948.

Lausten. R, and Balling. P, "Thermal lensing in pulsed laser amplifiers: an analytical model", *J. Opt. Soc. Am. B,* vol. 20, pp. 1479, 2003.

Lawrence. R, "Active wavefront correction in laser interferometric gravitational wave detectors", Ph. D. thesis, MIT, 2003.

LeBlanc. C, Grillon. G, Chambaret. J. P, Migus. A, and Notonetti. A, "Compact and efficient multipass Ti:sapphire system for femtosecond chirped-pulse amplification at the terawatt level", *Opt Lett*., vol. 18, pp. 140, 1993.

Lenzer. M, Spielmann. C, Winter. E, Krausz. F, Schidt. A. J, "Sub-20-fs, kilohertz-repetition-rate Ti:sapphire amplifier", *Opt. Lett*., vol. 20, pp. 1397, 1995.

L'Huillier. A and Balcou. P, "High-order harmonic generation in rare gases with a 1-ps 1053-nm laser", *Phys. Rev. Lett.,* vol. 70, pp. 774, 1993.

Liu. X, Du. D, and Mourou. G, "Laser ablation and micromachining with ultrashort laser pulses", *IEEE J. Quant. Electron*, vol. 33, pp. 1706, 1997.

Liu. W. T, Zhang. L. N, and Shen. Y. R, "Interfacial layer structure at alcohol/silica interfaces probed by sum-frequency vibrational spectroscopy", *Chem. Phys. Lett.,* vol. 412, pp. 206, 2005.

MacDonald. M. P, Graf. Th, Balmer. J. E, and Weber. H. P, "Reducing thermal lensing in diode-pmped laser rods", *Opt. Commun*., vol. 178, pp. 383, 2000.

Maier. M, Kaiser. W, and Giordmaine. J. A, "Intense light bursts in the stimulated Raman effect", *Phys. Rev. Lett.*, vol. 17, pp. 1275, 1966.

Maiman. T. H, "Stimulated optical radiation in ruby", *Nature,* vol. 187**,** pp. 493, 1960.

Maine. P, Strickland. D, Bado. P, Pessot. M, and Mourou. G, "Generation of ultrahigh peak power pulses by chirped pulse amplification", *IEEE Journal of Quantum Electronics,* vol. 24, pp. 398, 1988.

Mansell. J. D, Hennawi. J, Gustafson. E. K, Fejer. M. M, Byer. R. L, Clubley. D, Yoshida. S, and Reitze. D. H, "Evaluating the Effect of Transmissive Optic Thermal Lensing on Laser Beam Quality With a Shack -Hartmann Wave-Front Sensor", *Appl. Opt*., vol. 40, pp. 366, 2001.

Martinez. O. E, Gordon. J. P, and Fork. R. L, "Negative group-velocity dispersion using refraction", *J. Opt. Soc. Am. A*, vol. 1, pp. 1003, 1984.

Martinez. O. E, "3000 Times Grating Compression with Positive Group Velocity Dispersion: Application to Fiber Compensation in 1.3-1.6 μm Region", *IEEE Journal of Quantum Electronics,* vol. 23, pp. 59, 1987.

Mason. M. B, Hay. N, Hutchinson. M. H. R, "Implementation of a novel reflective doublet based stretcher design for a sub-50 fs chirped pulse amplification laser system", *CLEO*, 2000.

Miyake. C, Tidwell. S. C, Lowenthal. D. D, and Romea. R. D, "Ti: Al_2O_3 laser amplifier design study", *Proc. SPIE,* vol. 1222, Laser Radar V, R.J. Becherer, Ed. SPIE, pp. 96, 1990.

Morgner. U, Krtner. F. X, Cho. S. H, Chen. Y, Haus. H. A, Fujimoto. J. G, Ippen. E. P, Scheuer. V, Angelow. G, and Tschudi. T, "Sub-two-cycle pulsesfrom a Kerr-lens mode-locked Ti: sapphire laser", *Opt. Lett.,* vol. 24, pp. 411, 1999.

Moulton. P. F, "Spectroscopic and laser characteristics of Ti: Al_2O_3", *J. Opt. Soc. Am. B*, vol. 3, pp**.** 125, 1986.

Moulton. P. F, "Tunable solid-state lasers", *IEEE proc*., vol. 80, pp. 348, 1992.

Mueller. G, Amin. R. S, Guagliardo. D, McFeron. D, Lundock. R, Reitze. D. H and Tanner. D. B, "Method for compensation of thermally induced modal distortions in the input optical components of gravitational wave interferometers", *Class. Quantum Grav.,* vol. 19, pp. 1793, 2002.

Naumova. N. M, Nees. J. A, Sokolov. I. V, Hou. B, and Mourou. G. A, "Relativistic generation of isolated attosecond pulses in a λ^3 focal volume", *Phys. Rev. Lett.,* vol. 92, pp. 063902, 2004.

Ness. J, Naumova. N, Power. E, Yanovsky. V, Sokolov. I, Maksimchuk. A, Bahk. S, Chvykov. V, Kalinchenko. G, Hou. B, and Mourou. G, "Relativistic generation of isolated attosecond pulse: a different route to extreme intensity", *J. Mod. Optic*s, vol. 52, pp. 305, 2005.

Nye Opticals; http://www.nyeoptical.com

Offner. A, "Unit power imaging catoptic anastigmat", U.S. patents 3,748,015, 1971.

Omenetto. F. G, Taylor. A. J, Moores. M. D, and Reitze. D. H, "Adaptive control of femtosecond pulse propagation in optical fibers", *Opt. Lett.*, vol. 26, pp. 938, 2001.

Ostroverkhov. V, Waychunas. G. A, and Shen. Y. R, "New information on water interfacial structure revealed by phase-sensitive surface spectroscopy", *Phys. Rev. Lett.,* vol. 94, pp. 046102, 2005.

Paul. P. M, Toma. E. S, Breger. P, Mullot. G, Auge. F, Balcou. Ph, Muller. H. G, and Agostini. P, "Observation of a train of attosecond pulses from high harmonic generation", *Science*, vol. 292, pp. 1689, 2001.

Pennington. D. M, Brown. C. G, Cowan. T. E, Hatchett. S. P, Henry. E, Herman. S, Kartz. M, Key. M, Koch. J, MacKinnon. A. J, Perry. M. D, Phillips. T. W, Roth. M, Sangster. T. C, Singh. M, Snavely. R. A, Stoyer. M, Stuart. B. C, Wilkis. S. C, "Petawatt laser system and experiments", *IEEE J. Selected topics in Quant. Electronics,* vol. 6, pp. 676, 2000.

Perry. M. D, Pennington. D, Stuart. B. C, Britten. J. A, Brown. C. G, Herman. S, Kartz. M, Miller. J, Powell. H. T, Vergino. M, and Yanovsky. V, "Petawatt laser pulses", *Opt. Lett.,* vol. 24, pp. 160, 1999.

Pittman. M, Ferre. S, Rousseau. J. P, Notebaert. L, Chambaret. J. P, and Cheriaux. G, "Design and characterization of a near-diffraction-limited femtosecond 100-TW 10-Hz high-intensity laser system", *Appl. Phys. B*, vol. 74, pp. 529, 2002.

Quetschke. V, Gleason. J, Rakhmanov. M, Lee. J, Zhang. L, Yoshiki. F. L, Leidel. C, Mueller. G, Amin. R, Tanner. D. B, and Reitze. D. H, "Adaptive control of laser modal properties", *Opt. Lett*., vol. 31, pp. 217, 2006.

Ramanathan. V, Lee. J, Wang. X, Xu. S, Williams. L, Malphurs. W, and Reitze. D. H, "Analysis of thermal aberrations in a high average power single-stage Ti: sapphire regenerative chirped pulse amplifiers: simulation and experiment", *Rev. Sci. Instr.,* vol. 77, pp.103103, 2006.

Rettenberger. A, Leiderer. P, Probst. M, and Haight. R, "Ultrafast electron transport in layered semiconductors studied with femtosecond-laser photoemission", *Phys. Rev. B*, vol. 56, pp. 12092, 1997.

Rulliere. C Editor., “Femtosecond Laser Pulses: Principles and Experiment”, Springer, New York, 1998.

Sala. K. L, Geralidine. A, Wallace. K and Hall. G. E, “CW auto-correlation measurements of picosecond pulses”, *IEEE J. Quant. Electron*, vol. 16, pp. 990, 1980.

Salieres. P, Le Deroff. L, Auguste. T, Monot. P, D’Oliveira. P,Campo. D, Hergott. J. F, Merdji. H, and Carre. B, “Frequency-domain interferometry in the XUV with high-order harmonics”, *Phys. Rev. Lett.,* vol. 83, pp. 5483, 1999.

Salin. F, Le Blanc. C, Squier. J, and Barty. C, “Thermal eigenmode amplifiers for diffraction-limited amplification of ultrashort pulses”, *Opt. Lett.*, vol. 23, pp. 718, 1998.

Schulz. P. A, Henion. S. R, “Liquid-nitrogen-cooled Ti: Al_2O_3 laser”, *IEEE J. Quant. Electron*, vol. 27, pp. 1039, 1991.

Shank. C. V, Fork. R. L, Yen. R, Stolen. R. H, Tomlinson. W. J, “Compression of femtosecond optical pulses”, *Appl. Phys. Lett.,* vol. 40, pp. 761, 1982.

Siegman. A, “Lasers”, University Science Books, Mill Valley, CA, 1986.

Spence. D. E, Kean. P. N, and Sibbett. W, “60-fs pulse generation from a self-mode-locked Ti:sapphire laser”, *Opt. Lett.,* vol. 16, pp. 42, 1991.

Squier. J. A, Salin. F, Mourou. G. A, and Harter. D, “100-fs pulse generation and amplification in Ti:Al2O3”, *Opt. Lett*., vol. 16, pp. 324, 1991.

Squier. J. A, Korn. G, Mourou. G. A, Vaillancourt. G, and Bouvier. M, “Amplification of femtosecond pulses at 10-kHz repetition rates in Ti:Al_2O_3”, *Opt. Lett.*, vol. 18, pp. 625, 1993.

Steinmeyer. G, Sutter. D. H, Gallmann. L, Matuschek. N, and Keller. U, “Frontiers in ultrashort pulse generation: pushing the limits in linear and nonlinear optics”, *Science*, vol. 286, pp. 1507, 1999.

Stark. H, ed., “Image Recovery: Theory and Application”, Academic Press, Orlando, 1987.

Strickland. D and Mourou. G, “Compression of amplified chirped optical pulses”, *Opt. Commun.,* vol. 56, pp. 219, 1985.

Sullivan. A, Hamster. H, Kapteyn. H. C, Gordon. S, White. W, Nathel. H, Blair. R. J, and Falcone. R. W, “Multiterawatt, 100-fs laser”, *Opt. Lett*., vol. 16, pp. 1406, 1991.

Superfine. R, Huang. J. Y, and Shen. Y. R, “Nonlinear optical studies of the pure liquid/vapor interface: Vibrational spectra and polar ordering”, *Phys. Rev. Lett.,* vol. 66, pp. 1066, 1991.

Tajima. T and Dawson. J. M, “Laser electron accelerator”, *Phys. Rev. Lett.,* vol. 43, pp. 267, 1979.

Takada. H, Kakehata. M, and Torizuka. K, "High-repetition-rate 12fs pulse amplification by a Ti:sapphire regenerative amplifier system", *Opt. Lett*., vol. 31, pp. 1145, 2006.

Touloukain. Y. S, Powell. R. W, Ho. C. Y and Nicolaou. M. C, "Thermophysical Properties of matter", vol. 10**,** New York: IFI/Plenum, 1973.

Tournois. P, "Acousto-optic programmable dispersive filter for adaptive compensation of group delay time dispersion in laser systems", *Opt. Commun.,* vol. 140, pp. 245, 1997.

Treacy. E. B, "Optical pulse compression with diffraction gratings", *IEEE Journal of Quantum Electronics,* vol. 5**,** pp. 454, 1969.

Trebino. R, and Kane. D. J, "Using phase retrieval to measure the intensity and phase of ultrashort pulses: Frequency-resolved optical gating", *J. Opt. Soc. Amer. A.* vol. 10, pp. 1101, 1993.

Trebino. R, DeLong. K. W, Fittinghoff. D. N, Sweetser. J. N, Krumbugel. M. A, Richman. B. A, and Kane. D. J, "Measuring ultrashort laser pulses in the time-frequency domain using frequency-resolved optical gating", *Rev. Sci. Instru.,* vol. 68, pp. 3277, 1997.

Umstadter. D, "Review of physics and applications of relativistic plasma driven by ultra-intense lasers"*, Phys. of Plasma,* vol. 8, pp. 1774, 2001.

Verluise. F, Laude. V, Cheng. Z, Spielmann. C, and Tournois. P, "Amplitude and phase control of ultrashort pulses by use of an acousto-optic programmable dispersive filter: pulse compression and shaping", *Opt. Lett*., vol. 25, pp. 575, 2000.

Verluise. F, Laude. V, Huignard. J. P, Tournois. P, Migus. A, "Arbitrary dispersion control of ultrashort optical pulses with acoustic waves" , *J. Opt. Soc. Am B,* vol. 17, pp. 138, 1999.

Vaillancourt. G, Norris. T. B, Coe. J. S, Bado. P, and Mourou. G. A, "Operation of a 1-kHz pulse-pumped Ti: sapphire regenerative amplifier", *Opt. Lett.,* vol. 15, pp. 317, 1990.

Von der Linde. D, Sokolowski-Tinten. K, and Bialkowski. J, "Laser-solid interaction in the femtosecond time regime", *Appl. Surf. Sci*. vol. 109/110, pp. 1, 1997.

Wynne. K, Reid. G. D, Hochstrasser. R. M, "Regenerative amplification of 30-fs pulses in Ti:sapphire at 5 kHz", *Opt. Lett*., vol. 19, pp. 895, 1994.

Wyss. E, Roth. M, Graf. Th, and Weber. H. P, "Thermooptical compensation methods for high power lasers", *IEEE J. Quantum Elec*., vol. 38, pp. 1620, 2002.

Yariv. A, "Quantum Electronics", 3rd edn. Wiley, New York, 1989.

Zewail. A. H, "Femtochemistry: Recent progress in studies of dynamics and control reactions and their transition states", *J. Phys. Chem.,* vol. 100, pp. 12701, 1996.

Zhavoronkov. N, and Korn. G, "Regenerative amplification of femtosecond laser pulses in Tisapphire at multikilohertz repetition rates", *Opt. Lett*., vol. 29, pp. 198, 2004.

Zhou. J. P, Huang. C. P, Murnane. M. M, and Kapteyn. H. C, "Generation of 21-fs millijoule-energy pulses by use of Ti: sapphire", *Opt. Lett*., vol. 19, pp. 126, 1994.

Zhou. J. P, Huang. C. P, Murnane. M. M, and Kapteyn. H. C, "Amplification of 26-fs, 2-TW pulses near the gain-narrowing limit in Ti:sapphire", *Opt. Lett*., vol. 20, pp. 64, 1995

Zhou. X, Kanai. T, Yoshitomi. D, Sekikawa. T, Watanabe. S, "Generation of high average power, 7.5-fs blue pulses at 5 kHz by adaptive phase control", *Appl. Phys. B*, vol. 81, pp. 13, 2005

Zuber, N, "On the Stability of Boiling Heat Transfer", *Trans.* ASME, vol**.** 80**,** pp. 711, 1958.

BIOGRAPHICAL SKETCH

Vidya Ramanathan was born in Chennai (then Madras) a southern city in India on October 31st 1976. But soon thereafter her parents moved to Mumbai (then Bombay) along the west coast of the country where she was brought up with two younger twin siblings. After graduating from high school in May '94, she entered the Physics department at the Ramnarain Ruia College in Bombay to obtain a B.Sc degree in physics in the fall of '97. She then received her master's degree in physics at the University of Bombay during the summer of '99.

She began her graduate studies at the Indian Institute of Technology at Bombay from August '99. Disillusioned with her progress at grad school, she decided to head west and landed at the University of Florida, in fall 2000. Joining Dr. David Reitze's optics group at UF, she nurtured her interests in the field of femtosecond lasers and has since been involved in the development of a high average power chirped pulse amplifier system.